Optical and mechanical characterization of freestanding multilayer graphene membranes

Huijs, Jochem M.M.

Award date:
2017

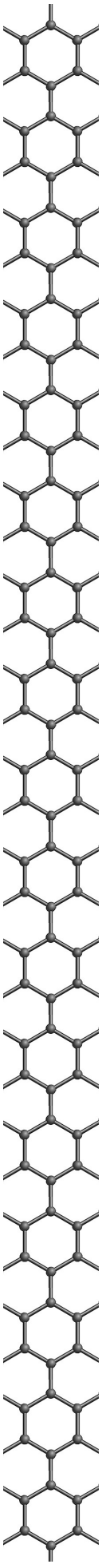

Optical and mechanical characterization of freestanding multilayer graphene membranes

Master Thesis

J.M.M. Huijs, BSc

October 5, 2017

Optical and mechanical characterization of freestanding multilayer graphene membranes

J.M.M. (Jochem) Huijs, BSc

Master of Science Thesis
October 5, 2017
PMP 17-12

Eindhoven University of Technology
Department of Applied Physics
Plasma & Materials Processing

Philips Innovation Services
MEMS & Micro Devices

Supervisors:
Dr. A.J.M. (Jos) Giesbers (PInS)
Dr.ir. J.H. (Johan) Klootwijk (Philips Research)
Dr. A.A. (Ageeth) Bol (TUe)

Graduation committee:
Dr. A.A. (Ageeth) Bol
Dr.ir. C.F.J. (Kees) Flipse
Dr.ir. E.J.D. (Edgar) Vredenbregt
Dr.ir. J. (Job) Beckers
Advisors:
Dr. A.J.M. (Jos) Giesbers (PInS)
Dr.ir. J.H. (Johan) Klootwijk (Philips Research)

Abstract

Graphene exhibits an extremely high strength-to-weight ratio, which can amongst others be used to create large scale ultrathin optical windows. For further development and upscaling in size it is essential to acquire information on its thickness and stiffness, being two focus areas of this thesis. Furthermore, since graphene shows large potential for use in electromechanical resonators due to its large stiffness and light weight, potential operating characteristics of graphene-CMUT devices are assessed.

Combining excitonic resonance, the so-called Fano resonance effect, with the linear scaling conductivity in multilayer graphene, a full range UV-vis (∼250-1100 nm) transmission model is proposed. This model is used to determine the thickness of different multilayer graphene membranes. Additionally, this model provides a method to calculate the reflection of multilayer graphene membranes based on the fitted transmission curves, where reflection is generally neglected in optical studies on graphene.

In order to investigate the stiffness of the multilayer membranes, bulge test have been performed on two different membrane configurations, being able to individually extract the Young's modulus E and Poisson ratio ν. Graphene membranes with a thickness of $t = 11.5$ nm show a relatively constant intrinsic Young's modulus of $E \approx 80$ GPa, which increases to $E \approx 150$ GPa for membranes with a thickness of $t = 2.76$ nm. These values are lower than the theoretical value of $E = 1$ TPa for single-layer graphene, indicating the mechanical response might be more towards graphite-like values of $E = 15 - 30$ GPa. The Poisson ratio ν on the other hand shows a significant increase, clearly different from the generally used constant value of $\nu = 0.16$ throughout literature. The Poisson ratio increases from a near-zero value at low stress, to well above the theoretical isotropic limit of $\nu = 0.5$. This suggests the Poisson ratio ν is the main effect contributing to the non-linear effective response E_b and E_p for square and rectangular membranes, respectively. Quantitative analysis of the non-linear effect suggests small-scale crumpling of the graphene membranes can be the main cause for this effect.

Multilayer graphene membranes have been electromechanically actuated, showing proof-of-principle operation as present in CMUT devices. Through modeling suggestions are made for optimal design parameters. While this states potential ranges of operation in for example medical imaging, more information is needed on certain output parameters. Main parameter to be investigated is the output sound wave pressure, before assessing the benefits of graphene membranes over current membrane materials.

Contents

1 Introduction **1**
- 1.1 Graphene: the golden age in physics . . . 1
- 1.2 Graphene membranes . . . 2
- 1.3 Research questions . . . 3
- 1.4 Thesis outline . . . 4

2 Sample design, processing and experimental setups **5**
- 2.1 Introduction . . . 5
- 2.2 Graphene membrane preparation . . . 5
  - 2.2.1 Pre-deposition processing and CVD graphene deposition . . . 6
  - 2.2.2 Postgraphene deposition processing . . . 6
- 2.3 Raman characterization . . . 8
- 2.4 UV-vis experimental setup . . . 9
- 2.5 Bulge test experimental setup . . . 10

3 Thickness determination **13**
- 3.1 Introduction . . . 13
- 3.2 Conventional transmission spectroscopy on graphene . . . 14
- 3.3 Single-layer graphene universal conductivity σ_0 and light transmission . . . 15
- 3.4 Energy depence of the conductivity of single-layer graphene . . . 16
  - 3.4.1 Empirical single-layer graphene conductivity model . . . 16
  - 3.4.2 Exciton effect: Fano resonance and its effect on optical conductivity . . . 17
- 3.5 Multilayer graphene UV-vis transmission . . . 19
- 3.6 UV-vis results . . . 21
  - 3.6.1 Conductivity fitting and growth uniformity . . . 21
- 3.7 Conclusion . . . 24

4 Membrane characterization: bulge testing **25**
- 4.1 Introduction . . . 25
- 4.2 Young's modulus E and Poisson ratio ν . . . 26
- 4.3 Bulge testing . . . 28
  - 4.3.1 Membrane profile analysis . . . 29
  - 4.3.2 Geometrical configurations . . . 31
- 4.4 Bulge test results . . . 32
  - 4.4.1 Young's modulus & Poisson ratio determination . . . 32
  - 4.4.2 Membrane crumpling and non-linear bulging . . . 36
  - 4.4.3 Layer dependent membrane stiffening . . . 37
- 4.5 Conclusion . . . 40

5 Graphene incorporation in CMUT **43**
5.1 Introduction . . . 43
5.2 CMUT design and processing . . . 44
5.2.1 Conventional CMUT designs . . . 45
5.2.2 Graphene incorporation in resonators and CMUTs . . . 45
5.3 Membrane actuation . . . 46
5.3.1 Electrostatic attraction . . . 47
5.3.2 Membrane vibration . . . 48
5.4 CMUT characteristics modeling . . . 48
5.4.1 Capacitance . . . 49
5.4.2 Collapse voltage . . . 51
5.4.3 Frequency modeling . . . 54
5.5 Conclusion . . . 55

6 Conclusions and outlook **57**
6.1 Thesis conclusions . . . 57
6.2 Outlook and recommendations for future research . . . 58

Acknowledgements **61**

Bibliography **63**

Appendix:

A Continuous versus discrete convolution **73**

B Square membrane fitting **75**
B.1 Spherical fit . . . 75
B.2 Individual cross-sectional fits . . . 77

C Stress-strain curve: hysteresis effects **79**

D Parameter error analysis **81**
D.1 Individual strain moduli and Young's modulus . . . 81
D.2 Poisson ratio . . . 82

E Individual bulge test fit parameters **83**
E.1 Biaxial E_b and planar E_p modulus . . . 83
E.1.1 Type 1 graphene: thickness $t = 11.5$ nm . . . 83
E.1.2 Type 2 graphene: thickness $t = 2.76$ nm . . . 84
E.2 Non-linear strain-stress analysis parameters . . . 85

F Bulge test sample deviations **87**

G MATLAB scripts **89**
G.1 UV-vis transmission model . . . 89
G.2 Bulge test: membrane profile fits . . . 95
G.2.1 Cylindrical membrane . . . 95
G.2.2 Square membrane . . . 96

Chapter 1

Introduction

In this introduction a general overview on graphene and graphene membranes in specific is given. This thesis focuses on graphene membranes, since they prove to be excellent candidates for use as optical windows and electromechanical resonators. This introduction shortly touches upon the different aspects of the graphene membranes, such as the importance of its thickness and mechanical stiffness. The corresponding research questions are formulated and the added value of this thesis to the current literature knowledge on (multilayer) graphene membranes is indicated. At the end of this introduction a detailed outline of this thesis is given, describing the different chapters and their research focus.

1.1 Graphene: the golden age in physics

It can be safely assumed that graphene is one of the most heavily researched materials nowadays. Despite its relatively recent experimental discovery, the number of publications related to graphene has increased to 14,000 within a decade, with on average 40 papers being published on graphene per day in 2014 [1]. Applications incorporating graphene are researched across numerous fields, ranging from biological engineering [2] and optical electronics [3], to filtration systems [4, 5] and photovoltaic devices [6].

Graphene consists of carbon atoms arranged in a 2-dimensional honeycomb lattice. Figure 1.1 shows a schematic overview of this 2D structure, which acts as building block for other well-known shapes such as zero dimensional buckyballs, one dimensional nanotubes and three dimensional graphite [7]. Before its experimental discovery, 2D graphite, now known as graphene, already was a theoretical topic of interest. It was thought however, that graphene was never able to exist as a free material due to being thermodynamically unstable [8]. Researchers posed random fluctuations would ripple the 2D structures to such an extent, it is more suitable to consider them 3D structures in stead of 2D materials. In 2004 though, Geim and Novoselov experimentally extracted the first graphene samples at the University of Manchester [9]. Their method of extracting a single layer of graphene by means of mechanical exfoliation is often referred to as the 'Scotch tape'-method. This method involves peeling of a layer of carbon atoms from a larger chunk of highly oriented pyrolytic graphite (HOPG) using a piece of Scotch tape. Nowadays, the Scotch tape-method is still used to extract micrometer size graphene flakes generally used in research. Improvements have been made to generate techniques more suitable for incorporation in industrial applications, which are based on wafer-scale processing. Techniques such as chemical vapour deposition (CVD) or synthesis on silicon carbide (SiC) wafers have been developed, resulting in a more large scale production of graphene more suitable for semiconductor applications [10].

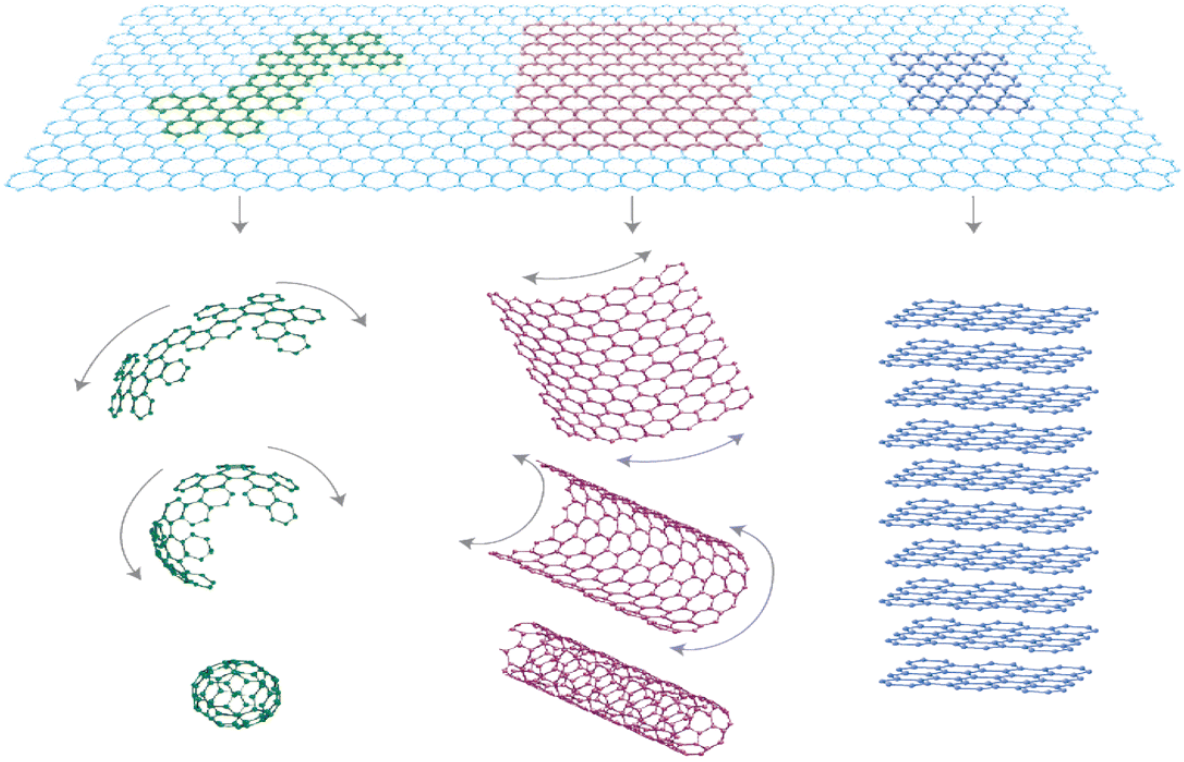

Figure 1.1: *Graphic representation of a sheet of graphene. Choosing an appropriate area within the lattice, graphene can be restructured into 0D buckyballs, 1D nanotubes or 3D graphite.*[1]

Despite graphite commonly being known as an insulator, graphene is shown to have an extremely high electron mobility, thus exhibiting aspects more resembling conducting materials [11]. The extraordinary properties of graphene have rapidly accelerated research across various fields. An example is the possibility to study the Quantum Hall Effect at room temperature [12, 13]. Before the experimental discovery of graphene, this research field was only accessible to low-temperature, high energy physicists.

One of the main focus areas of this thesis is the mechanical behavior of graphene. This topic is motivated by the awarding of the Nobel in Physics to Geim and Novoselov for their experimental discovery of graphene. In their Nobel prize lecture the potential of graphene is nicely illustrated: 'It [graphene] is so strong that a 1 m^2 hammock, no heavier than a catÂŠs whisker, could bear the weight of an average sized cat without breaking' [14]. This extreme strength-to-weight-ratio can be implemented in various applications which require strong mechanical properties but very little material mass itself. Examples of these applications are ultra-thin optical windows [15] or extremely sensitive pressure sensors [16]. These forms of (multilayer) graphene membranes are currently being researched at Philips Innovation Services, of which this work is a part.

1.2 Graphene membranes

Large scale graphene membranes show large potential for use as optical windows in X-ray spectroscopy [17, 18], electron microscopy [19] and cryoTEM analysis [20]. These applications require a high photon-transmission, while simultaneously spanning large surface areas.

[1] Image source: Geim *et al.* (2007) [7]

Although it already has been shown multilayer graphene membranes can be spanned over mm^2-size areas [22, 21, 23], see Figure 1.2, the exact thickness of the graphene membranes is still a point of discussion. Since this thickness determines the amount of light transmitted, it is crucial to investigate of how many graphene layers the multilayer membranes consist. Here transmission spectroscopy has shown to be a prime candidate for thickness determination of multilayer graphene membranes [22, 24].

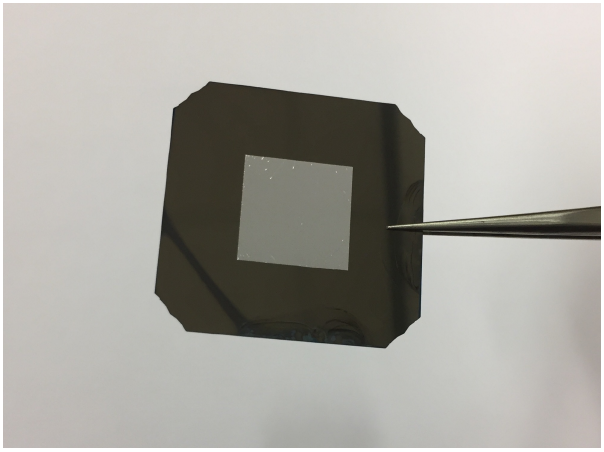

Figure 1.2: *Typical 11x11 mm^2 multilayer graphene membrane as studied in this thesis. The nanometer thin semi-transparent graphene membrane can be identified by eye.*

In order to acquire even larger surface areas of graphene membranes, its mechanical response has to be optimized to meet these requirements. While the mechanical properties of small scale $\sim \mu m^2$ single-layer graphene membranes are a field of interest in current research [25, 26], the mechanical properties of large scale $\sim mm^2$ multilayer graphene membranes have been less frequently investigated. Therefore it is also necessary to acquire insight into the mechanical characteristics such as the stiffness of the multilayer graphene membranes. Being commonly used in thin film characterization, bulge testing has proven to be an excellent technique for determining the mechanical characteristics of thin membranes [27].

1.3 Research questions

As described in the previous section, applications such as optical windows require detailed characterization of the thickness and stiffness of the material. Additionally, ultrasound transducers are currently researched at Philips, in which graphene membranes could be potentially incorporated, replacing standard micromachined materials [28, 29]. These properties form the basis of this thesis, formulated in the three main research questions:

1) "How can the thickness of freestanding multilayer graphene membranes be accurately determined through UV-vis spectroscopy?"

UV-vis spectroscopy has proven to be an excellent non-invasive technique for multilayer graphene analysis. Current research on full-range UV-vis spectroscopy on single-layer graphene has delivered detailed models, whereas for multilayer graphene mostly single-wavelength UV-vis spectroscopy is applied. In this thesis a full-range multilayer graphene UV-vis model is proposed and fitted with transmission measurements on membranes with different thicknesses.

2) "What is the mechanical response of freestanding multilayer graphene membranes?"

Since literature knowledge on the mechanical response of multilayer graphene membranes is very sparse, it is chosen to investigate the mechanical response of the membranes in more detail, thus leading to this second research question. This thesis describes a method to independently determine the Young's modulus E and Poisson ratio ν of the multilayer graphene membranes, applying the method of bulge testing on large scale graphene membranes.

3) "Can freestanding multilayer graphene membranes replace current membrane structures in ultrasound transducers?"

Combining the mechanical and electronic properties of multilayer graphene membranes has led to formulation of the third research question of this thesis. The potential use of graphene in ultrasound transducers is investigated using a proof-of-principle experimental setup. Combined with modeling of potential output parameters, this proves insight into the possible characteristics of such graphene-transducer devices.

1.4 Thesis outline

This thesis is structured according to the three research questions mentioned above. Since these questions each require a different analysis approach of the graphene membranes, they are centralized in individual chapters.

- **Chapter 2: Sample design, processing and experimental setups**
  This chapter describes the preparation of the multilayer graphene membranes studied in this thesis. The multilayer graphene is characterized through Raman spectroscopy, and the two main experimental setup used in this thesis are described: UV-spectroscopy and bulge testing.
- **Chapter 3: Thickness determination**
  Here the first research question is addressed. First, a literature overview on transmission spectroscopy on multilayer graphene is given. The transmission through single-layer graphene is related to its optical conductivity, describing the relevant excitonic effects in the UV-vis regime. Extending to multilayer graphene, a full-range UV-vis transmission model is proposed, eventually used to analyze different graphene thicknesses.
- **Chapter 4: Membrane characterization: bulge testing**
  This chapter outlines the second research question, characterizing the mechanical response of the multilayer graphene membranes. First, a general introduction on the mechanical characteristics and the principle of bulge testing is given. Different membrane configurations and thicknesses are tested, comparing the mechanical response to recent literature on the bulging of single-layer graphene.
- **Chapter 5: Graphene incorporation in CMUT**
  The third research question is investigated in this chapter, reporting the potential for the use of graphene membranes in ultrasound transducers. The working principle of conventional ultrasound transducers is explained, additionally discussing recent attempts to incorporate graphene in electromechanical resonators. Proof-of-principle actuation of the graphene membranes created in this thesis is shown. Lastly, potential characteristics of graphene-transducer are modeled, suggesting optimal parameters for desired applications.
- **Chapter 6: Conclusions and outlook**
  At the end of this thesis, the findings in this work concerning the three research topics are outlined. Based on the different results acquired, recommendations for future research are given.

Chapter 2

Sample design, processing and experimental setups

This chapter provides a description of the processing of the multilayer graphene membranes studied throughout this thesis. The processing steps for fabrication of the graphene membranes are discussed, after which a characterization of the graphene through Raman spectroscopy is presented. Lastly, the two experimental setups, UV-vis spectroscopy and bulge testing are discussed, centralizing the experimental discussion of this work in this chapter.

2.1 Introduction

The process of manufacturing graphene membranes has always followed a similar approach over the past decade. It essentially involves two separate substrates used in fabrication: one on which the graphene is grown, and a second permeated substrate onto which the graphene is transfered, forming the actual membranes [30]. Although this process does deliver freestanding graphene membranes, it often results in transferal residue on the membranes. Besides sample contamination, transferring large areas of graphene entails manual processing and low reproducibility. Since industrial process flows are based on full wafer scale processing, especially this last restriction is unfavorable for semiconductor processing and the potential for incorporation of graphene.

This chapter describes the manufacturing process for the graphene membranes used in this thesis. Production of the graphene membranes is performed using the cleanroom facilities at Philips Innovation Services (PInS) at the High Tech Campus in Eindhoven, The Netherlands. In contrast to the graphene transfer process, the fabrication process in this thesis selectively removes the substrate from underneath the graphene. Using this method the membranes are directly created on the substrate wafer and the transferring process is bypassed. A similar process has already been presented producing graphene membranes in the order of $100 - 3000$ μm^2 [31]. In this thesis we extend this method to produce freestanding multilayer graphene membranes in the order of $\sim mm^2$ to $\sim cm^2$.

2.2 Graphene membrane preparation

In this thesis two type of graphene membranes with different thicknesses are created, throughout this thesis referred to as type 1 and type 2. Although the graphene growth process is outside of the scope of this work, the process of graphene deposition is shortly described below. After graphene deposition the wafers are further processed at Philips, obtaining the individual graphene membrane samples.

2.2.1 Pre-deposition processing and CVD graphene deposition[1]

The multilayer graphene is grown by chemical vapour deposition (CVD) on a metal catalyst. This metal catalyst is sputtered on the front side of a silicon (100) wafer. The multilayer graphene growth process is based on the procedure presented by Grachova *et al.* (2014) describing a wafer-scale CVD graphene growth process [32]. A temperature profile of the growth process is shown in Figure 2.1. The wafer is gradually heated to a temperature of 1010 °C in an environment of Ar and H_2. When the desired temperature is reached, an annealing step is initiated to remove any native oxide from the metal catalyst's surface. After annealing, methane gas (CH_4) is introduced to start the graphene growth. By selecting the duration of the methane gas flow, the amount of graphene deposition and therefore the multilayer thickness can be controlled.

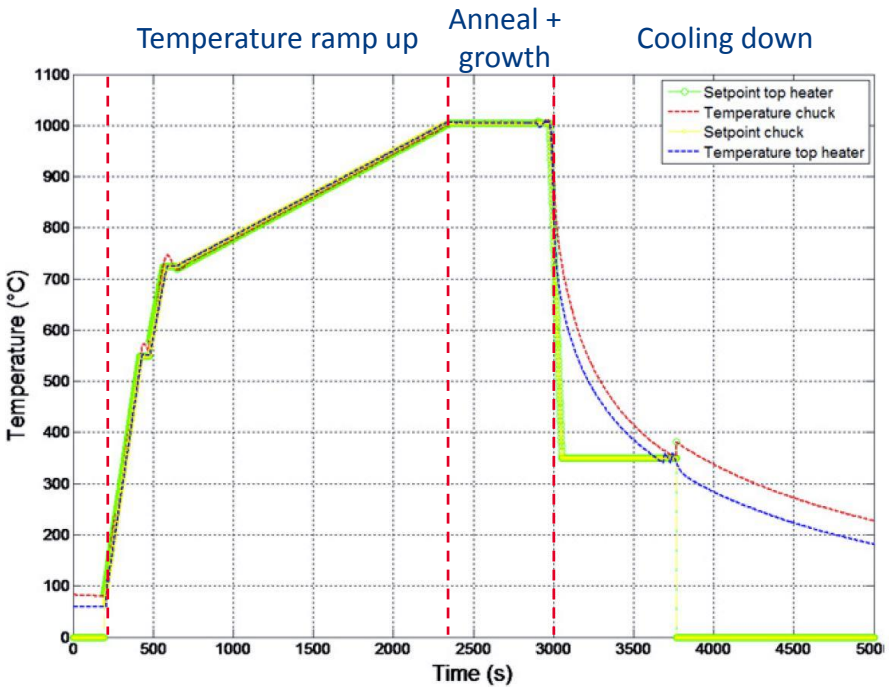

Figure 2.1: *Typical temperature profile of the multilayer graphene deposition process. The three main processes are indicated: temperature ramp up, anneal and graphene growth, and cooling down.*[2]

The growth process of multilayer graphene depends on multiple factors such as C-solubility of the metal catalyst [33] and the cooling-rate after growth [34], factors which are outside the scope of this thesis and therefore will not be discussed here. For more details on the growth process of graphene, see the papers of Munoz *et al.* (2013) [33] and Grachova *et al.* (2014) [32].

2.2.2 Postgraphene deposition processing

After graphene deposition the wafer is further processed in the cleanroom at Philips Innovation Services. As mentioned in the introduction of this chapter, the graphene membranes are created using a transferfree process. Applying standard lithography techniques the backside of the silicon wafer is patterned. Using a KOH-solution the wafer is anisotropically etched

[1] In the time period of this graduation project, Philips does not yet have the resources to grow graphene on location. Therefore the actual graphene deposition is outsourced, with the resulting thickness being determined through UV-vis spectroscopy as described in this thesis.

[2] Image adapted from Grachova *et al.* (2014) [32]

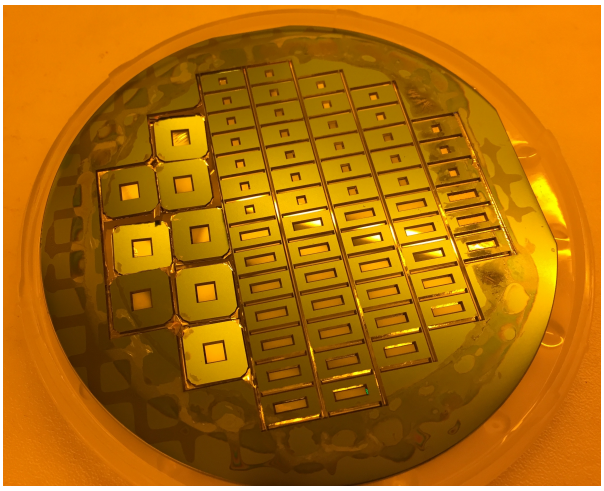

Figure 2.2: *4" graphene wafer after KOH-etching. The 5x1 mm^2 and 1x1 mm^2 bulge test samples can be identified, together with 3x3 mm^2 samples used for transmission spectroscopy.*

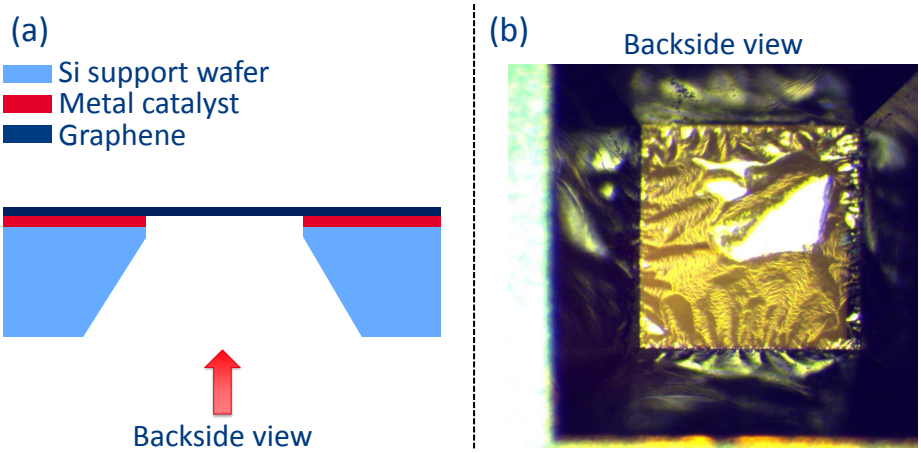

Figure 2.3: ***(a)*** *Schematic description of the graphene membrane after anisotropic KOH-etching and removal of the underlaying metal catalyst.* ***(b)*** *Backside microscopic image of an individual 1x1 mm^2 multilayer graphene membrane.*

along the vertical (100) direction and characteristic (111) planes become visible, see Figure 2.2. After wet-echting of the underlaying metal catalyst the freestanding graphene membranes are acquired, see Figure 2.3. The graphene is still supported by the silicon wafer on which it is grown, this creating the membranes on the same substrate wafer without the use of transfer.

After wet-etching of the metal catalyst, the final challenge in obtaining freestanding graphene membranes is an even drying process. After rinsing, the sample is air dried to let the remaining water evaporate. Due to the surface tension of water, caused by the strong hydrogen bonds between the water molecules, the graphene sometimes backfolds over itself, see Figure 2.4. Attempts are made to reduce the number of folds, for example by adding acetone to reduce surface tension. While this slightly reduces the number of folds, it is still an effect which has to be taken into account, especially in choosing the appropriate samples for bulging.

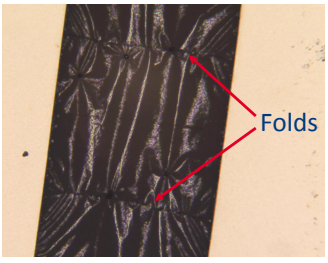

Figure 2.4: *Rectangular 5x1 mm^2 graphene membrane with folds along the full width of the membrane.*

2.3 Raman characterization

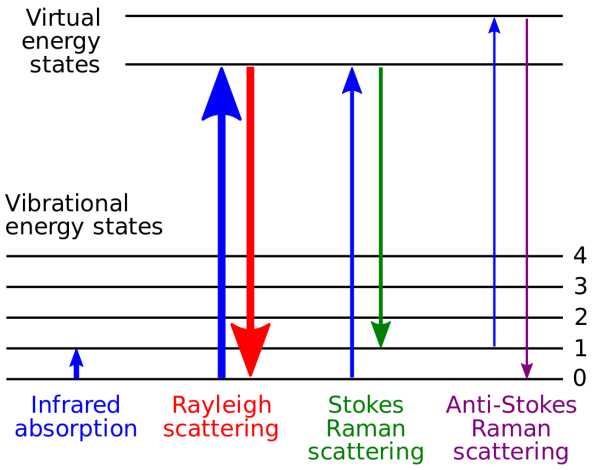

Figure 2.5: *Schematic illustration of the working principle of Raman scattering. Multiple transition paths are shown between the different energy levels. The Stokes Raman scattering and anti-Stokes Raman scattering cause minor shift in the emitted light, identified by the so-called Raman shift.*[3]

A typical technique to characterize (multilayer) graphene is Raman spectroscopy [35]. Raman spectroscopy uses low-frequency light to excite lattice vibrations, see Figure 2.5. By absorption of the light, the crystal is excited to higher virtual energy states. When falling back to lower energy states, the photons interact with the lattice vibrations, causing minor shift in the emitted wavelength. This so-called Raman shift can be used as fingerprint for specific crystal configurations and identification of lattice anomalies.

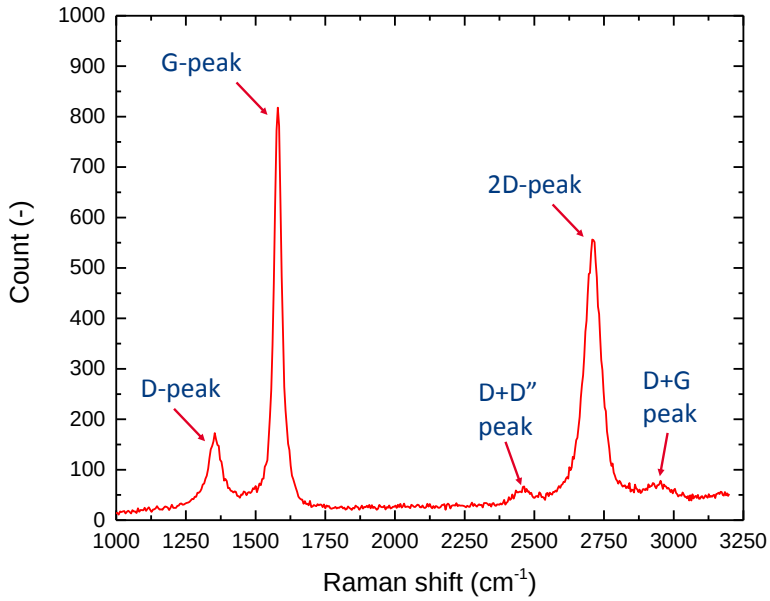

Figure 2.6: *Raman spectrum of freestanding type 1 multilayer graphene. The characteristic G- and 2D-peak can be distinguished, with the D-peak indicating defects present in the graphene. Higher order peaks (D+D" and D+G) can also be identified around the 2D-peak.*

[3]Image source: `https://en.wikipedia.org/wiki/Raman_spectroscopy`

Graphene is typically characterized by the presence of a *G*- and *2D*-peak in the Raman spectrum [36], see Figure 2.6. Indeed the multilayer graphene fabricated for this thesis shows the presence of *G*- and *2D*-peaks at the expected wavenumbers, 1579.8 ± 0.2 cm^{-1} and 2709.5 ± 0.5 cm^{-1}, respectively. The appearance of a peak at 1349.9 ± 0.2, the *D*-peak, indicates the presence of defects in the graphene [37, 38, 39]. Transitioning from single- to multilayer graphene, the intensity ratio $I(G)/I(2D)$ of the graphene Raman spectra changes [40]. Similarly, the structure of the 2D peak changes with increasing layers, from a single peak in the case of single-layer graphene, to multiple peaks for $N = 10$, similar to Raman spectra of graphite [41]. Surprisingly, the *2D*-peak in Figure 2.6 consist only of a single contribution, a characteristic of turbostratically grown graphene [42, 43].

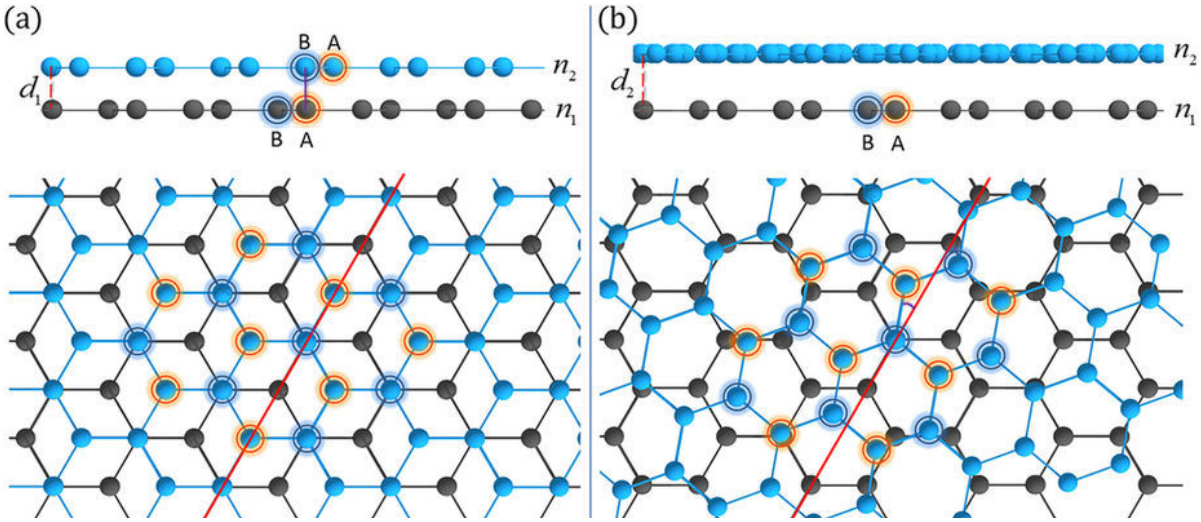

Figure 2.7: *Schematic representation of bilayer graphene in* ***(a)*** *Bernal, or AB, stacking order and* ***(b)*** *in the turbostratic configuration . Bernal stacking implies graphene layers are stacked with similar orientation directions, positioning the next layer such that the carbon atoms are aligned accordingly. Turbostratic graphene entails the graphene layers are stacked in random orientation directions.*[4]

In contrast to Bernal, or AB, stacked graphene, turbostratic graphene consists of graphene layers randomly stacked on top of each other, see Figure 2.7. Characteristic of turbostratic graphene is that the individual layers are electronically decoupled, having electronic properties resembling that of single-layer graphene [44]. This explains the fact turbostratic graphene's $2D$-peak consists of only a single contribution. Furthermore, this property is used to calculate the conductivity of multilayer graphene, which is discussed in detail in Chapter 3.

2.4 UV-vis experimental setup

UV-vis transmission experiments are performed using a homebuilt setup, schematically shown in Figure 2.8. The setup consists of three components: a broadband light source, optical fiber for direction ot the light, and a broadband detector. The broadband light is generated by an UV-vis light source (Mikropack DH-2000-BAL, 200 to 1118 nm). The light is guided through optical fibers towards a pinhole directly above the sample opening, over which a sample can be suspended. The optical path after transmission is similar to that before, continuing directly below the sample and guiding the collected light to a broadband detector.

[4]Image source: Garlow *et al.* (2016) [44]

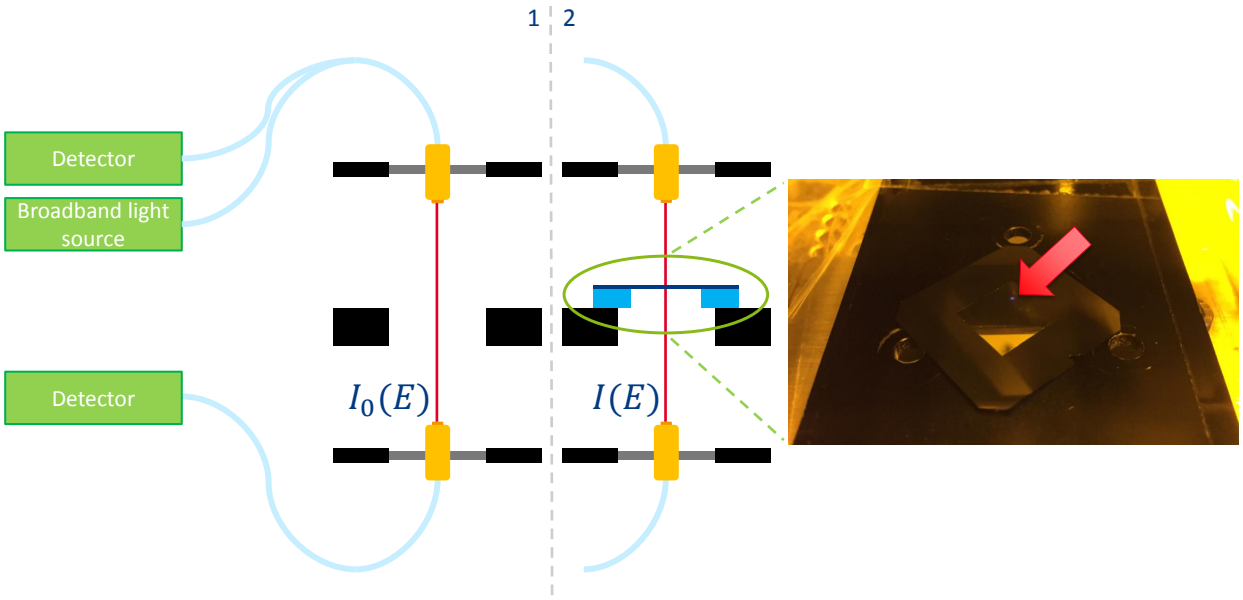

Figure 2.8: *Schematic representation of the homebuilt UV-vis transmission setup. The light is generated by a broadband light source and is guided through optical fiber to and from the sample where it is collected by a detector. The transmission spectrum is measured by comparing a baseline run (1) with a run including the light passing through a sample (2). Right: top view of a 11x11 mm^2 graphene membrane with the laser spot (∼1x1 mm^2) indicated.*

The transmission spectra are generated by comparing two individual measurements. First, a baseline spectrum $I_0(E)$ is acquired, in which the optical path is undisturbed (1). Second, the sample is placed in the optical path, resulting in different spectrum $I(E)$ (2). These measurements are converted to a transmission spectrum through

$$T(E) = \frac{I(E)}{I_0(E)} \tag{2.1}$$

Besides transmission this setup can also measure reflection. Reflection is determined by measuring the amount of light that reflects from the sample along the same line of normal incidence. It has to be noted that the spectrum collection, in both transmission and reflection, is limited to normal incident light only. Minimum random refraction and diffraction is expected for the extremely thin membranes studied in this work. Diffuse reflection however, could be an effect influencing the reflection spectra, depending on the surface roughness of the sample. This effect has to be taken into account when analyzing the reflection spectra.

2.5 Bulge test experimental setup

In this thesis the mechanical characteristics of the graphene membranes are determined through bulge testing. This experimental method involves pressuring a membrane from one side, causing a deflection, or bulging, of the membrane. Measuring the deflection pattern at different pressure setting, a characteristic bulging response can be distinguished. This response is mainly governed by the intrinsic material parameters, further discussed in Chapter 4. The bulge test setup consists of two main components: a sample holder able to pressurize the membrane from one side, and a profilometer used to accurately determine the membrane's deflection pattern. The experimental setup applied in this thesis is depicted in Figure 2.9, with a more detailed view on the bulge holder in combination with the profilometer shown in Figure 2.10.

Figure 2.9: *Experimental setup for bulge testing. The profilometer (Sensofar PLμ 2300) is placed in a temperature and shock-proof chamber. Both the sample location, supplied pressure and measurement setup can be controlled from outside of the controlled chamber.*

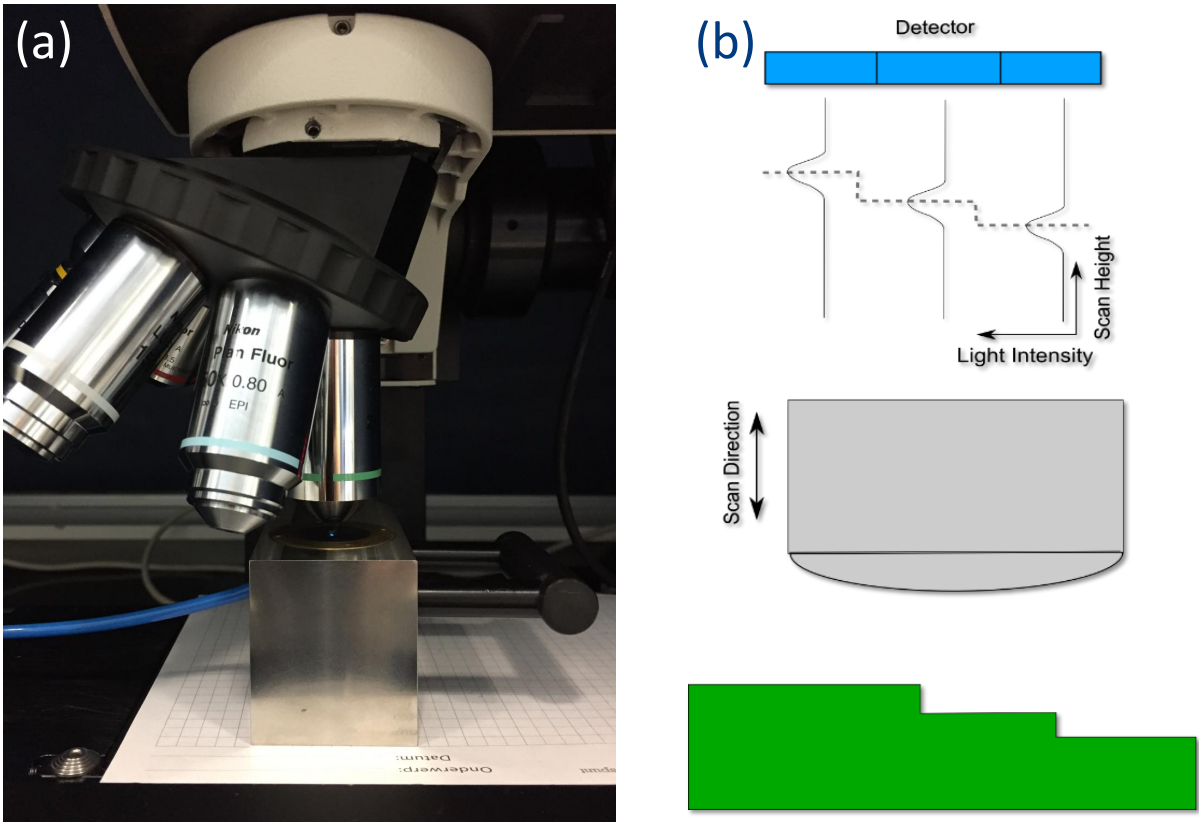

Figure 2.10: ***(a)*** *Image of the bulge sample holder placed directly beneath the rotating lens system of the profilometer.* ***(b)*** *Schematic description of the working principle of the profilometer.*

The membrane is placed in an aluminum holder with a hollow interior, sealed with a copper ring and connected to an inlet tube. The required pressure is supplied by a nitrogen tank connected to a pressure regulator (Fluigent MFCS-EZ), operating in the pressure range of 0-2000 mbar with a 0.03% (∼0.6 mbar) full range accuracy. The height profile of the membrane is scanned using an optical surface profiler Sensofar Plμ 2300, shown in more detail in Figure 2.10. The surface height of the sample is determined by fitting the intensity of the reflected light as function of the detector height. When at a certain height an object passes through the focal point of the lens, the reflected light intensity peaks. By simultaneously measuring the reflected intensity of the whole area as function of scan height the exact surface profile of the membrane can be determined.

Before initializing a bulge test run, the sample has to be horizontally leveled in order to have a correct starting point. This is done by using an interferometry objective which makes height differences directly visible by means of interference rings. Since the sample table can be tilted in both horizontal directions, the interference pattern can be used to place the sample aligned with the horizontal plane. During the bulging procedure the pressure is manually increased in increments of 1 mbar and after each pressure increase the membrane profile is extracted. The membrane profile is measured using a 20x objective which corresponds to an area of ∼650x500 μm^2 divided in an equidistant grid with 0.83 μm spacing.

Chapter 3

Thickness determination

This chapter focuses on UV-vis transmission spectroscopy of multilayer graphene membranes with the main purpose to determine the number of layers, and thus its thickness. After the introduction, a short literature overview on transmission spectroscopy of graphene is provided, indicating the added benefit of a full-range transmission model for multilayer graphene. The theoretical background on the transmission through and optical conductivity of single-layer graphene is discussed, followed by a detailed explanation of the proposed multilayer transmission model. This transmission model is compared with measurements on multilayer graphene membranes with different thicknesses.

3.1 Introduction

As the name suggests, single-layer graphene consist of only one layer of carbon atoms. Measuring the thickness of one-atom-thick materials is not as trivial as it may seem, requiring extremely accurate experimental techniques. Over the years different methods have been developed, each utilizing a different characteristic of graphene in order to determine its thickness. These methods can be optical by nature (reflection and contrast spectroscopy [45, 46], using surface plasmon resonance [47]), electronic properties (Scanning Electron Microscopy (SEM) [48]), using crystal features (X-ray diffraction [49]) or simply direct height measurements (Atomic Force Microscopy (AFM) [50]).

While all these methods have been perfected to determine the thickness of single-layer graphene, multilayer graphene requires a different approach. For multilayer graphene thicknesses, Raman spectroscopy, AFM and transmission spectroscopy are the most suitable experimental methods. Raman spectroscopy can however only distinguish up to 10 layers of stacked graphene, making it less useful for thicker graphene membranes [41]. AFM provides a more direct measurement of its thickness, but experimental fluctuations due to surface roughness are in the order of nanometers, reducing its accuracy to several layers. Transmission spectroscopy, on the other hand, can extend its reach beyond 10 layers and being a non-invasive technique, it is extremely suitable to determine the thickness of multilayer graphene.

It is generally assumed that light absorption in graphene is constant over a broad wavelength regime. In the infrared regime, the 'constant' absorption of 2.3% for single-layer graphene is valid, but absorption can reach up to 10% around ~ 5 eV (≈ 250 nm). Determining multilayer graphene thickness with transmission spectroscopy is usually performed at a single wavelength. This method requires *a priori* input on optical parameters of graphene before acquiring its thickness. Since the light absorption of single-layer graphene is not constant in the UV-vis regime, choosing one specific wavelength can lead to discrepancies. These discrepancies become

larger in the case of multilayer graphene. A full-range transmission model can take into account the non-constant light absorption, avoiding any discrepancies between optical properties of transmission measurements at specific wavelengths. Additionally, this thesis shows such a full-range multilayer transmission model can be used to model the reflected intensity of the light, a property which is generally neglected for single- and few-layer graphene.

3.2 Conventional transmission spectroscopy on graphene

Within transmission spectroscopy multiple data analysis procedures exist to determine the thickness of a semi-transparent material. These procedures require input on the theoretical or experimentally determined optical properties of the material. One method exploits the relation between the transmission T, reflection R and absorption coefficient α [51]

$$T = \frac{(1-R)^2 e^{-\alpha t}}{1-R^2 e^{-2\alpha t}} \quad \text{with} \quad \alpha = \frac{4\pi k}{\lambda}, R = \left|\frac{\widetilde{n}-1}{\widetilde{n}+1}\right|^2 \tag{3.1}$$

with t the thickness, λ the wavelength and $\widetilde{n} = n + ik$ the complex refractive index of the material. A different approach is adopted by Kim *et al.* (2014), applying the Beer-Lambert law to determine the thickness of a multilayer graphene stack [22]

$$T = e^{-4\pi k t/\lambda} \tag{3.2}$$

which essentially is the same as Equation 3.1 with $R = 0$, an assumption valid only in the case of few-layer graphene. Figure 3.1 shows a typical transmission spectrum for multilayer graphene. Table 3.1 shows several literature references of the optical properties of graphene, used to calculate the thickness from the transmission spectrum of the multilayer graphene in Figure 3.1. From these figures two main complications arise in determining the thickness:

- In the UV-visible regime the transmission spectrum is not flat, giving rise to the discussion at which wavelength the transmission and optical properties have to be determined.
- Both formulas 3.1 and 3.2 assume the material is a continuous absorbing material. Generally this assumption is valid. However, graphene approaches the thickness limit in terms of a finite, countable number of atomic layers, requiring an approach which incorporates the discrete number of absorbing layers.

In literature the first problem is circumvented by the convention to determine the optical properties at $\lambda = 550$ nm. Unfortunately, as Table 3.1 shows, different experimentally determined values for $\widetilde{n}$ consequently result in different thicknesses t for the **same** transmission measurement and an alternative is needed. The second problem requires a more detailed examination of the optical properties of graphene, how these evolve over multiple layers, and lastly how they relate to the transmission.

Table 3.1: *Optical properties of graphene at λ = 550 nm. The thickness t is calculated from the **same** transmission data in Figure 3.1 at 550 nm using the literature and Equation 3.1.*

Reference	Refractive index $\widetilde{n}$	Graphene thickness t (nm)
Jellison *et al.* (2007), experimental [52]	$2.52 + 1.94i$	3.08
Skulason *et al.* (2010), theoretical [53]	$1.88 + 1.59i$	8.05
Skulason *et al.* (2010), experimental [53]	$2.92 + 0.77i$	20.74
Kim *et al.* (2014), theoretical [22]	$1.30i$ (Beer-Lambert)	32.56

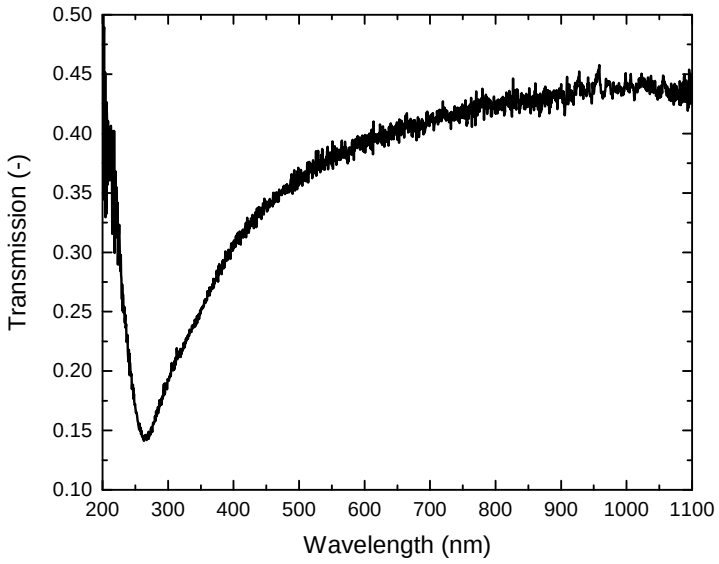

Figure 3.1: *Typical UV-vis transmission spectrum for a multilayer graphene membrane studied in this thesis.*

Both these problems can be solved by considering the transmission over the full wavelength regime over which it is measured. Combining the full range transmission with a discrete number of layers in a multilayer graphene stack, it is possible to create a more robust transmission model. Key in this model is to correctly model the full range transmission of single-layer graphene, before extending this method to a multilayer graphene stack. Therefore, in the next two sections first conventional 'constant' light absorption and the energy depence of the optical conductivity is discussed, after which the transmission is extended to multilayer graphene.

3.3 Single-layer graphene universal conductivity σ_0 and light transmission

Nair *et al.* (2008) have shown that graphene absorbs 4 ∼2.3% of light over a broad wavelength range [54]. This constant absorption is a results of the valence and conductance band having a linear dispersion around the so-called Dirac point. This leads to a constant transmission T and a universal optical conductivity σ_0

$$T = \left(1 + \frac{\sigma_0}{2c\epsilon_0}\right)^{-2} \approx 1 - \frac{\sigma_0}{c\epsilon_0} = 1 - A \tag{3.3}$$

with c the speed of light, ϵ_0 the vacuum permittivity and σ_0 given by

$$\sigma_0 = \frac{e^2}{4\hbar} \tag{3.4}$$

resulting in an absorption $A = 2.3\%$, which indeed has has been confirmed in the transmission experiments, see Figure 3.2.

Although not explicitly mentioned by Nair *et al.*, their experimental data shows that transmission slightly decreases towards shorter wavelengths. Indeed when photon energy increases the graphene energy bands start to deviate from the linear dispersion around the Dirac point and the conductivity σ does become dependent upon the photon energy. Especially around the saddle point in the conductance band the conductivity peaks, resulting in a higher absorption [55].

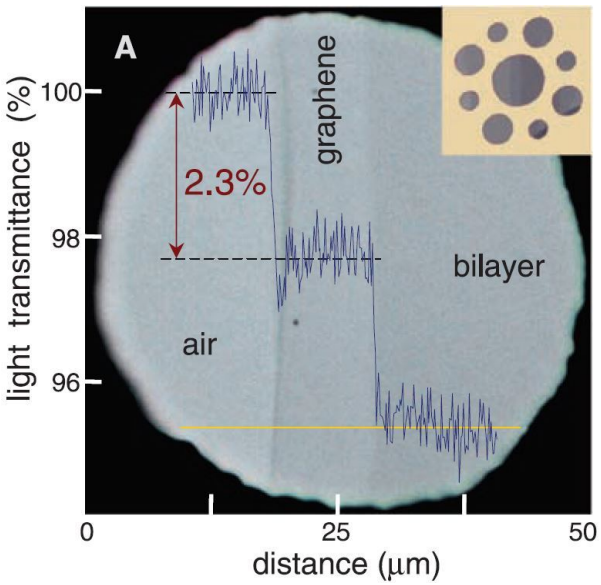

Figure 3.2: *Single- and bilayer graphene white light transmission as measured by Nair et al. (2008).*[1]

Besides the saddle point singularity, it has also been observed that the presence of excitons has a considerable effect on the absorption of light in the UV-vis regime, enhancing the absorption up to four times the regular 2.3% [56, 57]. This large absorption difference in the UV-vis range of the electromagnetic spectrum indicates that it is not enough to only take into account the universal optical conductivity σ_0, but that energy dependence has to be considered. In the next section this energy dependence will be described in more detail.

3.4 Energy depence of the conductivity of single-layer graphene

Before extending the transmission from single-layer to multilayer graphene, the energy dependence of the conductivity has to be discussed, $\sigma_0 \rightarrow \sigma(E)$. First, the optical conductivity of single-layer graphene is modeled, after which the Fano-resonance effect is introduced, showing to have a profound effect on the optical conductivity of single-layer graphene.

3.4.1 Empirical single-layer graphene conductivity model

In the infrared region the optical conductivity of graphene approximates the universal optical conductivity σ_0 of Equation 3.4. When the photon energy increases, the optical conductivity also increases to a maximum around the saddle point in the conductance band. At this point the joint density of states (JDOS) ρ has got a singularity which leads to a peak in the conductivity [58].

An empirical approach to describe the optical conductivity around the saddle point can also be adopted. Here by considering the two main effects in the UV-vis wavelength range are considered: the constant universal optical conductivity σ_0 and the absorption peak at the singularity point [56, 59, 60]. Around the singularity the optical conductivity can be described by $\sigma \sim -\log(E)$, is used to approximate the total optical conductivity in the UV-vis regime

$$\sigma(E)/\sigma_0 = 1 - \log|1 - E/E_0| \tag{3.5}$$

[1] Image source: Nair *et al.* (2008) [54]

with $E_0 = 2t$ the saddle-point energy of the singularity and t the nearest-neighbor hopping parameter in the C−C lattice. The constant term 1 is used to represent the background universal optical conductivity σ_0.

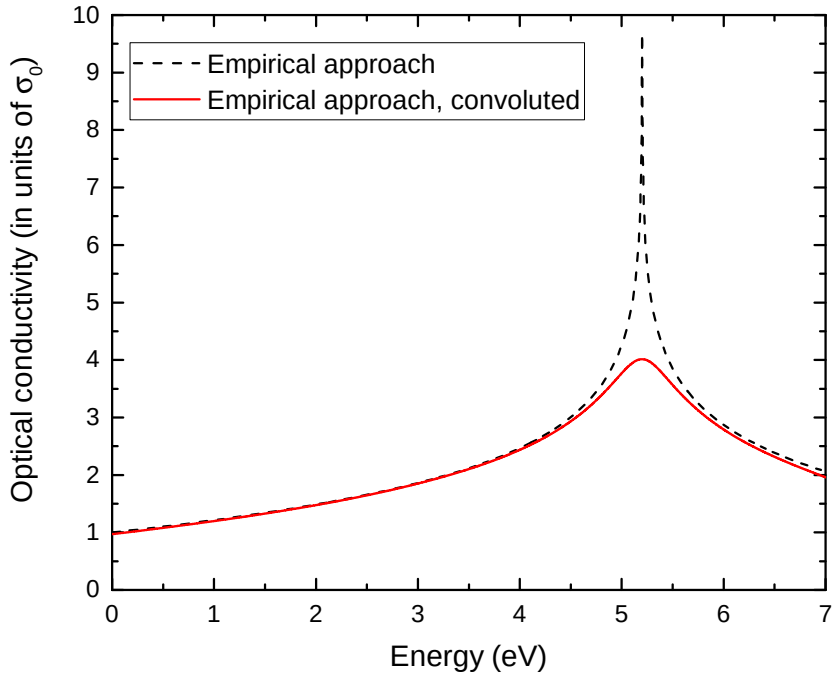

Figure 3.3: *Optical conductivity of single-layer graphene according to the empirical approach* $\sigma \sim -\log|1 - E/E_0|$. *Equation 3.5 is also shown convoluted with a Lorentzian (width = 250 meV) to account for experimental broadening.*

In Figure 3.3 the empirical description for $\sigma(E)$ is plotted (black line). To account for experimental broadening, Equation 3.5 is also plotted convoluted with a Lorentzian with a width of 250 meV [56] (red line). Noticeably, the convolution smears out the peak, resulting in a less intense peak around the singularity. The convoluted empirical formula reaches a height of ∼4.0 σ_0. Despite the relatively elementary approach in describing $\sigma(E)$, it agrees well with numerical tight-binding bond-orbital, so called *GW*, calculations [58]. These numerical calculations confirm that the optical conductivity of graphene is close to σ_0 in the infrared region and rises to a height of $4\sigma_0$ at its maximum, similar to the model shown here. This indicates that the empirical formula for the optical conductivity is indeed representable for single-layer graphene in the UV-vis regime.

3.4.2 Exciton effect: Fano resonance and its effect on optical conductivity

In the previous section the optical conductivity has been determined by empirical approximation of the band structure. While the empirical formula does give an accurate description of the intrinsic properties of graphene, measurements on the optical conductivity show a different response then predicted by the convoluted empirical model in Figure 3.3 [61]. Main observation is the redshift of the conductivity peak from the expected 5.2 eV to ∼4.6 eV, together with a profound asymmetry of the peak. Yang *et al.* (2009) [58] observe a similar effect on the absorbance of graphene when incorporating electron-hole interactions in their *GW*-calculations. Mak *et al.* (2011) [56] and Chae *et al.* (2011) [57] describe this effect as the presence of an exciton state existing within the continuum band structure of graphene, see Figure 3.4.

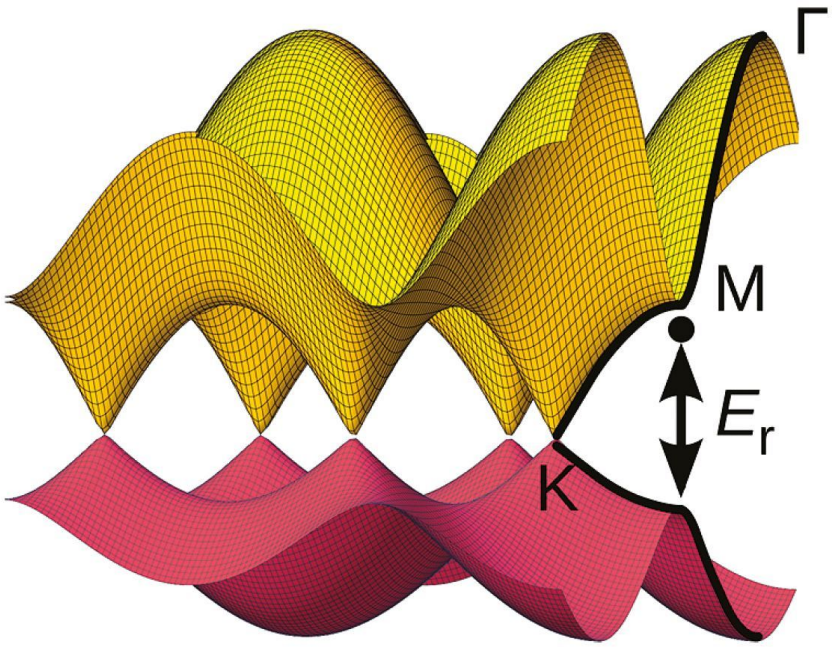

Figure 3.4: *Conductance (yellow) and valence (red) band of graphene. The maximum of the conductance band (Γ) and the linear dispersion around the Dirac point (**K**) can be distinguished. Point of interest is the saddle point **M** where the exciton state with resonance energy E_{res} is schematically shown.*[2]

The excitonic effect can quantitatively be described by resonance between the continuum background optical conductivity and the exciton state, an effect first described by Fano in 1961 [62]. Combining this Fano resonance with the optical conductivity results in [56, 57]

$$\frac{\sigma_{Fano}(E)}{\sigma_{cont}(E)} = A\frac{(q+\epsilon)^2}{1+\epsilon^2} \quad \text{with} \quad \epsilon = \frac{E - E_{res}}{\Gamma/2} \tag{3.6}$$

where q^2 is the strength of the coupling between the excitonic transition and the continuum energy bands, ϵ the normalized energy in which E_{res} equals the resonance energy and Γ the phenomenological width of the excitonic state. Lastly, A is a scaling factor, since from measurements it is known the optical conductivity reaches σ_0 at lower energies and $\sim 4\sigma_0$ at its maximum. Without this factor the overall effect would be too large and does not correspond to literature references on the Fano resonance effect. A is chosen such that the resulting conductivity always peaks at $\sim 4\sigma_0$.

Figure 3.5 shows the optical conductivity σ_{cont} (black), the non-scaled effect of the Fano multiplication σ_{Fano}/A (green) and the resulting optical conductivity σ_{Fano} (blue). The continuum optical conductivity σ_{cont} from Equation 3.5 results in a symmetrical peak around the singularity. Since in high and low energy limits the Fano resonance goes to 1, the continuum optical conductivity is not affected and thus $\sigma_{Fano} = \sigma_{cont}$. Around the exciton resonance energy E_{res} though, an asymmetric resonance takes place, with its maximum just below the resonance energy. When multiplied with the continuum optical conductivity σ_{cont}, this results in an asymmetric signal σ_{Fano}/A. This response is scaled down by A, leading to the single-layer graphene optical conductivity σ_{Fano}, shown by the blue line in Figure 3.5. Despite a relative empirical description, the optical conductivity σ_{Fano} matches measurements on single-layer graphene as reported by Mak *et al.* (2011), Gogoi *et al.* (2012) and Santoso *et al.* (2014) [56, 59, 60].

[2]Image source: Chae *et al.* (2011) [57]

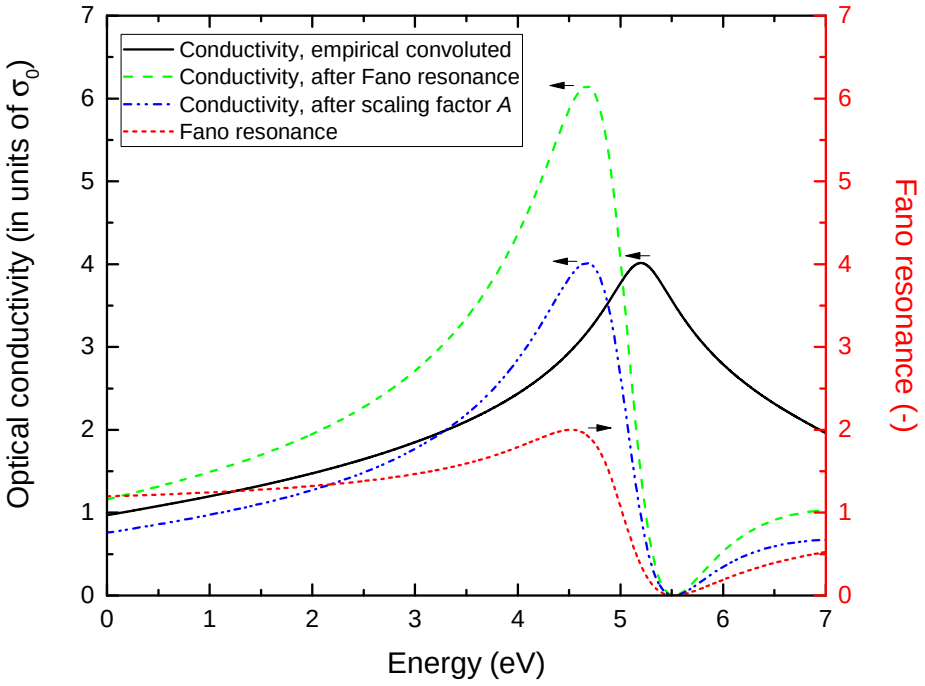

Figure 3.5: *Optical conductivity before Fano resonance (empirical convoluted) and after multiplication with the Fano resonance ($q = -1$, $E_{res} = 5.02$ eV and $\Gamma = 1.0$ eV). The resulting, scaled, optical conductivity corresponds to literature references in the range of 1.0 to 5.0 eV.*

3.5 Multilayer graphene UV-vis transmission

After describing the optical conductivity of single-layer graphene, the model is extended to calculate the transmission through a stack of multilayer graphene. From first principle optical calculations it follows the transmission T, reflection R and absorption A of a freestanding thin film are related to the conductivity of the film by [63]

$$T = \frac{1}{\left|1 + \widetilde{\sigma}_{tot}/2c\epsilon_0\right|^2} \tag{3.7}$$

$$R = \left|\frac{\widetilde{\sigma}_{tot}/2c\epsilon_0}{1 + \widetilde{\sigma}_{tot}/2c\epsilon_0}\right|^2 \tag{3.8}$$

$$A = \frac{\mathrm{Re}(\widetilde{\sigma}_{tot})/c\epsilon_0}{\left|1 + \widetilde{\sigma}_{tot}/2c\epsilon_0\right|^2} \tag{3.9}$$

in which $\widetilde{\sigma}_{tot}$ represents the total (complex) optical conductivity of the thin film. Considering the UV-vis regime, the imaginary part of the conductivity is negligible [64], simplifying the formulas above. As shortly discussed in section 2.3, specifically in turbostratic multilayer graphene, it has been shown that the conductivity scales linearly with the number of layers N

$$\sigma_{tot} = N\sigma_{SLG} \tag{3.10}$$

with σ_{SLG} the optical conductivity of a single-layer of graphene [65]. Stacking order of the graphene layers does influence the optical conductivity of the total stack in certain configurations, amongst others AB/Bernal stacking, but mainly at energies $E < 1.0$ eV [66]. Since this thesis focuses on the UV-vis region from 1.0 to 5.0 eV, it can be safely assumed the conductivity scales linearly with N.

From the optical formulas shown above it follows that $R \sim \sigma_{tot}^2$ and reflection indeed can be ignored in the case of single- and few-layer graphene. In multilayer graphene though, the conductivity increases linearly according to Equation 3.10 and reflection cannot be neglected.

Zhu *et al.* (2014) [24] were the first to explicitly apply the correlation between the transmission and conductivity to multilayer graphene according to

$$T(E) = \left(1 + N\frac{f(E)\sigma_0}{2c\epsilon_0}\right)^{-2} \tag{3.11}$$

with $f(E) = 1.13$ a correction factor to account for the deviation of the optical conductivity at 550 nm compared to the universal optical conductivity σ_0. Although this model captures the energy dependence of the optical conductivity, still only one wavelength is used to determine the number of layers N. Furthermore the correction factor $f(E)$ has been determined empirically from the conductivity of a single-layer of graphene, raising questions on the impact of small deviations in this factor for large values of N.

Instead of using a correction factor for the optical conductivity as applied by Zhu *et al.*, a full-range UV-vis description of the optical conductivity based on the Fano resonance principle is adopted. The transmission is given by Equation 3.7, in which the total conductivity σ_{tot} is given by Equation 3.10 and the single-layer conductivity σ_{SLG} by Equation 3.6. This leads to the overall transmission formula

$$T(E, N, q, E_{res}, \Gamma) = \left(1 + N \cdot \frac{\sigma_{Fano}(E, q, E_{res}, \Gamma)}{2c\epsilon_0}\right)^{-2} \tag{3.12}$$

In this formula 4 parameters have to be determined by fitting the equation:

- q the Fano coupling parameter,
- E_{res} the resonance energy of the exciton,
- Γ the phenomenological width of the excitonic state,
- N the number of graphene layers.

Potentially a fifth fitting parameter can be added. If there is any indication the graphene lattice is slightly distorted, the singularity energy can be shifted from the pristine graphene value of $E_0 = 5.2$ eV as used until now:

- E_0 the saddle point energy of the JDOS singularity from Equation 3.5.

From Equation 3.12 the parameter of interest N can be determined. To establish the thickness of the graphene, the number of layers is multiplied with the distance between the graphene layers

$$t = Nd \tag{3.13}$$

with d the interlayer distance. In line with literature, d is chosen equal to the interlayer distance in graphite crystals $d = 3.35$ Å [44, 47]. In the next section the derived model for multilayer graphene is fitted with measurement data for different multilayer thicknesses.

3.6 UV-vis results

The UV-vis measurements are performed in the range of 200 to 1118 nm, in which the 250 to 1100 nm (4.96 to 1.13 eV, respectively) is used to fit the transmission model. The main objective is to determine the number of layers N of the graphene membrane. Multiple spots on the same membrane are measured to confirm growth uniformity. Similarly, different graphene membrane thicknesses are compared to investigate the validity of the model and cross-referenced with reflection data.

3.6.1 Conductivity fitting and growth uniformity

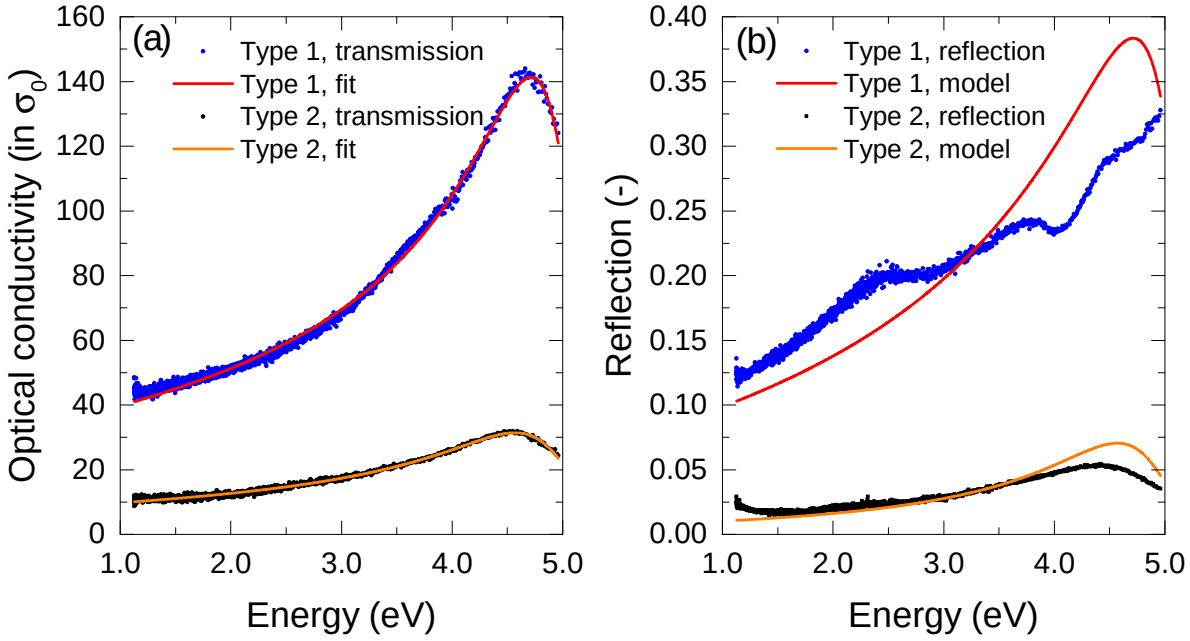

Figure 3.6: ***(a)*** *Optical conductivity extracted from two transmission spectra on type 1 (blue) and type 2 (black) graphene with corresponding model fits. The fit parameters are reported in Table 3.3.* ***(b)*** *Measured and modeled reflection of the same transmission measurements.*

Figure 3.6a shows the optical conductivity of type 1 and type 2 graphene, calculated from the corresponding transmission spectra using Equation 3.7, and the corresponding fits. The nearest-neighbor hopping parameters $t = 2.70$ and 2.88 match literature values reported between $t = 2.5$ and 3.0 eV from first principle calculations [64, 67]. This agreement indicates the carbon atoms are arranged in a not too severely distorted graphene lattice. Comparing the Fano fit values to literature values, see Table 3.2, some discrepancies become apparent: The relatively low coupling parameter q and high resonance energy E_{res} indicate smaller interaction

Table 3.2: *Comparison of the Fano parameters from the fits in Figure 3.6 with literature values reported for single-layer graphene.*

Parameter	Type 1	Type 2	Mak (2011) [56]	Gogoi (2012) [59]	Santoso (2014) [60]
Hopping parameter t (eV)	2.70	2.88	2.60 (fixed)	2.60 (fixed)	2.60 (fixed)
Fano coupling q (-)	-0.83	-1.00	-1.00	-1.16	-1.10
Exciton resonance E_{res} (eV)	5.18	5.05	5.02	4.90	4.94
Resonance width Γ (eV)	1.11	1.34	0.78	0.99	0.93
Number of layers N (-)	34	8	-	-	-

between the exciton and the graphene lattice in multilayer graphene and more energy needed to excite the exciton. This observation is supported by recent simulation models which show the small binding energy of excitons in multilayer graphene (∼0.05 eV) compared to single-layer graphene (∼0.5 eV) [68]. Similarly, the broad phenomenological width Γ signals an extremely short lifetime ($\Delta E \Delta t \geq \hbar/2$: $\Delta t = 0.30$ fs) possibly originating from defects in the membrane such as grain boundaries, already observed in the Raman spectra in Chapter 2. Since excitons essentially are electron-hole pairs, defects points are ideal recombination locations.

The conductivity is also related to the reflection according to Equation 3.8, being able to compare the model with the measured reflection. Figure 3.6b shows the measured reflection and modeled reflection based on the transmission fits. Although the measured reflection follows the same upward trend as the model, and does overlap in the lower energy regime, the discrepancy becomes larger towards higher energies. Since only normal incident light is captured by the reflectance detector, diffuse reflected light is lost, resulting in lower reflection than modeled. Diffuse reflection can especially be large if the surface roughness is in the order of the wavelength. The type 1 graphene indeed shows signs of more surface roughness, possibly enhancing the amount of diffuse reflection. This might account for the fact the deviation from the upward trends occurs at lower energies in the type 1 graphene compared to the type 2 graphene.

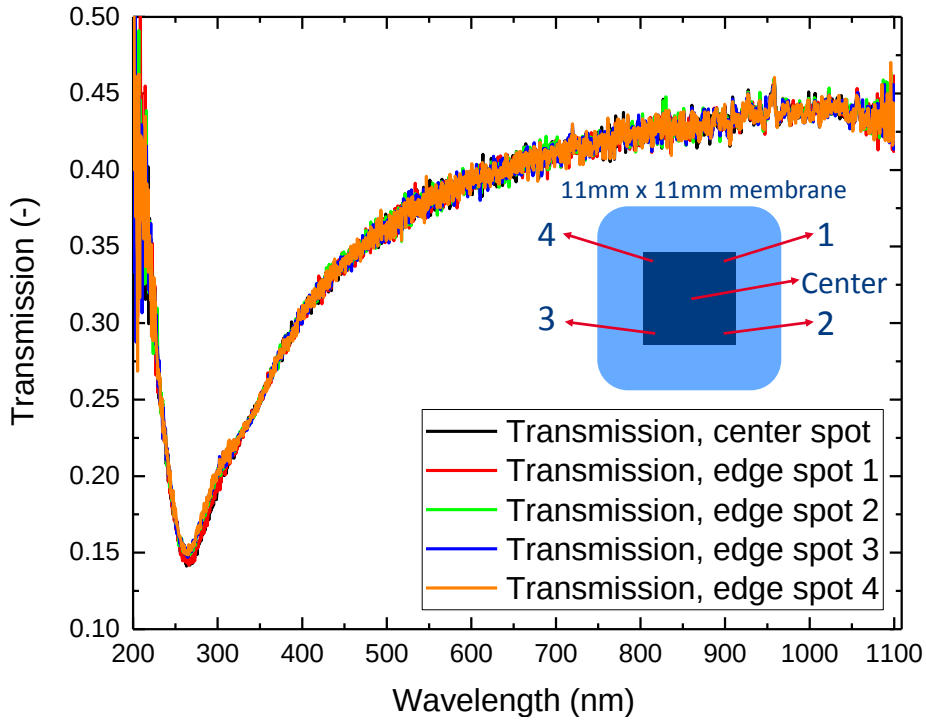

Figure 3.7: *Transmission spectra measured for five spots on an 11x11 mm^2 type 1 multilayer graphene membrane. Inset: schematic sample description with measurement locations.*

Figure 3.7 shows multiple transmission spectra on a multilayer graphene membrane suspended over an 11 mm by 11 mm square opening. The transmission spectra do not differ significantly, suggesting the multilayer graphene is uniform in its thickness over areas in the order of millimeters. Fitting the different transmission curves, the corresponding parameters show some localized discrepancies, see Table 3.3, which also might be due to artificially small error margins. The number of layers on the other hand is very consistent around $N = 34$, resulting in an overall thickness of 11.5 nm.

Table 3.3: *Fitting parameters for the five transmission spectra shown in Figure 3.7. For each transmission measurement all the five parameters are fitted.*

Model parameters	Center spot	Spot 1	Spot 2	Spot 3	Spot 4
$t = E_0/2$ (eV)	2.62 ± 0.01	2.64 ± 0.01	2.70 ± 0.04	2.71 ± 0.08	2.74 ± 0.09
q (-)	-0.83 ± 0.03	-0.84 ± 0.01	-0.83 ± 0.01	-0.83 ± 0.05	-0.84 ± 0.07
E_{res} (eV)	5.13 ± 0.01	5.14 ± 0.02	5.18 ± 0.01	5.184 ± 0.009	5.170 ± 0.006
Γ (eV)	1.067 ± 0.008	1.06 ± 0.01	1.11 ± 0.02	1.10 ± 0.02	1.06 ± 0.02
N (-)	35 ± 6	35 ± 7	34 ± 7	34 ± 2	33.4 ± 0.4
Thickness (nm)	12 ± 2	12 ± 3	11 ± 2	11.2 ± 0.8	11.2 ± 0.1

To directly verify the thickness of the multilayer graphene, AFM measurements are performed on a transferred piece of type 1 graphene. Figure 3.8 shows the average height profile along 10 AFM line scans. It can be seen the AFM measurements suffer from large height variations, largely caused by the transfer procedure. Due to the large height variations it is difficult to determine thickness of the graphene over a large area. The graphene is crumpled due to drying and possible imprint of the metal substrate. Therefore it is assumed the graphene is more evenly positioned along the silicon substrate at the transition from graphene to silicon. The height of different 'plateaus' is determined by fitting a linear relation on the flat silicon surface and fitting the graphene height using a linear relation with the same slope. Along the edge of the graphene a region can be distinguished where the graphene has back-folded, also giving results on double the thickness. The different plateaus correspond to an average graphene thickness of 12 ± 2 nm, in agreement with 11 ± 0.5 nm found in the UV-vis full range model. The AFM height error is estimated to be in the order of nanometers, mainly due to tip-substrate interactions and possible residual water between the silicon wafer and the transfered graphene [50].

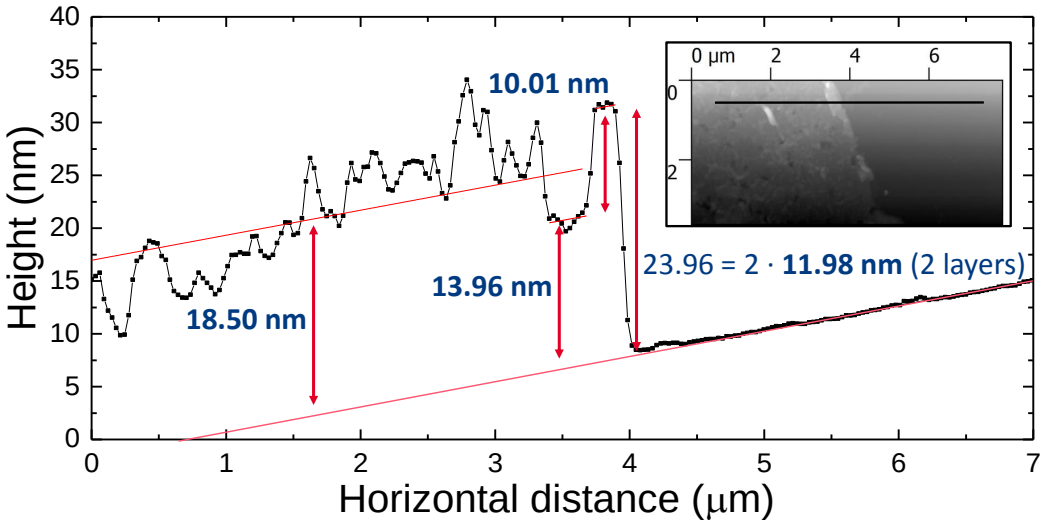

Figure 3.8: *AFM line scan of transferred type 1 graphene on a clean piece of silicon. The datapoints are averaged over 10 horizontal linescans. Inset: AFM map of the transferred multilayer graphene and indicated region of the linescan.*

3.7 Conclusion

In this chapter a full-range UV-vis transmission model (∼250-1100 nm) is proposed for multilayer graphene. The correlation between the transmission and linear scaling conductivity is combined with the Fano resonance effect observed in single-layer graphene. This results in a more robust method to determine the thickness of multilayer graphene compared to previous models, which in general only use a single wavelength as reference for thickness calculations.

The full-range UV-vis transmission model has been fitted on transmission measurements from two type of multilayer graphene membranes. The model is fitted with the available data and confirms growth uniformity on a centimeter scale. The experimentally found membrane thickness is verified with AFM measured on transfered graphene. Additionally, this model is used to predict reflection spectra, which are compared with reflection measurements. The modeled reflection shows a similar upward trend as the reflection measurements. Deviations towards higher energies are most likely due to diffuse reflection. Since the detector only captures normal incident light, diffuse reflection is not captured. Added benefit of the UV-vis model is that information on excitonic effects in graphene is acquired. The graphene membranes show a higher than previously reported exciton resonance energy. Furthermore, a relatively low exciton coupling is observed, which can be explained due to low binding energy of excitons in multilayer graphene. Additionally, very short exciton lifetimes (∼30 fs) are observed, mainly attributed to defects in the membrane.

Since in this thesis only normal incident light is measured, the reflection of graphene membranes can be studied in more detail with angular detectors collecting light in all angular directions. This can be used to verify the model for diffuse light reflection. The excitonic effects can also be studied in more detail, for example determining the influence of the defect density on the exciton lifetime.

Chapter 4

Membrane characterization: bulge testing

In this chapter, graphene membranes are mechanically characterized by means of bulge testing. After the introduction, the main material characteristics Young's modulus E and Poisson ratio ν are explained. The principle behind bulge testing is illustrated in detail, clarifying the methods to determine the stress and strain exerted in different membrane configurations. Stress-strain curves of two configurations are analyzed to independently determine the Young's modulus and Poisson ratio. The membranes exhibit a non-linear response which is quantitatively described using a literature model based on the crumpling of graphene membranes. Lastly, the effect of varying thickness on the stiffness and strength of the graphene membranes is discussed.

4.1 Introduction

Graphene is amongst others known for its large strength-to-weight ratio, an ability used to create ultrathin, but extremely strong membranes. These membranes can be used for filtering purposes [4, 5], optical windows [23, 69] or electromechanical resonators [70]. Since each of these applications requires certain minimum standards of the graphene membranes, it is of importance to acquire information on its mechanical properties. This thesis focuses on characterizing the Young's modulus E and the Poisson ratio ν of the multilayer graphene menbranes. The Young's modulus in particular has been thoroughly investigated for both single- and multilayer graphene. Pristine single-layer graphene is commonly accepted to exhibit a value of $E \approx 1$ TPa [71]. This high stiffness establishes graphene as an extremely thin but at the same time exceptionally strong material. Extending into multilayer graphene, a decrease in stiffness is observed [72]. Since these multilayer graphene membranes are currently also used for applications at Philips, it is of interest to determine the exact stiffness of the multilayer graphene membranes.

In literature the stiffness of graphene has been investigated using a broad variety of techniques, ranging from numerical simulations on graphene bending [25] and Raman spectroscopy [73], to nanoindentation [74], high-resolution electron energy loss spectroscopy [75] and more recently bulge testing [26, 76]. The method of bulge testing has become an almost standard characterization technique for thin film membranes, i.e. μm thick silicon nitride membranes [77]. Although bulge testing has been applied to single-layer, transfered graphene membranes, it has only been used in a limited pressure range and in one single, relatively small ($\sim \mu m$) configuration. In this thesis we extend the bulge testing method to millimeter size, non-transfered graphene membranes.

Additionally, while current research mainly focuses on analyzing the Young's modulus of graphene membranes, this work also determines the Poisson ratio independently from the Young's modulus. The Poisson ratio of single- and multilayer graphene is generally assumed to be constant around $\nu \approx 0.16$ [26, 76], after which it is used to derive the Young's modulus of the graphene. In this thesis, by using different membrane configurations, the Young's modulus E and the Poisson ratio ν are determined independently without making *a priori* assumptions on material parameters. The following section provides a short introduction on the theory behind the Young's modulus and Poisson ratio.

4.2 Young's modulus E and Poisson ratio ν

In order to describe the multilayer graphene membrane's mechanical response, two fundamental material characteristics have to be determined: the Young's modulus E and Poisson ratio ν. The Young's modulus is defined by

$$E \equiv \frac{\sigma}{\epsilon} \tag{4.1}$$

in which σ and ϵ are the stress and the strain, respectively. The stress is defined by $\sigma \equiv F/A$, in which with F the applied force and A the pressurized surface area, and can be seen as a measure for pressure. The strain $\epsilon \equiv \Delta L/L_0$ can be interpreted as the amount of relative expansion of the material, in which ΔL is the change in length and L_0 the initial length of the object. An intuitive interpretation of the Young's modulus is the stiffness of a material, since it essentially indicates how much pressure is needed to stretch the material a certain amount. This can also be seen when rewriting Equation 4.1 into

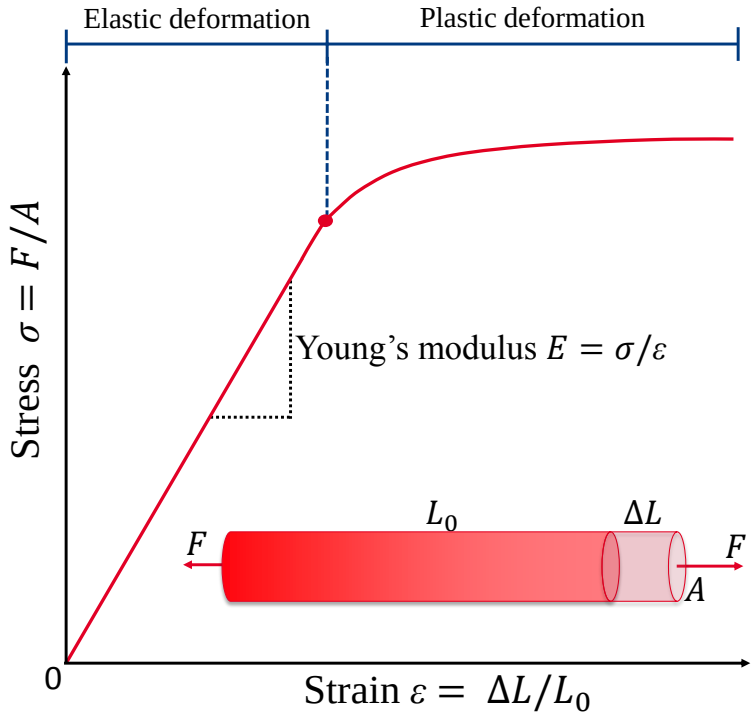

Figure 4.1: *Typical stress-strain curve of a material when subjected to a stretching force. Examining Equation 4.1, the Young's modulus can be perceived as the slope of the curve. At a certain point the material deviates from linear (elastic) deformation and shows permanent (plastic) deformation, perceived by the decreasing slope of the curve.*

$$F = \frac{EA}{L_0}\Delta L = kx \tag{4.2}$$

which can be interpreted as Hooke's law for extension or compression with a spring constant of $k = \frac{EA}{L_0}$ for a deformation length of x.

Figure 4.1 shows a typical stress-strain curve as measured in bulge testing. Following Equation 4.1, the slope of the curve can be identified as the Young's modulus E. In general all materials follow a linear stress-strain relation at low stress. In this regime the expansion is an elastic and thus reversible process. Beyond a certain stress level any material will start to undergo irreversible changes. Ceramic materials will break at the end of their linear mechanical response regime, while other materials such as metals show their stress-strain curves leveling off. This process essentially indicates permanent or plastic deformation of the material, resulting in less stress needed to deform the same length of material. Most materials follow this trend, with exception of a special class of materials: hyperelastic materials [78]. The stress-strain curve of a hyperelastic material does not follow a linear trend, but actually becomes steeper with increasing strain, the opposite of what is shown here. Certain rubbers and mechanically engineered foams can behave hyperelastically, meaning they become more stiff when stretched out further. In other words: the stress-strain slope, and thus Young's modulus, becomes larger. This deformation still happens **elastically**, meaning it is an intrinsic material characteristic and not a failure mechanism such as the plastic regime in metals.

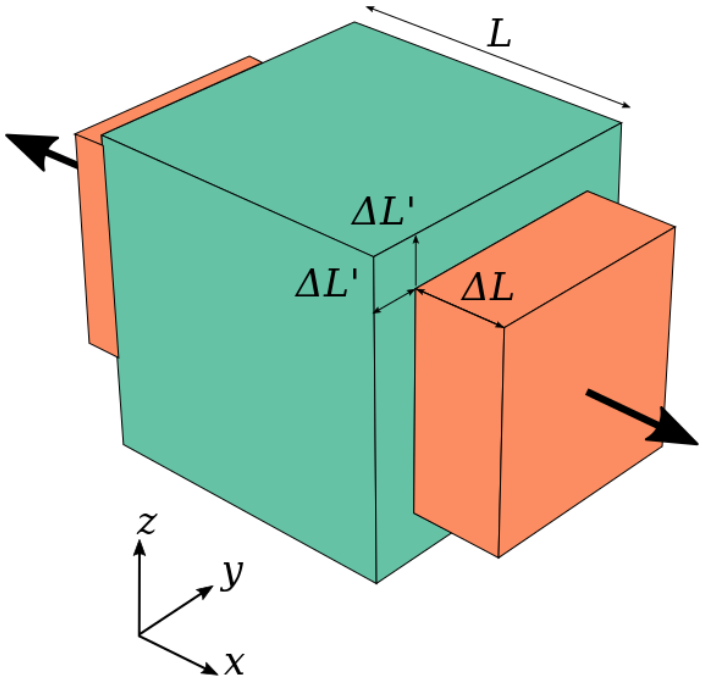

Figure 4.2: *Schematic view of different expansion directions in a cube with sides L (green). When force in the x-direction is exerted, the cube expands a distance ΔL along the x-axis (red), while contracting by $\Delta L'$ in the directions perpendicular to the x-direction.*[1]

While the Young's modulus does give a measure of strength in one dimension, it lacks a connection to other expansion or compression directions in a material. In general, when a

[1]Image source: `https://en.wikipedia.org/wiki/Poisson%27s_ratio`

material expands in a certain direction, for example the x-direction, it is likely to shrink in the directions perpendicular to that direction, the y- and z-direction, see Figure 4.2. The relation between these directions is given by the Poisson ratio

$$\nu = -\frac{d\epsilon_{trans}}{d\epsilon_{axial}} \tag{4.3}$$

in which $d\epsilon_{axial}$ and $d\epsilon_{trans}$ are the strain differences along the force axis and perpendicular to the force axis, respectively. The green cube with sides L in Figure 4.2 describes the unstrained situation, while the red cube represents the cube when subjected to a strain in the x-direction. Along this direction the cube expands by ΔL, while it contracts in the y- and z-direction by $\Delta L'$. In the case of small deformations, the Poisson ratio can be approximated by simply giving the ratio between the expanded and contracted material

$$\nu \approx -\frac{\Delta L'}{\Delta L} \tag{4.4}$$

For linear elastic, isotropic materials the Poisson ratio is bound by $-1 < \nu < 0.5$, where the boundaries can be derived based on theory of elasticity considering thermodynamically stable conditions [79, 80]. A positive Poisson ratio is common for most materials, since in general they tend to contract in the directions perpendicular to the direction of the expansion force, thus $\Delta L' < 0$ and $\nu > 0$. While a positive Poisson ratio can be intuitively understood, negative Poisson ratio's are less intuitive but also possible. These are so-called 'auxetic' materials, actually expanding in the directions perpendicular to the applied pressure direction. This characteristic can be observed in certain meta-materials and mechanically-engineered foam structures [81]. Materials that show a non-linear elastic stress-strain response or which are non-isotropic can posses values for the Poisson ratio outside of the thermodynamical limits of -1 and 0.5 [82]. Especially in the case of non-isotropic materials one has to be careful in describing the Young's modulus and Poisson ratio for specific strain directions.

4.3 Bulge testing

As touched upon in the introduction of this chapter, the Young's modulus and Poisson ratio of the multilayer graphene membranes are determined through bulge testing. For decades, bulge testing has been an almost standard experimental method to determine mechanical characteristics of membranes. The basic idea behind bulge testing is that when a pressure difference is set over a membrane, the membrane bulges away from the pressurized region. The deformation pattern of the membrane is characterized by the material properties, see Figure 4.3. This deformation depends on multiple parameters: membrane strength, width, thickness, etc. By choosing the proper membrane configuration and analysis method, the desired material characteristics such as the Young's modulus E and Poisson ratio ν can be extracted.

Bulge testing has already been used to determine the Young's modulus of single-layer graphene, showing values ranging from 30 to 500 GPa [76, 26]. While these values vary largely, possibly due to different preparation conditions, they both significantly differ from numerical studies which predict the value to be around $E \approx 1$ TPa (see Coa *et al.* (2014) [25] for a numerical study overview on the mechanical properties of single-layer graphene). Additionally, Zhang *et al.* (2012) [72] shows a decrease in stiffness for multilayer graphene, although again assumptions on multiple material parameters, amongst others the Poisson ratio, are used to determine the absolute value for the Young's modulus. In each experimental study so far, a specific geometrical configuration is used in combination with a theoretical value for the Poisson ratio. This value is always assumed to be constant around $\nu \approx 0.16$. This is due to the fact that the Young's modulus E and the Poisson ratio ν are both needed to describe the material stiffness

in a specific geometrical configuration. A single stress-strain curve as shown in Figure 4.1 only gives information on the elastic modulus in that specific configuration. At least two bulging configurations are needed to obtain information on both the Young's modulus and the Poisson ratio independently, as is described in more detail in section 4.3.2 [83, 84].

4.3.1 Membrane profile analysis

In this thesis two different membrane configurations are applied to determine the mechanical characteristics of the multilayer graphene: a rectangular and square shape. Ideally a round membrane shape is chosen, but due to processing limitations the square membranes are spherically approximated. In this section round membranes are used to illustrate the bulge test principle. From both configurations the stress-strain curves are extracted to determine their mechanical response.

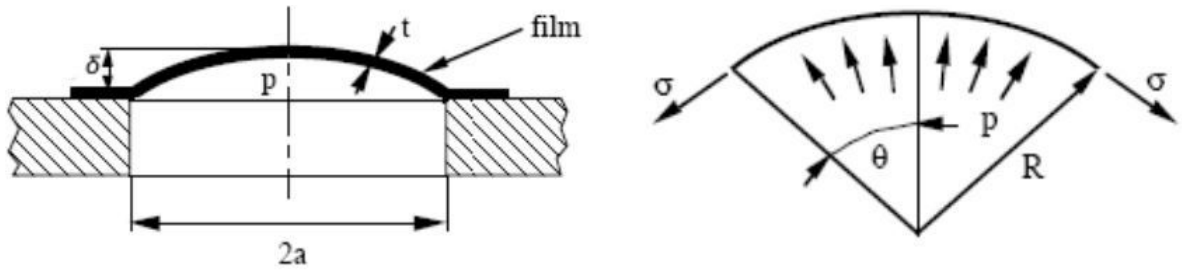

Figure 4.3: *Schematic description of the membrane parameters used to determine the stress and strain applied to the membrane.*[2]

The pressure difference P over the membrane causes the membrane to bulge upward, as seen in Figure 4.3. The deflection curvature can be used to determine the stress and strain applied to the membrane. For a membrane of width $2a$, thickness t and deflection δ, the strain ϵ is given by

$$\epsilon = \frac{a^2+\delta^2}{2a\delta}\sin^{-1}\left(\frac{2a\delta}{a^2+d^2}\right) - 1 = \frac{R}{a}\sin^{-1}\left(\frac{a}{R}\right) - 1 \tag{4.5}$$

with $R = (a^2+\delta^2)/(2\delta)$ the radius of curvature of the pressurized membrane [84]. This strain equation is valid for both rectangular and round membranes. Similarly, the stress applied to the membrane can be determined by

$$\sigma = \frac{P(a^2+\delta^2)}{2\delta t} = \frac{PR}{t} \tag{4.6}$$

and

$$\sigma = \frac{P(a^2+\delta^2)}{4\delta t} = \frac{PR}{2t} \tag{4.7}$$

for a rectangular and round membrane, respectively [84, 85]. As seen in the equations above, the strain and stress can be determined either measuring the deflection δ or the radius of curvature R. In this thesis it is chosen to fit the full membrane profile to extract the radius of curvature R. By choosing this method it is not necessary to determine initial deflections and possible sample tilt is corrected for.

[2]Image source: MSc thesis S.Shafqat (2014) [84]

Rectangular membrane: cylindrical fit

Rectangular membranes with aspect ratios > 4 have been shown to follow deflection patterns virtually independent from the elongated direction, experiencing only strain in one direction, a so-called planar strain [86]. Rectangular membranes can therefore be approximated by an infinitely long cylindrical shape when pressurized, see Figure 4.4. The radius of curvature R is extracted by fitting a three dimensional cylinder trough the point-cloud data $z(x, y)$

$$z(x, y) = b + e \cdot y + \sqrt{R^2 - (x - a - d \cdot y)^2} \tag{4.8}$$

The cylindrical formula is derived from the general equation for a cylinder in the y-direction $x^2 + z^2 = R^2$ including offsets in the z- and x direction, b and a, respectively. Although the samples are leveled in the $x - y$ plane during initialization, offsets are unavoidable and corrected for by including the terms $e \cdot y$ and $d \cdot y$ in the model. It is indeed found these terms are relatively small $(d, e \ll 1)$ indicating the sample orientation is close to horizontal.

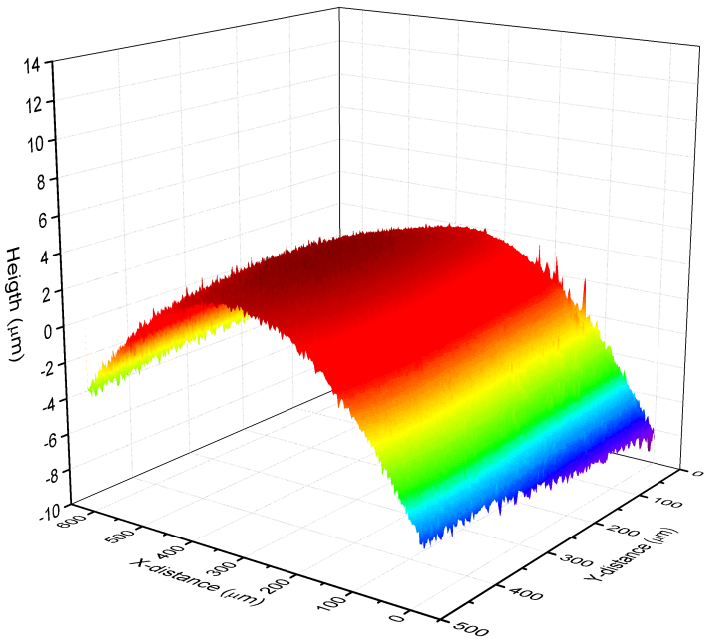

Figure 4.4: *Height profile of a pressurized 5x1 mm^2 rectangular multilayer graphene membrane ($t = 2.76$ nm, $P = 6$ mbar) taking a cylindrical shape.*

Square membrane: spherical approximation

The second configuration required for the bulge test procedure is a round geometry. Round membranes take a spherical shape when pressurized, experiencing a strain in two directions, so-called biaxial strain. Unfortunately, due to processing limitations, only square configurations can be created which have to be spherically approximated. As long as the spherical fit stays away from the edges, the spherical approximation is justified. Unfortunately, full 3D-fits of the membrane profile show too large deviations. Therefore a semi-3D cross section model is used, which is shortly discussed here. A more detailed comparison of the different spherical approximation methods of the square membrane is given in Appendix B.

Figure 4.5a shows the height profile of a pressurized square multilayer graphene membrane. The schematic illustration in Figure 4.5b shows an intuitive interpretation of the membrane regions in which the square membrane can be spherically approximated. In the dark blue

center area the membrane takes an approximate spherical form, while towards the light blue corners regions the membrane deflection clearly deviates from spherical behavior. The radius of curvature is determined by taking two cross sections of the height profile, along the x- and y-axis, which intersect at the maximum deflection point of the membrane. The cross sections in the x and y directions, z_x and z_y respectively, are simultaneously fitted with

$$\begin{cases} z_x(y) = c + \sqrt{R^2 - (y-a)^2} \\ z_y(x) = c + \sqrt{R^2 - (x-b)^2} \end{cases} \tag{4.9}$$

which share the z-offset c and radius of curvature R, but include different offsets a and b in the y- and x-direction, respectively.

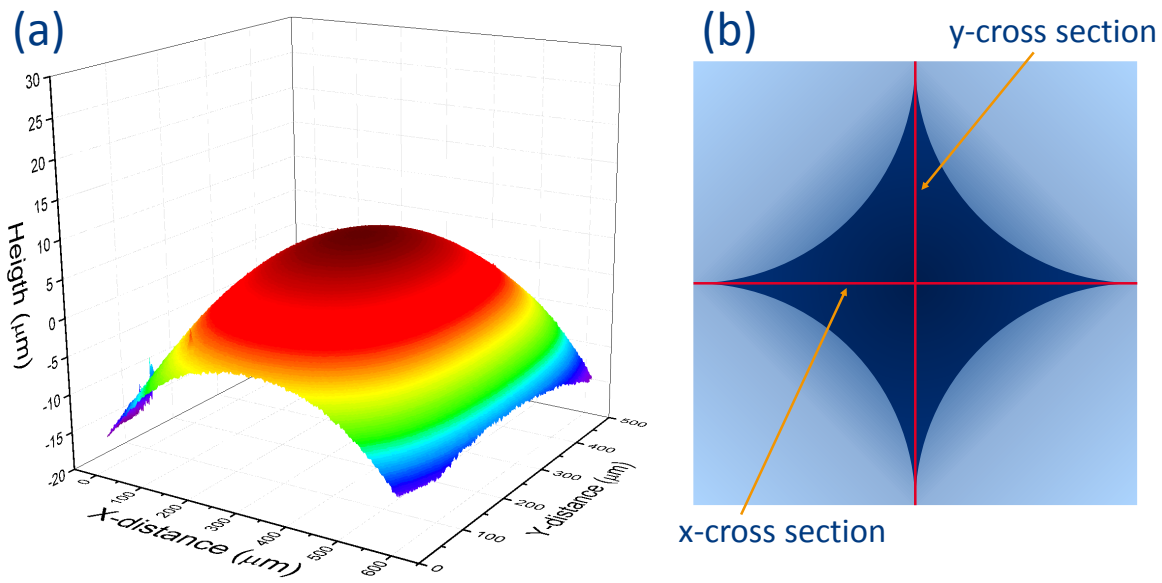

Figure 4.5: ***(a)*** *Height profile of a 1x1 mm^2 square multilayer graphene membrane when pressurized (t = 11.5 nm, P = 28 mbar).* ***(b)*** *Schematic top view of a pressurized square membrane. The typical area where the square membrane can be approximated by a sphere is shown in dark blue. Towards the corners the spherical approximation is no longer valid, indicated by the light blue areas. The two cross sections largely cover an area in which the spherical approximation is justified.*

4.3.2 Geometrical configurations

A rectangular membrane be approximated by a cylindrical shape when pressurized, see Figure 4.6a. In this configuration the membrane is only constrained in one direction, experiencing a **planar** strain E_p. This planar strain relates to the Young's modulus and Poisson ratio through

$$E_p = \frac{E}{1-\nu^2} \tag{4.10}$$

In case of a square configuration the membrane takes a spherical shape when pressurized, see Figure 4.6b. Since the membrane is fixed at its edges, it now experiences a constraint in two directions undergoing a **biaxial** strain modulus E_b. The biaxial strain is given by

$$E_b = \frac{E}{1-\nu} \tag{4.11}$$

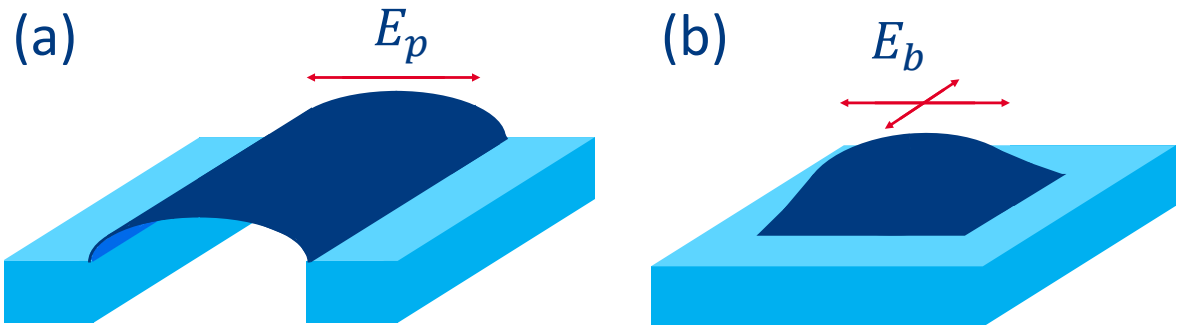

Figure 4.6: *Two membrane configurations required to independently determine the Young's modulus E and the Poisson ratio ν.* ***(a)*** *In a cylindrical configuration the membrane is only constrained in one direction undergoing planar strain E_p.* ***(b)*** *In a square configuration the membrane is constrained in two directions experiencing biaxial strain E_b.*

After characterizing the stress-strain curves of the two membrane configurations, the biaxial and planar strain modulus can be determined from the slope of their respective curves. Equations 4.11 and 4.10 can then be solved for E and ν:

$$E = 2E_b - \frac{E_b^2}{E_p} \tag{4.12}$$

and

$$\nu = \frac{E_b}{E_p} - 1 \tag{4.13}$$

This results in a method to calculate the Young's modulus and Poisson ratio separately, in stead of a generally composed elastic modulus like Equations 4.10 and 4.11 when adopting only a single geometrical configuration. In the next section this method is applied to determine the Young's modulus and Poisson ratio of the multilayer graphene membranes created in this thesis.

4.4 Bulge test results

The bulge tests are performed using the setup described in section 2.5 and analyzed according to the procedure described above. The thickness of the multilayer graphene is determined through UV-vis spectroscopy as described in Chapter 3.

Similar to the UV-vis chapter, two different thickness of graphene membranes are used for bulge testing: type 1 graphene with a thickness of $t = 11.5$ nm and type 2 graphene which is 2.76 nm thick. First, the bulge results of the thickest $t = 11.5$ nm membrane are discussed and the non-linear response is described. Second, the non-linear effect in the stress-strain response is quantitatively analyzed using a recent literature model on the bulging of single-layer graphene. Lastly, bulge test results on the thinner 2.76 nm graphene membrane are discussed and compared to literature values on the stiffness of single- and multilayer graphene.

4.4.1 Young's modulus & Poisson ratio determination

Figure 4.7 shows the stress-strain curves of multilayer graphene membranes with thickness $t = 11.5$, in both the square and rectangular configurations. All membranes are pressurized until membrane rupture, capturing the largest possible part of the stress-strain curve. In both the square and rectangular membrane configurations, there is no well-defined stress limit the

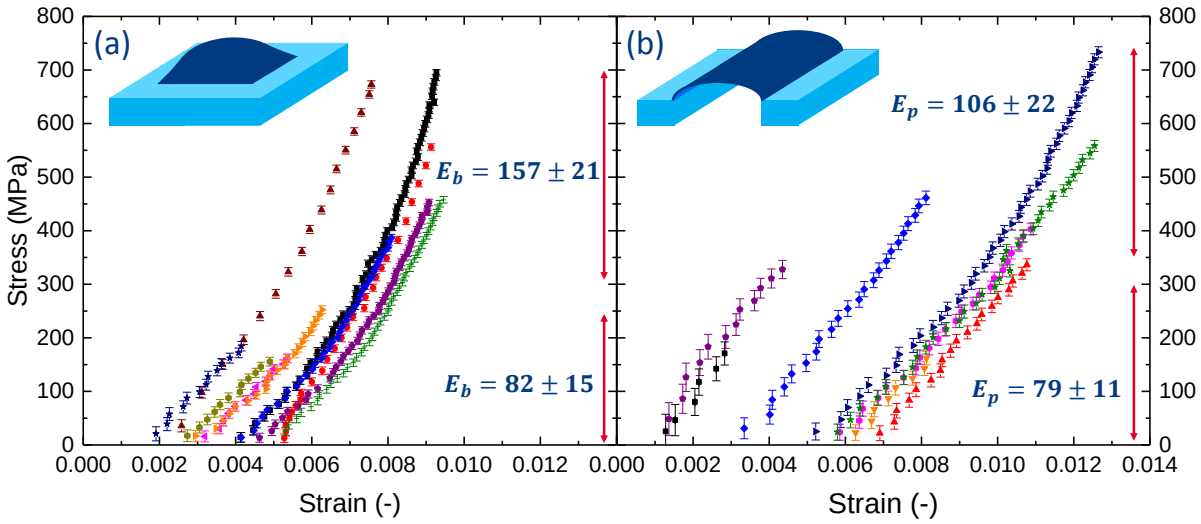

Figure 4.7: *Stress-strain curves of multilayer graphene ($t = 11.5$ nm) in* ***(a)*** *a square configuration and* ***(b)*** *a rectangular configuration, with each color indicating a bulge test on a different sample. The biaxial E_b and planar E_b modulus are linearly approximated for low stress up to ∼250-300 MPa and high stress from ∼300-350 MPa.*

membranes withstand, although individual samples have been observed enduring stress levels of $700 - 750$ MPa ($P_{max} = 73$ and 46 mbar for the square and rectangular membrane, respectively). It is interesting to observe the large onset of the curves. This can be attributed due to the large scale wrinkling, see Figure 4.8. When even slightly pressurized, wrinkles will be suppressed by smoothening of the membrane through off-center deflection, resulting in a strongly curved membrane R_1. The difference in onsets, which is most prominently visible in the rectangular membranes, can be attributed attachment of the membrane to the edges. The resulting curvature is less strong, leading to a larger radius $R_2 > R_1$ and thus $\epsilon_2 < \epsilon_1$.

All the stress-strain curves in Figure 4.7 follow a similar trend, showing a non-linear response with increasing stress and having similar steepnesses. Hysteresis test have been performed to verify the non-linear response, see Appendix C. Both in loading and unloading cycles the non-linear behavior is observed, confirming it is an intrinsic material characteristic and cannot be attributed to for example material failure at high stress. As described earlier in this chapter, materials that describe such a non-linear stress-strain response are called hyperelastic materials. While the curves in Figure 4.7 suggest hyperelastic behavior, they only provide direct information on the biaxial E_b and planar E_p modulus. To extract information on the Young's modulus E and the Poisson ratio ν, the square and rectangular responses are linearly approximated in order to make a first approximation of E_b and E_p. The stress-strain curves

Table 4.1: *Extracted biaxial and planar modulus from Figure 4.7. Between brackets the number of samples used to determine the elastic modulus is given. The resulting Young's modulus and Poisson ratio of the two stress regimes are calculated using Equations 4.12 and 4.13.*

	Low stress (< 250-300 MPa)	**High stress (> 300-350 MPa)**
Biaxial modulus E_b (GPa)	82 ± 15 ($N = 10$)	157 ± 21 ($N = 6$)
Planar modulus E_p (GPa)	79 ± 11 ($N = 8$)	106 ± 22 ($N = 4$)
Young's modulus E (GPa)	79 ± 12	82 ± 51
Poisson ratio ν (-)	0.0 ± 0.4	0.5 ± 0.4

suggest two regimes of operation: below and above ∼250-300 MPa. In the lower stress regime, both configurations have similar responses: $E_b = 82 \pm 15$ GPa and $E_p = 79 \pm 11$ GPa, while these values increase to $E_b = 157 \pm 21$ and $E_p = 106 \pm 22$ in the high-stress regime, see Table 4.1.

Surprisingly, while the individual configurations show an increase in elastic modulus E_b and E_p, the Young's modulus E does not show this trend and stays relatively constant at $E = 79 \pm 12$ GPa in the low stress regime and $E = 82 \pm 51$ GPa under high stresses. A literature discussion on how this stiffness compares to other literature values will be given in section 4.4.3. As E remains constant, the Poisson ratio ν increases from $\nu = 0.0 \pm 0.2$ to $\nu = 0.5 \pm 0.4$, close to the isotropic limit. A near-zero value for the Poisson ratio indicates neglectable directionally in multilayer graphene membranes, clearly different from literature assumptions on single-layer graphene. A more pronounced directional effect can be seen at high stress, where the Poisson ratio increases to $\nu = 0.5 \pm 0.4$. This value is larger than the generally assumed, and numerically calculated, value of $\nu = 0.16$ [25, 87]. Although the high value of $\nu = 0.5$ can be compared to some individual simulation results which predict values around $\nu = 0.40 - 0.45$ [88, 89, 90, 91], the Young's modulus in these specific simulations sometimes reaches up to $E = 1 - 4$ TPa, questioning the validity of the corresponding Poisson ratio.

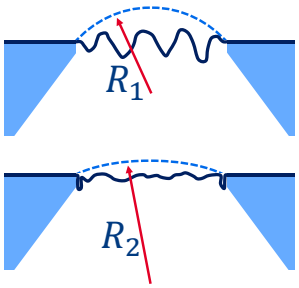

Figure 4.8: *Schematic description of the difference in strain onset. Since in the bottom configuration the membrane is attached to the sides, $R_1 < R_2$ after the initial pressurization.*

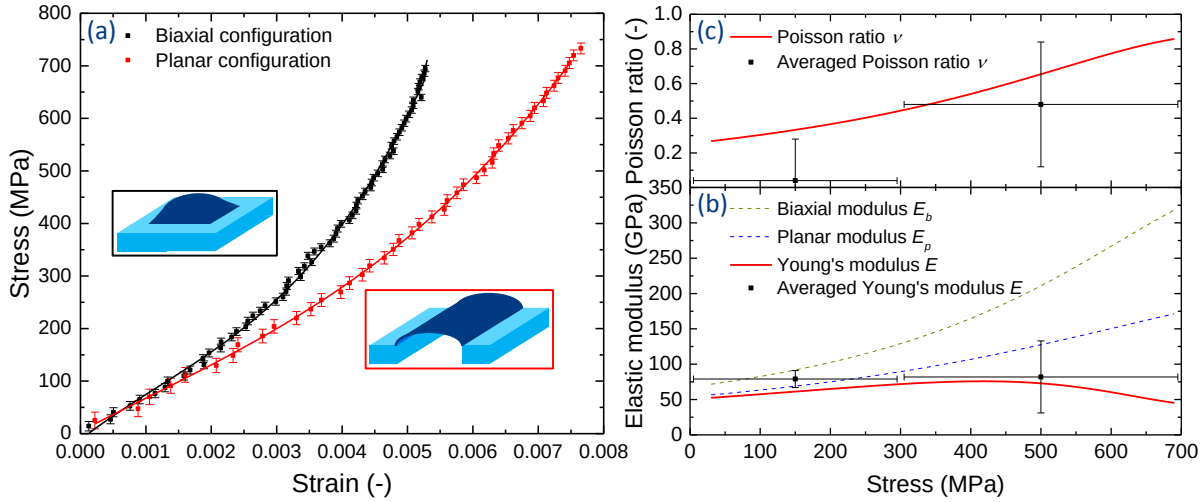

Figure 4.9: ***(a)*** *Typical biaxial and planar stress-stain curves of the multilayer graphene membranes.* ***(b)*** *Biaxial and planar moduli are calculated from the corresponding stress-strain curves. The resulting Young's modulus and Poisson ratio* ***(c)*** *are plotted over the full stress range. For comparison the statistically determined values for the Young's modulus and Poisson ratio in both the low stress and high stress regime are indicated.*

Figure 4.9a shows a more detailed comparison of the biaxial and planar response of two typical stress-strain curves. The two curves are fitted with a smoothed cubic b-spline, being able to extract the slope and thus the biaxial E_b and planar modulus E_p as function of the applied stress, see Figure 4.9b. Since now a continuous distribution for E_b and E_p is given, the Young's modulus E and Poisson ratio ν can also be calculated as function of the applied stress. This extends the linear approximation described above into a more detailed description.

The continuous upward trend of E_b and E_p confirms the observed stiffening derived in Table 4.1. The resulting Young's modulus shows a slight fluctuation in stiffness, but stays relatively constant. This corresponds with the values of $E = 79 \pm 12$ GPa and $E = 82 \pm 51$ GPa for the low and high stress regime, respectively, indicated with the two points in Figure 4.9b. The continuous distribution of the Poisson ratio in Figure 4.9c also supports the observed upward trend. The Poisson ratio at low stress deviates slightly compared to the statistically determined value. This can be caused by the fact the response of the chosen sample is slightly different compared to the statistically determined value over multiple samples. At high stress the Poisson ratio actually surpasses the theoretical limit for isotropic materials of 0.5. This can be explained by the consideration that graphene does not fit the aspects of an isotropical crystal configuration, but can rather be described by an orthotropic configuration [92]. Orthotropic materials have properties which are equal in one plane, for example $x - y$, but can be different in the directions perpendicular to that plane, z-direction. (Multilayer) graphene meets these requirements due to its in-plane hexagonal symmetric structure. For orthotropic materials the Poisson ratio is restricted by

$$-1 < \nu < 1 \tag{4.14}$$

imposing an upper boundary of +1 instead of the previously reported 0.5 for isotropic materials. This corresponds with the observation in Figure 4.9c where the Poisson ratio increases to well above 0.5. While this explains the high values of the Poisson ratio, the value of $\nu \approx 0$, indicating low directionality dependence, can be understood when examining SEM-images of the multilayer membranes, see Figure 4.10. The graphene shows significant small-scale crumpling. When stress is applied it first flattens out the membrane's roughness, not specifically being constrained by any boundary conditions in other directions, thus $\nu \approx 0$. When the wrinkles are flattened out, constraints in other directions become more important, leading to a more noticable value for the Poisson ratio $\nu > 0$. This crumpling effect is further quantitatively analyzed in the following section.

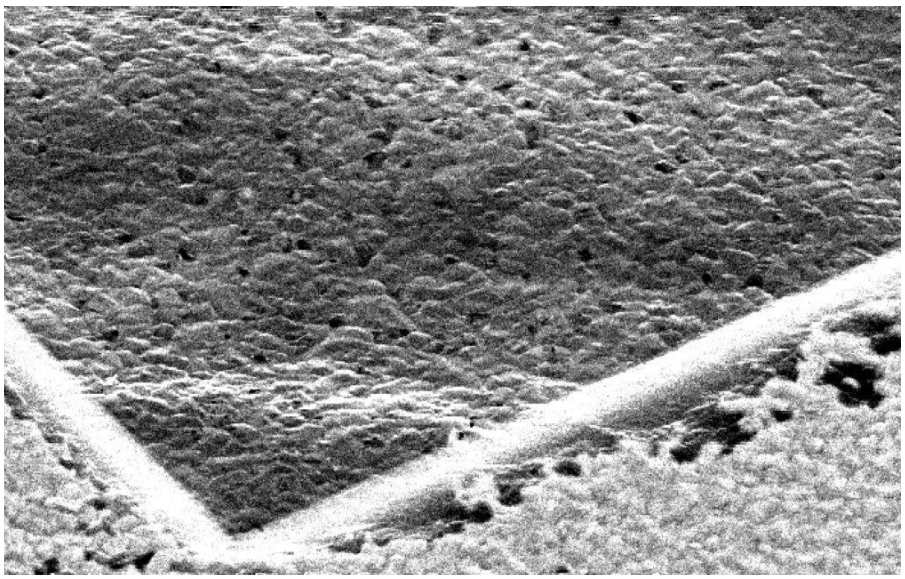

Figure 4.10: *SEM-image of a $t = 11.5$ nm multilayer graphene membrane under a 45° angle. At this angle the small-scale crumpling is clearly visualized.*

4.4.2 Membrane crumpling and non-linear bulging

The pronounced non-linear effect in bulging of graphene membranes has already been encountered in measurements from Nicholl *et al.* (2015) [26] and Berger *et al.* (2016) [76]. Nicholl observes this non-linear response by an increase of 400% in biaxial modulus and qualitatively describe its possible origin: static wrinkling and crumpling of the graphene membrane. Indeed, as shown in the previous section, SEM-images of graphene membranes show small-scale roughness and large-scale wrinkling of the multilayer membranes. This undulation has a softening effect on the stiffness of the membrane, which can intuitively be understood by comparing the crumpled graphene to a corrugated board. Pulling the ends of an undulated board, the wrinkles of the board are smoothened out. When the pressure is increased further, the intrinsic strength of the board starts to dominate over the waviness of the material, leading to an increase in stiffness. A different softening effect can contribute to the non-linear response: flexural phonons, lattice vibrations in 2D material [93]. This effect is dismissed by Nicholl, since it is observed the temperature dependence of the elastic modulus is relatively small in single-layer graphene. In this work, it is expected that the contribution of flexural phonons is negligible, since the increasing number of atomic layers suppresses the out-of-plane vibrations [94].

A quantitative model of the non-linear response of graphene has been developed by Gornyi *et al.* (2016) [95], and applied in a follow-up paper by Nicholl *et al.* (2017) [96]. The response of the strain ϵ as function of stress σ is given according to

$$\epsilon(\sigma) = \frac{\sigma_*}{k}\Big(\frac{\sigma}{\sigma_*} + \frac{1}{\alpha}\Big(\frac{\sigma}{\sigma_*}\Big)^{\alpha}\Big) \tag{4.15}$$

with k the elastic modulus of the specific configuration (for example E_b or E_p), σ_* the crossover stress and α a coefficient which is determined by amount of disorder in the graphene. This exponent is predicted to be $\alpha \approx 0.1$ for strongly disordered graphene, governed by static wrinkling, and $\alpha \approx 0.5$ for clean graphene, with its main contribution from flexural phonons. Equation 4.15 implicates at low stress ($\sigma < \sigma_*$) the strain is a non-linear function $\epsilon \sim \sigma^{\alpha}$. At sufficiently high stress ($\sigma > \sigma_*$) the conventional linear behavior $\epsilon \sim \sigma$ is reached.

In contrast to Nicholl *et al.* (2017) [96], all three parameters $k = E_b$, α and σ_* are determined by fitting, where Nicholl fixes E_b as the value determined from profilometry in the high-stress regime. Futhermore, the initial strain-offset due to the large-scale wrinkling of the membrane is incorporated into the non-linear response, thus neglecting any stress- or strain-offset while fitting. Equation 4.15 is fitted to the stress-strain curves showing the most pronounced non-linear effects, see Figure 4.11.

The average non-linear exponent found by fitting is $\alpha = 0.17 \pm 0.05$, in correspondence to the value of 0.12 found by Nicholl [96] for single-layer graphene and close to the value of $\alpha = 0.1$ expected for static wrinkling [95]. In agreement with literature, it supports the assumption flexural phonons are suppressed in multi-layer graphene and the non-linear response is governed by static wrinkling. The average value of $E_b = 256 \pm 87$ GPa for the linear response regime is higher than the value found in section section 4.4.1 in the high stress regime $E_b = 157$ GPa, but is close to the maximum value for E_b observed in Figure 4.9b. This suggest the membranes break before fully reaching the linear regime where $\epsilon \sim \sigma$, indicating wrinkling might still be present at the high stresses applied in this thesis. Lastly, the average cross-over stress of $\sigma_* = 282 \pm 187$ MPa shows a broad cross-over regime, possibly supporting the assumption of wrinkling still being present. Despite a large uncertainty, this value is close to the value of $\sigma = 250 - 300$ MPa used to separate a low and high stress regime for linear approximation.

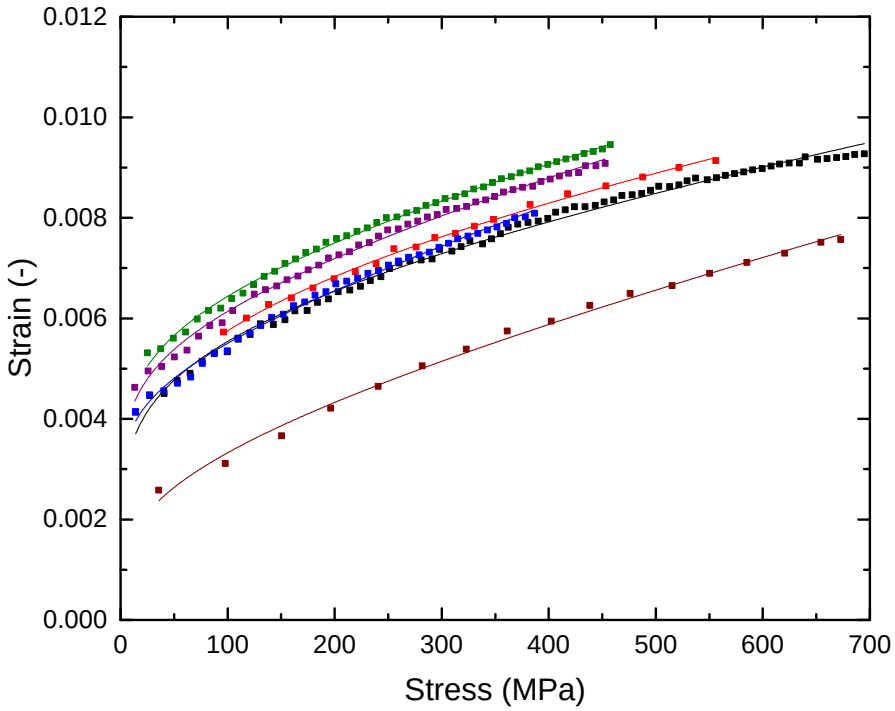

Figure 4.11: *Non-linear strain-stress curves of the square membranes including the fits according to Equation 4.15. The individual fit parameters are given in Appendix E.*

While Equation 4.15 does give a quantitative description of the **effective** elastic modulus in a specific configuration, for example the biaxial strain modulus E_b, it does not necessarily relate to the **intrinsic** value for the Young's modulus E. In the previous section it has been shown the Young's modulus is relatively constant and the Poisson ratio varies largely with increasing stress. Following Equations 4.11 and 4.10, $E_b, E_p \sim \nu, E$, it suggests the Poisson ratio actually is the largest contributor to the non-linear response of the graphene membranes. While current research has mainly focused on the effect of crumpling on the effective stiffness of graphene, it would be interesting to investigate the effect of crumpling on the Poisson ratio. Besides the non-linear Poisson ratio, it is of interest to investigate the change in stiffness with membrane thickness, which is discussed in the next section.

4.4.3 Layer dependent membrane stiffening

In order to investigate the effect of the thickness on the stiffness of the graphene, a thinner graphene is grown for comparison. The graphene in question is determined to be 2.76 nm thick, approximately 8 layers, and subjected to similar bulge tests as the first type of graphene, $t = 11.5$ nm. Figure 4.12 shows the stress-strain curves of square and rectangular shaped membranes. A similar non-linear response up to ~900 MPa can be observed, specifically in the biaxial configuration. Since the membrane are much thinner, and the stress is inversely proportional with the thickness $\sigma \sim 1/t$, the data points are spaced further apart and the corresponding error is larger.

Unfortunately, a full non-linear description like performed in the previous section is not possible due to the large data spacing, but similar to the previous type of graphene, the biaxial E_b and planar modulus E_p are linearly approximated in two stress regimes: below and above $\sim$ 600 MPa. The number of data points in the rectangular configuration is very limited, choosing to

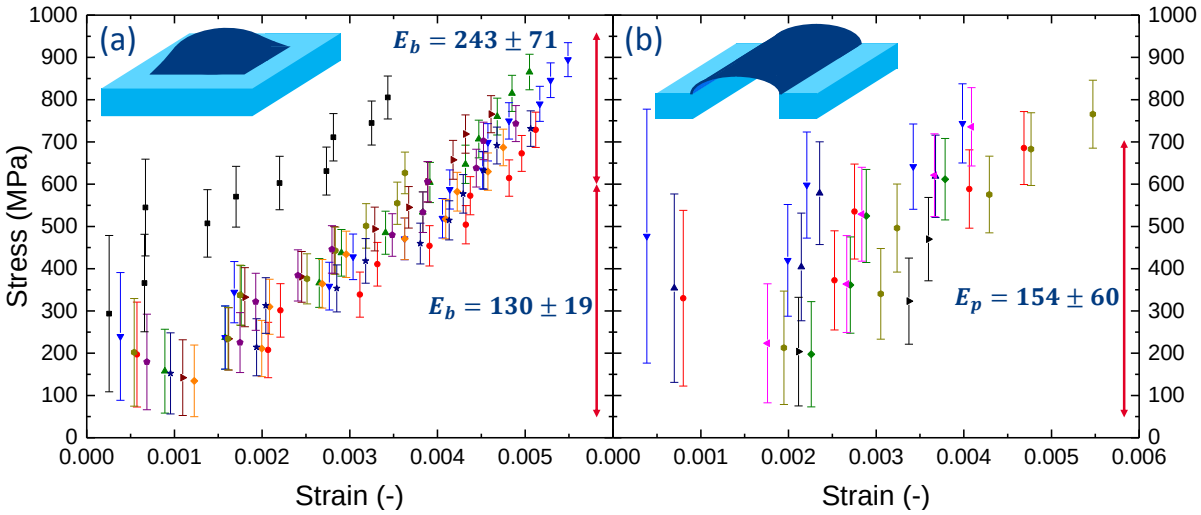

Figure 4.12: *Stress strain curves of multilayer graphene (t = 2.76 nm) in* ***(a)*** *a square configuration and* ***(b)*** *a rectangular configuration, with each color indicating a bulge test on a different sample. The biaxial E_b and planar E_b modulus are linearly approximated for low stresses up to ∼600 MPa and high stresses from ∼600 MPa.*

appoint the curve up to 700 MPa as the planar modulus E_p for the lower regime. Directly comparing the biaxial and planar moduli of the two different thickness, see Table 4.2, it can be seen the 2.76 nm membrane response is significantly stiffer in both configurations. The biaxial moduli E_b are almost a factor two higher, 130 ± 19 GPa and 243 ± 71 GPa for the low and high stress regime, respectively, compared to 82 GPa and 157 GPa for the $t = 11.5$ nm graphene. Similarly, the planar modulus increases from 79 GPa to 154 ± 60 GPa, showing the same increase in stiffness.

Table 4.2: *Extracted biaxial and planar modulus from Figure 4.12. The Young's modulus and Poisson ratio of the two stress regimes are calculated using Equations 4.12 and 4.13. No planar modulus for the high stress regime is extracted due to low number of datapoints.*

	Low stress (< 600 MPa)	**High stress (> 600 MPa)**
Biaxial modulus E_b (GPa)	130 ± 19 ($N = 9$)	243 ± 71 ($N = 7$)
Planar modulus E_p (GPa)	154 ± 60 ($N = 7$)	– ($N = 0$)
Young's modulus E (GPa)	150 ± 44	–
Poisson ratio ν (-)	-0.2 ± 0.4	–

The Poisson ratio found in the lower stress regime is close to zero and even slightly negative, $\nu = -0.2 \pm 0.4$, similar to measured in the case of the $t = 11.5$ nm graphene. Some simulations even suggest the possibility of a non-linear Poisson ratio in single-layer graphene approaching negative values towards high strains [97, 98]. It has to be noted these simulations ignore the effect of crumpling, which, as shown in the previous section, can be of great influence on the mechanical response. While the extracted Young's modulus of 150 ± 44 GPa is higher than the value of ∼ 80 GPa for the $t = 11.5$ nm membrane, see Table 4.2, both are still significantly lower than the theoretical value of $E \approx 1$ TPa for single-layer graphene [25]. Zhang *et al.* (2012) [72] measure a decrease in Young's modulus from 891 GPa to 393 GPa, 51 GPa and 27 GPa for mono-, bi-, tri- and tetralayer graphene, respectively. Interestingly, the multilayer graphene in this thesis shows higher stiffnesses. The Young's moduli of 80 and 150 GPa for 34 and 8 layers, respectively, are both significantly larger than the stiffness of trilayer graphene

as measured by Zhang. Main reason for this discrepancy can be attributed to the measuring method applied by Zhang, having to correct for substrate effects and assumptions on materials parameters, resulting in Young's moduli of which the correctness can be questioned, specifically in the case of multilayer graphene. It might be more applicable to compare the Young's moduli of 80 and 150 GPa measured in this thesis to more graphite-like materials, since the material at hand is multilayer graphene. Literature values on the Young's modulus for HOPG ($15-30$ GPa [99]), amorphous carbon ($4.1-27.6$ GPa [100]) and graphite-like carbon films (~ 180 GPa [101]) might be more representative for the multilayer membranes. These values indeed indicate lower Young's moduli than the values found for single-layer graphene. In combination with the experimentally determined values for E found in this work, this indicates **multilayer** graphene membranes are less stiff compared to their **single-layer** counterparts.

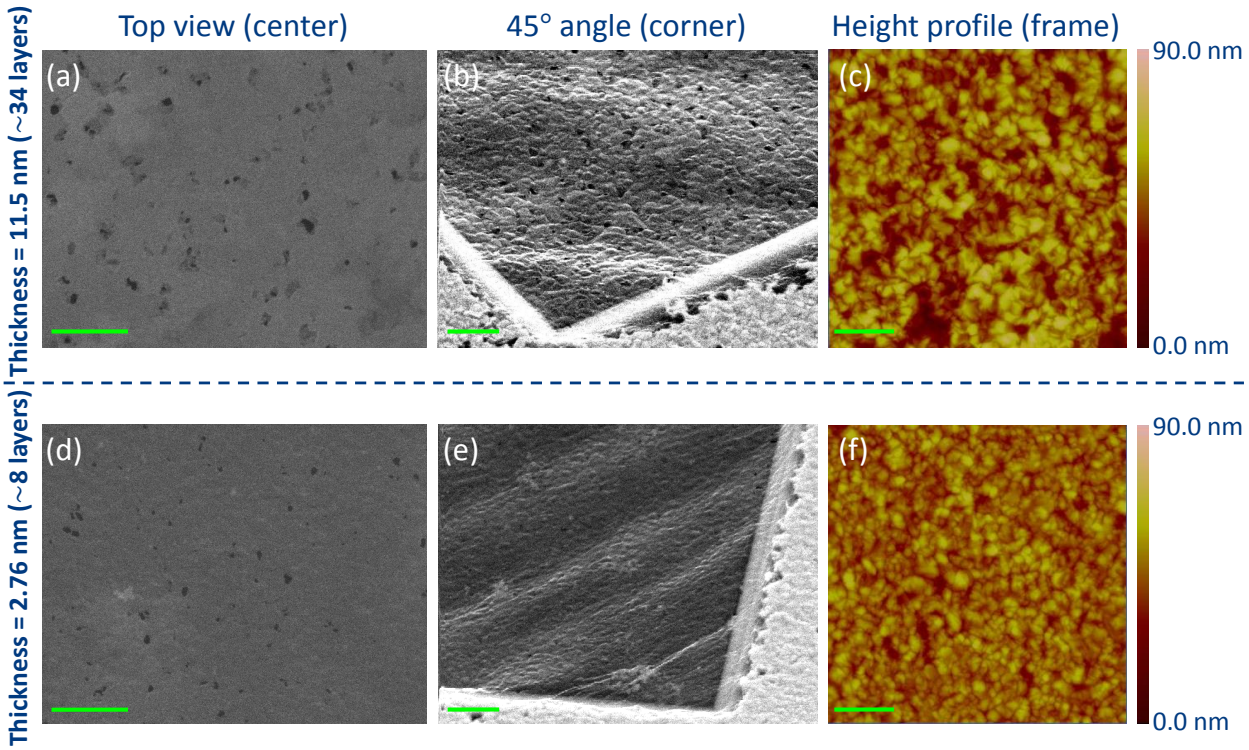

Figure 4.13: *SEM- and AFM images of freestanding graphene membranes with thickness $t = 11.5$ nm (top row) and $t = 2.76$ nm (bottom row).* ***(a),(d)*** *SEM-images top view taken around the center of the membrane, visualizing the small holes (dark spots) in the membrane.* ***(b),(e)*** *SEM-images taken under a $\sim 45°$ angle, showing the large-scale wrinkling and small-scale crumpling.* ***(c),(f)*** *AFM height profiles visualizing the surface roughness on the frame of the membrane. The green bar indicates a distance of 1 μm.*

A critical note has to be placed on the interpretation of the Young's modulus towards possible applications. While this thesis shows the **stiffness** of multilayer graphene membranes increases when the number of layers decreases, this does not give a direct measure for the membrane's **strength**. As intuitively expected, the thinner membranes are weaker and can only withstand a maximum pressure of $P_{max} = 15$ and 7 mbar for the square and rectangular configuration, respectively, where the $t = 11.5$ nm membranes can be pressurized until $P_{max} = 73$ and 46 mbar. The corresponding maximum stress, on the other hand, is slightly higher for the thinner membranes, ~ 900 MPa compared to ~ 700 MPa for the thicker membranes. The 2.76 nm membranes also are more consistent in reaching the same maximum pressure.

The eventual rupture of the graphene membranes can be the result of different factors, such as holes in the membranes, localized stress nodes or substrate edge effects. SEM-images indeed suggest the thinner membranes retain a lower hole density, see Figure 4.13, indicating this failure mechanism is less likely to be responsible for the membrane rupture than in the thicker membranes. A similar difference can be noted comparing the AFM height profiles of the graphene on top of the metal catalyst along the edge of the frame. The $t = 11.5$ nm grown graphene shows larger surface roughness than the $t = 2.76$ nm graphene, measuring a root-mean-square average height deviation of $R_q = 10.8$ nm, compared to $R_q = 6.79$ nm for the thinner graphene. Assuming this surface roughness is imprinted into the graphene membranes when being etched free, see the 45° SEM-images in Figure 4.13, it also could lead to more nodes in the graphene membranes. These nodes could experience higher local stress build-up, thus being potential failure points.

4.5 Conclusion

In this chapter it has been shown that conventional bulge testing can be applied on large scale ($\sim$ mm^2), non-transfered freestanding multilayer graphene membranes. Two membrane configurations are applied, bypassing any *a priori* assumptions on Poisson ratio or multilayer thickness. Using this method the intrinsic value for the Young's modulus E and the Poisson ratio ν of multilayer graphene membranes are determined.

Multilayer graphene membranes of $t = 11.5$ nm have been shown to have a non-linear response to increasing stress in specific configurations. They do posses an intrinsic, relatively constant Young's modulus though, achieving a value of $E = 79 \pm 12$ GPa at low stresses and 82 ± 51 GPa towards higher stress levels. More interesting is the fact that the Poisson ratio increases from a near-zero value $\nu = 0.0 \pm 0.2$ at low stress, to a value of $\nu = 0.5 \pm 0.4$ at high stress. This value equals the isotropic limit of $\nu = 0.5$, but can be explained by accentuating that graphene is actually more resemblant to orthotropic materials, of which the Poisson ratio exhibits an upper boundary of $\nu = 1$. The non-linear behavior of the Poisson ratio is clearly different than the commonly used literature value of $\nu = 0.16$, almost always assumed to be constant.

Examining the biaxial non-linear response more closely, it can be quantitatively investigated according to a recently developed theory assessing the crumpling of graphene membranes. This literature model predicts $\epsilon \sim \sigma^{\alpha}$ in the non-linear regime of the strain-stress response, achieving a linear response $\epsilon \sim \sigma$ at high stress. According to theory, the observed value of $\alpha = 0.17 \pm 0.05$ suggests the graphene is dominated by static wrinkling, similar to recent literature observations. SEM-images indeed confirm the freestanding graphene is dominated by small-scale crumpling.

Comparing with a different graphene thickness $t = 2.76$ nm, the stiffness of the material increases from $E \approx 80$ GPa to $E = 150 \pm 44$ GPa. While the intrinsic response becomes increasingly stiff, it is still more resembling graphite materials ($E = 15 - 30$ GPa) than single-layer graphene ($E \approx 1$ TPa).

Ideally, the multilayer graphene membranes are pressurized until a full linear response is measured, verifying the biaxial modulus found in Equation 4.15 with linear approximation of the stress-strain curve. The maximum stress applied to the membranes could be increased by using circular membrane configurations, avoiding stress build-up towards the edges of the membrane. Besides the membrane shape, SEM- and AFM-images show the large surface roughness of the metal catalyst, likely creating nodes for pressure build-up and possible starting points for mem-

brane rupture. Improving membrane smoothness and creating more flat graphene membranes could strengthen the membranes. In addition, the multilayer graphene membranes exhibit multiple defects and holes, as identified in the SEM-images and Raman spectra. Improvements can be made in the growth process of the multilayer graphene.

From a more theoretical point of view, while current literature has mainly focused on modeling the crumpling effect in bulging of single-layer graphene, it would be interesting to investigate the effect of multiple layers on the presence of crumpling. This work has shown that the non-linear response of the stress-strain curves can be largely explained by a non-linear Poisson ratio. A possible explanation for this nonlinearity, besides crumpling, can be the orthotropic nature of (multilayer) graphene. The orthotropicity of graphene will need to be examined more closely, assessing its effect on the elasticity of graphene and other material parameters.

Chapter 5

Graphene incorporation in CMUT

This chapter investigates a potential application for graphene membranes in capacitive micromachined ultrasound transducers: CMUTs. In the introduction the working principle of CMUTs is explained and recent attempts to incorporate graphene in ultrasound applications are discussed. Next, attempts to electro-mechanically manipulate the multilayer graphene membranes fabricated in this work are described, showing proof-of-principle actuation similar to the working principle of CMUTs. Finally, graphene-CMUT devices are modeled to obtain device characteristics, such as the capacitance, collapse voltage and resonance frequency using typical multilayer graphene parameters.

5.1 Introduction

Ultrasound devices are well known for their ability to provide non-invasive detection and sensing techniques, especially in the field of medical applications [102]. A typical application of ultrasound can be found in imaging and therapy, such as echography [103], but other possibilities have been explored, for example in the field of biometrics as fingerprint sensors [104].

Figure 5.1 shows two typical devices used to generate ultrasound waves: a piezoelectric transducer and a capacitive micromachined ultrasonic transducer, in short CMUT. A piezoelectric transducer consists of a stack of materials which can be actuated by applying a voltage to the structure. Applying an AC-voltage, the piezoelectric material will expand and contract, inducing pressure waves in the surrounding medium. The process can also be reversed by first applying a pressure difference to the stack of materials. This induces a measurable voltage difference over the device. By using these two characteristics, a piezoelectric transducer can be used to either transmit or receive (ultra)sound waves.

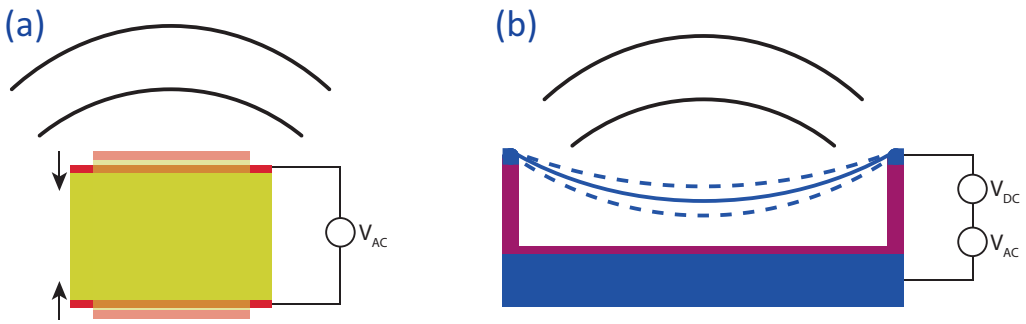

Figure 5.1: *Schematic representation of* ***(a)*** *a piezoelectric transducer, driven by an AC voltage source, and* ***(b)*** *a CMUT device, driven by both an AC and DC voltage source.*

Until 20 years ago piezoelectric transducers were the most common devices to create and detect ultrasound waves [105]. Although still widely used in various other types of applications, piezoelectric transducers had trouble keeping up with the increasingly demanding requirements for ultrasound applications. In particular the large impedance difference between the transducer and the surrounding medium, in general air, gave rise to below-average performance standards. Low efficiency and narrow bandwidth regions forced researchers to think differently on generating and sensing ultrasound. The solution was found in a different type of sound generating mechanism, provided by CMUTs [106]. As the name implies, a CMUT essentially consists of a capacitance, comparable to a parallel plate capacitance. Since the top electrode is suspended over a cavity, see Figure 5.1, imposing a DC voltage will create an electrostatic force, pulling the top electrode downward. Superimposing an AC-voltage will cause the top plate to vibrate, creating sound waves in the surrounding medium.

CMUTs have shown to posses broader bandwidth regions of operation than piezoelectric transducers, resulting in an improved axial resolution. This increased axial resolution leads to better quality imaging, e.g. blockages in blood vessels and echography [107]. In addition, using micromachining methods, CMUTs can be produced on a wafer scale, thereby reducing fabrication costs. CMUT devices are favorable in specific environments, especially due to their ability to operate under extreme conditions. CMUTs can be used in environments of high temperature (500 °C [108]) and under high pressure (up to 8 atmosphere [109]), while also being suitable for underwater imaging [110]. Outside of creating and sensing ultrasound waves, CMUT devices can also be modified to act as wind speed gauges [111], CO_2 detectors [112] and immunosensors detectors [113], showing their large potential for other types of applications.

5.2 CMUT design and processing

Although the operation of CMUTs is based on a relatively simple principle, the output properties are influenced by numerous factors. Parameters such as the CMUT design (cavity height, width, etc.) and material properties (membrane stiffness, pre-stress, etc.) all determine the response of the CMUT. The operating frequency determines whether a CMUT is more suitable for for example medical imaging or diagnostic purposes, see Figure 5.2. Other operating characteristics such as the collapse voltage and capacitance of the CMUT are all influenced by the design parameters. It is crucial to choose the right design, processing techniques and materials resulting in a CMUT device with the desired specifications. This section discusses the conventional design of CMUTs and typically used materials, as well as a short mention of recent attempts to incorporate graphene in ultrasound devices.

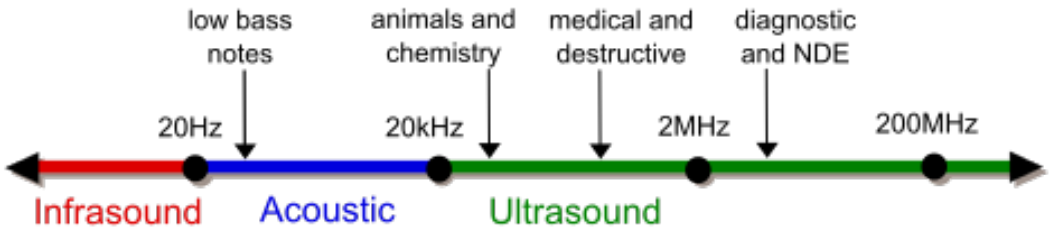

Figure 5.2: *Frequency ranges for sound waves determining the type of application. Ultrasound is generally considered as frequencies of 20 kHz and upwards.*[1]

[1]Image source: `https://en.wikipedia.org/wiki/Ultrasound`

5.2.1 Conventional CMUT designs

A typical CMUT design is illustrated in Figure 5.3a. As is standard practice in semiconductor processing, fabrication steps are performed on a silicon wafer, potentially acting as the bottom electrode of the capacitance structure. An insulating material, in this case silicon nitride (SiN) is deposited, after which the top part of the capacitor structure, for example aluminum (Al), is deposited. To seal the structure, another insulating material, in this case low-temperature silicon dioxide (SiO_2), is deposited over the structure to complete the membrane and isolate the top electrode from its surroundings. Using different lithography and etching techniques a cavity is created in the SiN, leaving a membrane suspended over a thin gap and completing the capacitance structure. For more details on the exact fabrication of CMUT devices, see the paper of Ergun *et al.* (2004) on CMUT processing [114].

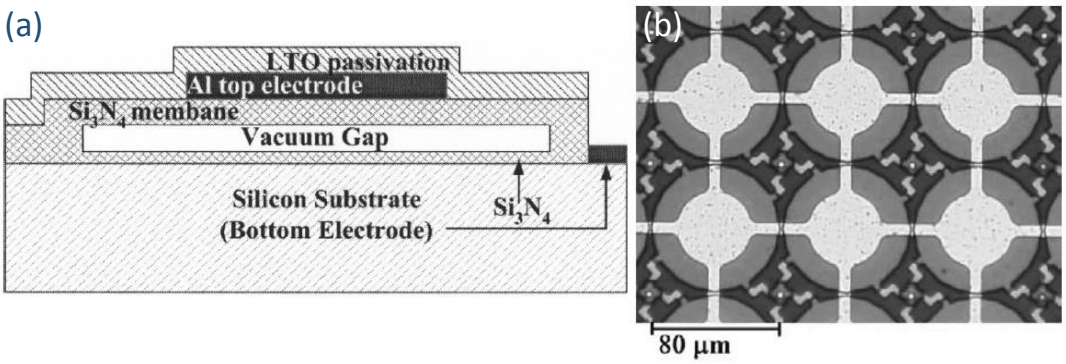

Figure 5.3: ***(a)*** *Design layout of a CMUT device. The different components of the CMUT are indicated, with the two electrodes highlighted in dark grey.* ***(b)*** *Top view of a CMUT array showing the electrodes being interconnected. This enables simultaneous actuation of multiple CMUTs.*[2]

Figure 5.3b shows a top view of a CMUT array. It can be seen that the top electrodes on each individual CMUT are interconnected, indicating the individual membranes can be actuated simultaneously [115]. Actuating an array of CMUTs in stead of only a single CMUT gives the advantage of being able to create 2D images. This is of great advantage in tissue imaging, being able to focus the ultrasound in specific directions only probing areas of interest [116].

5.2.2 Graphene incorporation in resonators and CMUTs

In CMUTs the membrane in general consists of multiple materials, with the conducting electrode packed in-between two insulating layers. By combining the ability to conduct electricity on one side, with extreme flexibility on the other, graphene is a prime candidate for incorporation in CMUT devices. Especially the ability to tune the frequency of graphene, in stead of a general fixed resonance frequency for macroscopic materials, is a promising feature [117].

The idea of incorporating single-layer graphene in CMUT-structures has already been studied in different forms. An example of graphene incorporation is shown by Tian *et al.* (2012) [118], describing transfered graphene on top of patterned anodic aluminum oxide resonating from 20 kHz to 50 kHz. Lebental *et al.* (2011) [119] show a different design in which carbon nanotubes are suspended over a trench, resulting in a resonance frequency of 10 MHz in air, within the application range for diagnostic imaging.

[2]Image sources: Ergun *et al.* (2004) [114] and Ergun *et al.* (2005) [115]

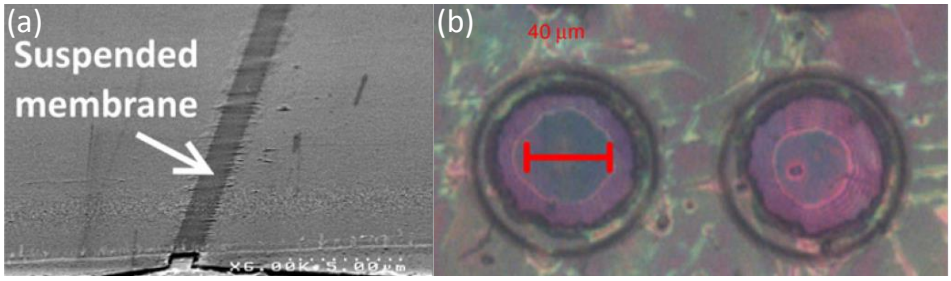

Figure 5.4: ***(a)*** *SEM image of Ni/DLC/Ni membrane suspended over a micromachined trench.* ***(b)*** *Optical image of transfered graphene onto round cavity structures. The circle in the cavity center indicates graphene sticking to the bottom of the structure.*[3]

Devices with more membrane-like graphene resonator components have also been investigated. Thibert *et al.* (2015) [120] have created a membrane out of diamond like carbon (DLC) in-between two layers of nickel (Ni) for support. As seen in Figure 5.4a, the membrane is suspended over a trench with a second electrode positioned at the bottom of the trench. The resonance frequency has not been determined experimentally, but simulations suggest resonance frequencies ranging from 15 MHz to 1 GHz. Chong *et al.* (2014) [121] have shown a configuration most resembling an actual CMUT device. Using micromachining steps round cavities are created onto which single-layer graphene is transfered. As seen in Figure 5.4b, the cavity is indeed covered by the graphene membrane. Despite the fact the graphene is sticking to the bottom of the cavity, frequency measurements have been performed determining a resonance frequency of 95 MHz.

Current research into conventional, silicon-based CMUT devices mainly focuses on improving the processing steps towards more precise dimension control of the structure, for example the cavity height [118, 122]. Although the frequencies generated by the graphene resonator and CMUT devices are within the MHz regime, the processing methods to construct such a device largely depend on the transfer of graphene on top of a CMUT base-structure. This method is not desirable for large scale production, mainly due to low reproducibility and transferal residues contaminating membrane areas. The solution for this problem has to be found in the processing of graphene membranes directly from the source wafer, making the incorporation in current full scale CMUT-processing easier and more cost-efficient for semiconductor companies. The graphene membranes in this thesis are fabricated bypassing the transfer process, making the processing more suitable for current semiconductor processing. It has to be noted, while single-layer graphene is generally grown using copper as the metal catalyst, this metal is extremely unsuitable for use in cleanrooms and even seen as pollutant [32]. Other metals such as nickel or molybdenum are more suitable for semiconductor processing, but generally result in the growth of multilayer graphene. In this chapter actuation of non-transfered freestanding multilayer graphene membranes is shown, in combination with modeling on possible device parameters.

5.3 Membrane actuation

In order to create a proof-of-princple CMUT-like configuration, the graphene membranes are suspended over a gap. Figure 5.5 shows the setup used in this section. A basic configuration is chosen, using a conducting wafer piece as second bottom electrode. Insulating tape ($t_{in} \approx 55\ \mu$m) is used as non-conducting material for the gap. On top of the two layers of insulating

[3]Image sources: Thibert *et al.* (2015) [120] and Chong *et al.* (2014) [121]

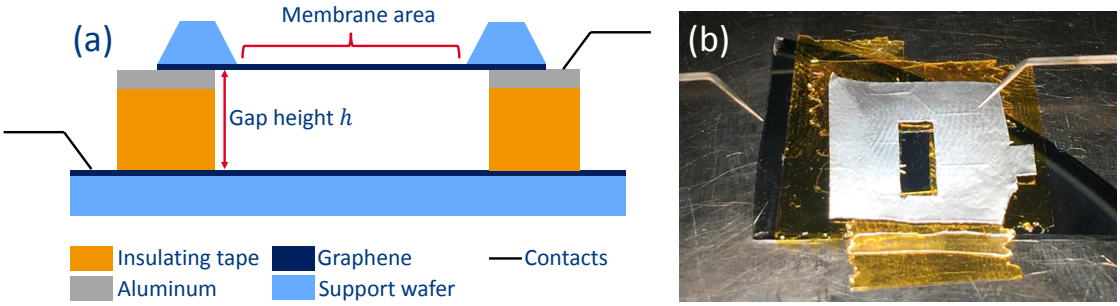

Figure 5.5: ***(a)*** *Schematic overview of the experimental setup used for membrane actuation. Insulating tape is patched on a bare graphene deposited wafer, on top of which aluminum foil is cut to similar dimensions. The sample is placed up-side-down on top of the aluminum, placing the membrane directly over the gap with height h.* ***(b)*** *Image of the voltage setup without the graphene membrane sample, visualizing the gap over which the membrane is placed.*

tape, shaped aluminum foil is placed ($t_{Al} \approx 10$ μm). The graphene membrane sample is placed up-side-down on top of the aluminum foil, being able to probe the graphene directly through the aluminum foil, since it is in direct contact. The electrical contacts are connected to a DC-voltage source, supplying voltages in the range of $0 - 1000$ V. To represent CMUT actuation, a DC- and AC-voltage source can also be placed in series, superimposing the alternating voltage while the membrane is electrostatically influenced. Membrane movement is captured by a camera, placed directly above the sample.

5.3.1 Electrostatic attraction

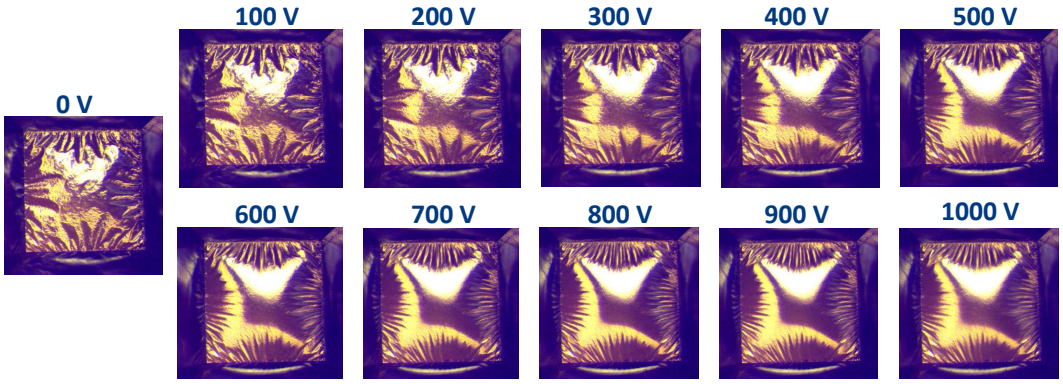

Figure 5.6: *Top view images of a square ∼1x1 mm^2 multilayer graphene membrane, $t = 11.5$ nm, suspended over a $h \approx 120$ μm gap while electrostatically actuated. The images show the membrane subjected to DC-voltages ranging from 0 to 1000 V.*

Figure 5.6 shows the DC actuation of a square ∼1x1 mm^2 multilayer graphene membrane ($t = 11.5$ nm), suspended over the gap, approximately $h = 120$ μ**m** in height ($2t_{in} + t_{Al}$). At 0V, it can be clearly seen the membrane is wrinkled, similar as shown earlier in this thesis. Increasing the voltage, the membrane wrinkles are smoothened out, attracting the graphene towards the bottom electrode[4]. Simultaneously, the number of wrinkles on the edge of the membrane increases, indicating increasing stress is applied to the membrane.

[4]Since the camera's point-of-view is directly above the membrane, it is not directly visible whether the membrane is deflecting upward or downward, but due to the nature of electrostatic attraction, it can be safely assumed the membrane is pulled downward.

In order to increase the electrostatic influence, the gap distance between the membrane and the bottom wafer is decreased further. By removing one of the two layers of insulating tape, the gap distance is reduced to only $h = 65$ μ**m** ($t_{in} + t_{Al}$). Since the electric field in the gap scales with $E = V/h$, it is estimated the electric field, and with that the force exerted on the membrane, is roughly two times as large as in the $h = 120$ μm gap configuration. Similar patterns of deflection as shown in Figure 5.6 can be identified, up until a voltage of ∼560 V. At this point membrane breakage is observed around the center of the membrane, see Figure 5.7, possibly due to physical contact between the membrane and the bottom electrode, causing a discharge. When comparing with the bulge experiments from Chapter 4 on the $t = 11.5$ nm membrane, the maximum strain is observed to be around $\epsilon = 0.01$. From geometrical considerations, it can be calculated that this strain corresponds to a maximum deflection of 62.5 μm, indeed similar to the estimated gap height.

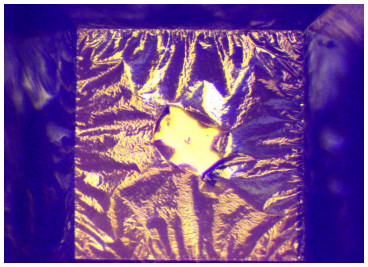

Figure 5.7: *Broken $t = 11.5$ nm membrane at 560 V.*

5.3.2 Membrane vibration

To resemble CMUT actuation, an AC voltage is applied to the graphene-CMUT structure and membrane oscillation is observed through video recordings. Initially, a 50 V, 1 Hz AC-voltage, without DC-bias, is applied to the membrane. This indeed initiates oscillations in the membrane, although an interesting feature is observed: While the driving voltage is set to 1 Hz, the membrane vibrates at a frequency of 2 Hz. An explanation for this doubled frequency can be found in the nature of the electrostatic force. One oscillation period exhibits both a minimum of -50 V and a maximum of +50 V. Since the reference voltage is 0 V, both extremes produce a voltage difference of 50 V over the gap, causing attraction of the membrane at two moment during a single period. It has to be noted oscillation of the membrane is not perfectly smooth, since the wrinkling distorts a clean oscillation pattern.

Similar 50 V, 1 Hz membrane resonance has also been delivered including a 100 V DC-bias. Applying the DC-bias indeed decreases the response frequency to 1 Hz, and since the increase in stress decrease the amount of wrinkles in the membrane, a more stable membrane resonance is observed. Higher frequencies are also supported by the membrane, which up to 20 Hz can still be observed by eye, indicating the membrane is stable enough to withstand fast driven oscillations.

5.4 CMUT characteristics modeling

Having shown proof-of-principle actuation of the graphene membranes, potential parameters of operation of a graphene-CMUT device are investigated. Main parameters of interest are (i) the capacitance of the CMUT structure, (ii) the collapse voltage and (iii) the resonance frequency of the CMUT [103]. The capacitance and collapse voltage indicate the range in which the CMUT can be operated, while the frequency determines the relevant field of application, as discussed in the Introduction of this chapter. First, the capacitance and collapse voltage of a graphene-CMUT like device are calculated for different geometrical dimensions, suggesting optimal device dimensions for processing purposes. Lastly, the operating frequency of the graphene membrane is discussed, one of the most crucial operating parameters since it determines which type of application it is most suitable for.

5.4.1 Capacitance

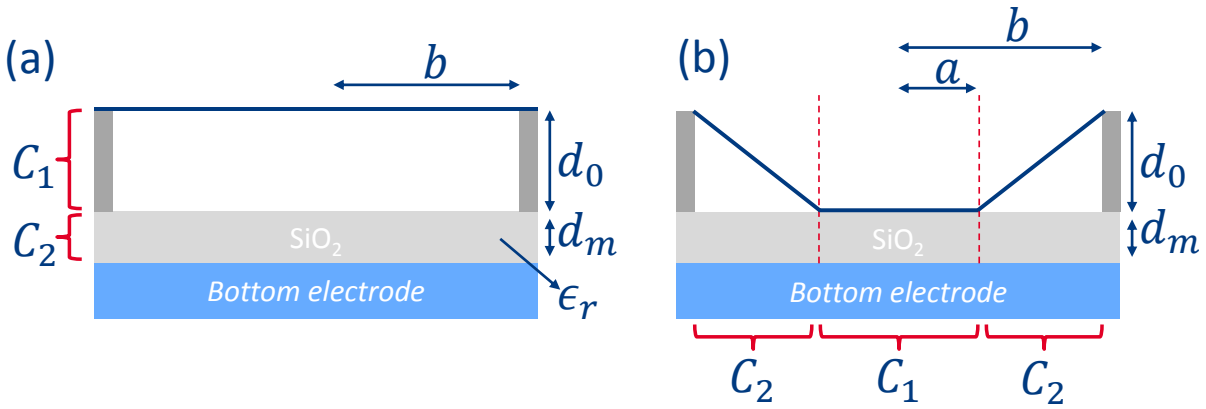

Figure 5.8: *Schematic cross section of CMUT configurations and corresponding parameters.* ***(a)*** *Configuration in which the membrane is not actuated and the total capacitance C consists of two capacitances in series C_1 and C_2 induced by the cavity and insulating SiO_2, respectively.* ***(b)*** *CMUT in collapse configuration in which part of the membrane touches the bottom of the cavity, covering an area with radius a. The total capacitance C in this configuration comprises two capacitances: A central round area C_1 for $0 < r < a$, and an edge capacitance C_2 for $a < r < b$, positioned in parallel.*

A CMUT device can be operated in two different modes: (i) vibration as a free membrane (Figure 5.8a), or (ii) in the so-called 'collapse mode'. Each mode provides a different operating regime with different frequencies and output pressures (Figure 5.8b) [123]. Since the ideal CMUT essentially consists of two electrodes separated by a gap, it can be approximated by the general formula for a parallel plate capacitance

$$C = \frac{\epsilon A}{h} \tag{5.1}$$

in which A equals the surface area of the electrodes, h the gap distance and ϵ the permittivity of the material between the two electrodes. Calculating the total capacitance C in the parallel configuration can be done by adding the reciprocal capacitances of the cavity $C_1 = \epsilon_0 \pi b^2/d_0$ and the insulting oxide layer $C_2 = \epsilon_0 \epsilon_r \pi b^2/d_m$ according to $1/C = 1/C_1 + 1/C_2$, resulting in the capacitance of the round CMUT device given by

$$C = \frac{\pi b^2 \epsilon_0}{d_0 + d_m/\epsilon_r} \tag{5.2}$$

with d_0 the distance of the gap, d_m the height of the insulating layer, b the radius of the membrane, ϵ_0 the vacuum permittivity and ϵ_r the relative permittivity of the insulating layer. In collapse mode the calculation of the capacitance becomes slightly more complicated, since now two regions can be distinguished, see Figure 5.8b: The region between $0 < r < a$ is given by the regular parallel plate capacitance over the insulating material, indicated by C_1. The second region between $a < r < b$ is given by a more complex capacitance C_2, which is composed of a non-linear capacitance over the cavity in series with a capacitance through the insulating material. The non-linear capacitance C_2 can be calculated by approximating the membrane profile $h(r)$, and with that the height of the gap, as a linear function of radius r: $h(r) = \frac{d_0}{b-a}(r-a)$. Similar to Equation 5.2 an expression can be derived for the capacitance C_2, integrating over small ring-shaped areas $dA = 2\pi r dr$ which are spaced a distance $h_{total} = h(r) + d_m/\epsilon_r$ of the bottom electrode. This gives the two different capacitances

$$\begin{aligned} 0 < r < a: \quad & C_1 = \frac{\pi a^2 \epsilon_0}{d_m/\epsilon_r} \\ a < r < b: \quad & C_2 = \int \frac{\epsilon dA}{h_{total}} = \int_a^b \frac{2\pi r \epsilon_0}{h(r) + d_m/\epsilon_r} dr \end{aligned} \tag{5.3}$$

in which the capacitance C_2 is found by analytically solving the integral. The factor $f = a/b$ is introduced as a measure for the fraction of the cavity that has collapsed, resulting in the full form of the two different capacitances:

$$C_1 = \frac{\pi f^2 b^2 \epsilon_0}{d_m/\epsilon_r} \tag{5.4}$$

$$C_2 = \frac{2\pi\epsilon_0 b^2 (1-f)^2}{d_0} \left(1 - \beta \cdot \ln\left(1 + (1-f)\frac{d_0}{d_m/\epsilon_r}\right)\right) \quad \text{with} \quad \beta = \frac{d_m/\epsilon_r}{d_0} - \frac{f}{1-f} \tag{5.5}$$

Since the two capacitances in this configuration are placed in parallel with respect to each other, the total capacitance C is found by simply adding the two individual capacitances

$$C = C_1 + C_2 \tag{5.6}$$

Figure 5.9 shows the capacitance as function of cavity height d_0 and membrane radius b, both in the parallel plate configuration 5.9a and in collapse mode 5.9b with $f = a/b = 0.5$. In both models the thickness of the SiO_2 is taken to be $d_m = 100$ nm with the corresponding relative permittivity $\epsilon_r = 3.9$. As can be expected from the general form of the capacitance, the capacitance increases quadratically with membrane radius $C \sim b^2$ and inversely with cavity height $C \sim 1/d_0$ in the parallel plate configuration, taking on values in the order of fF to pF. While these general trends seem to coincide with the collapse mode configuration, it is interesting to notice the decrease in dependence on the cavity height. This can be understood by the fact that the total capacitance C is largely governed by the capacitance of the collapsed part of the

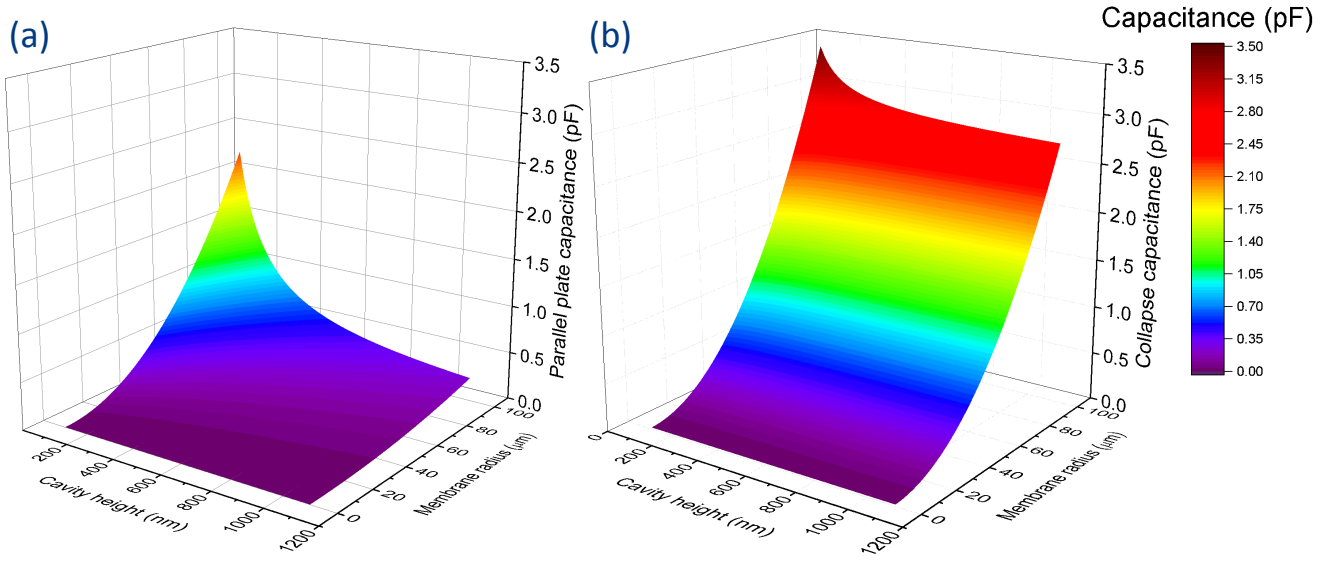

Figure 5.9: *Capacitance of a CMUT configuration as function of cavity height and membrane radius. Both the capacitance in the parallel plate configuration* ***(a)*** *is given according to Equation 5.2, as well as the capacitance in collapse* ***(b)*** *with $f = a/b = 0.5$ according to Equation 5.6 with the partial capacitances given by Equations 5.4 and 5.5.*

membrane C_1 from Equation 5.4. When the cavity height approaches the SiO_2 thickness, the effect of the edge capacitance C_2 becomes large, showing a more significant increase around $d_0 < 300$ nm. For typical CMUT dimensions around $d_0 = 500$ nm and $b = 50$ μm, the capacitance increases from $C = 134$ fF in the parallel plate configuration to around $C = 748$ fF in collapse mode. While this model provides insight in the capacitance of a single CMUT configuration, CMUTs are generally structured in arrays for 3D-imaging, for example 6 by 6 [123] or an 1D array of 128 elements [116]. This implies the total measurable capacitance being the sum of the number of individuals capacitances $N \cdot C$.

The increase in capacitance by a factor ~ 5.4 is much larger than reported by for example Oralkan *et al.* (2006) [123], reporting a relatively small 10% increase in capacitance when the membrane is pulled into collapse mode. This difference can largely be attributed to the smaller gap height $d_0 = 120$ nm and thicker insulating layer $d_m = 290$ nm used by Oralkan, while it is also unknown which fraction f of the membrane is in touch with the cavity. Future modeling would provide more insight into the relation between the force exerted on the membrane and the fraction which has collapsed. While the capacitance is a useful device characteristic, the model shown here does not require any input on membrane characteristics, being a very general (high level) description of the capacitance. The next section does provide a more graphene multilayer specific description, focusing on the DC-voltage required to pull the membrane into collapse mode.

5.4.2 Collapse voltage

As demonstrated in section 5.3 and as part of the CMUT working principle, the CMUT membrane can be actuated by a DC-voltage. As shortly touched upon in the previous section, the membrane can also be actuated in collapse mode, which can be created by applying a high enough DC-voltage overcoming the mechanical stiffness of the membrane. This results in the membrane collapsing on the bottom of the cavity. This section provides a method to calculate the maximum DC-voltage which can be applied to the membrane, the so-called collapse voltage, before it falls into collapse mode. This method is largely based on calculations by Wygant *et al.* (2006) [124].

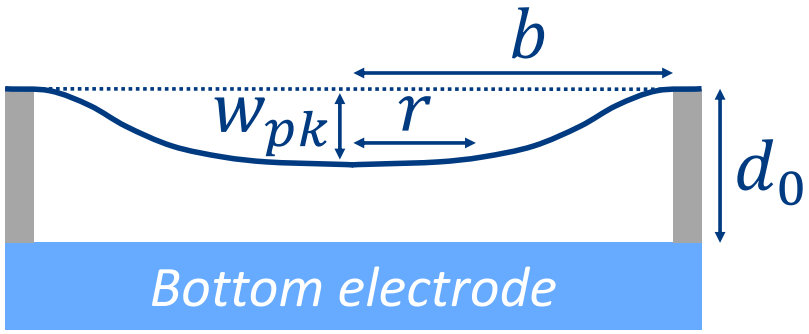

Figure 5.10: *Schematic description of the CMUT configuration for calculation of the collapse voltage.*

When a DC-voltage is applied to the configuration, the membrane experiences an electric force

$$F_e = \frac{1}{2} V^2 \frac{dC}{w_{avg}} \tag{5.7}$$

which is proportional to the applied voltage V^2 and the change in capacitance as function of

the average membrane displacement $\frac{dC}{w_{avg}}$. The capacitance over the gap as function of the average displacement w_{avg} is given by

$$C = \frac{\epsilon_0 \pi b^2 \operatorname{arctanh}(\sqrt{3w_{avg}/d_0})}{\sqrt{3w_{avg}d_0}} \tag{5.8}$$

with d_0 the total gap height and πb^2 the circular membrane area. The capacitance can be derived using the deflection profile $w(r) = w_{pk}(1 - r^2/b^2)^2$, see Figure 5.10, with the peak deflection w_{pk} related to the average deflection through $w_{pk} = 3w_{avg}$. An advantage of this expression is that it takes the capacitance as function of the deflection profile into account, in contrast to other models which in general assume a parallel plate capacitance. A concession has to be made though, since the effect of the insulating SiO_2 layer is neglected.

While the plate is electro-statically attracted to the bottom electrode, it tends to move back to its original position by the mechanical response F_m of the membrane. In the case of small deflections the mechanical force follows Hooke's law, having only a linear response to the average plate displacement w_{avg}. Since in this configuration the average deflection becomes relatively large, it is representative to include a term that is proportional to the cubic of the average deflection w_{avg}^3

$$F_m = k_1 w_{avg} + k_3 w_{avg}^3 \tag{5.9}$$

with the corresponding linear and cubic spring constant given by

$$\begin{aligned} k_1 &= \frac{192\pi D}{b^2} \quad \text{with} \quad D = \frac{Et^3}{12(1-\nu^2)} \\ k_3 &= D\frac{-24\pi(-896585 - 529610\nu + 342831\nu^2)}{29645b^2t^2} \end{aligned} \tag{5.10}$$

respectively. Here the influence of material parameters becomes apparent, with D the flexural rigidity of the material, E the Young's modulus, ν the Poisson ratio and t the thickness of the membrane.

In order to reach an equilibrium deflection situation the electric force F_e has to equal the mechanical force F_m for a certain plate deflection w_{avg}

$$F_e(w_{avg}) = F_m(w_{avg}) \tag{5.11}$$

For small forces Equation 5.11 can be solved for w_{avg}. When the voltage V is increased further, at some point the mechanical force F_m is unable to withhold the electric force F_e, resulting in the membrane collapsing onto the bottom of the cavity. The collapse voltage in this work is found by numerically increasing the voltage V until no solution can be found for Equation 5.11, appointing the corresponding voltage as the collapse voltage. The parameters used for calculation of the collapse voltage are: $E = 0.7$ TPa for the Young's modulus, $\nu = 0.24$ as the Poisson ratio and $t = 8$ nm for the thickness. It is expected the high value for the Young's modulus can be reached when improving process steps, and crumpling of the graphene membranes is decreased. The Poisson ratio is chosen to be that of HOPG [99], which has a similar structure as multilayer graphene. It has to be noted the Poisson ratio can vary largely with increasing stress, as observed in the previous chapter. A thickness of 8 nm is chosen as representative value for a multilayer graphene stack.

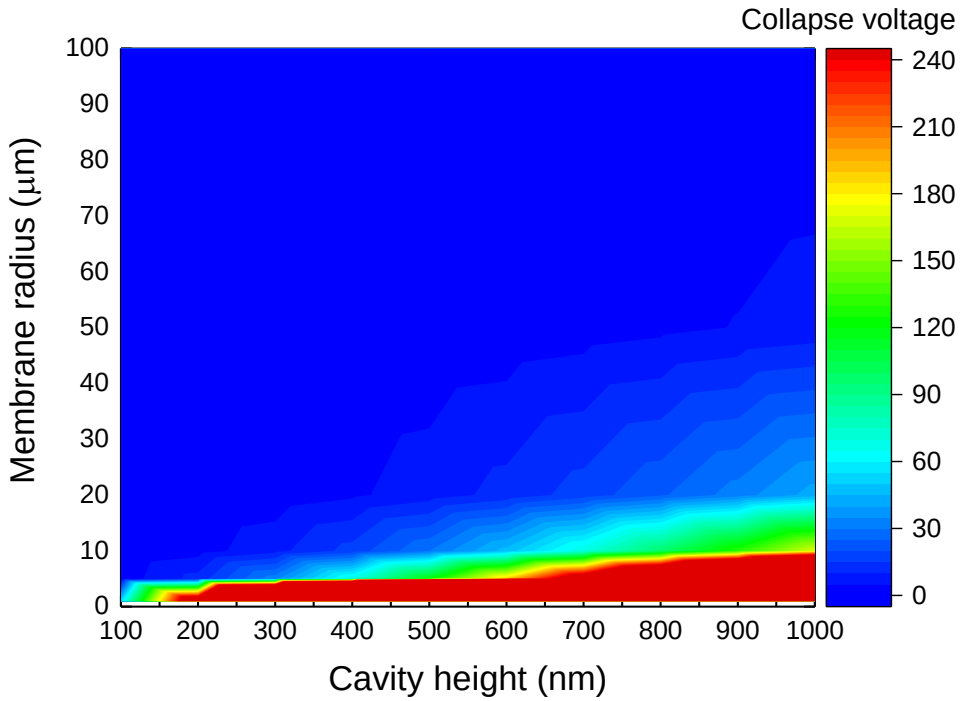

Figure 5.11: *Collapse voltage as function of membrane radius and cavity height. Membrane parameters of $E = 0.7$ TPa, $\nu = 0.24$ and $t = 8$ nm are chosen to represent typical graphene multilayer parameters.*

Figure 5.11 shows the collapse voltage of the modeled multilayer graphene membrane as function of membrane radius b and cavity height d_0. It can be seen relatively low voltages (<5 V) are needed to pull the membrane into collapse mode. This sharply increases towards smaller radii below 20 μm, rising to well above 200 V. It can be understood that large membranes require less voltage to pull the membrane into collapse, since the mechanical force decreases with increasing radius $F_m \sim 1/b^2$ and exactly the opposite applies to the electric force $F_e \sim b^2$, Although the collapse voltage is relatively low compared to standard CMUT devices, 130 V for a silicon membrane ($d_0 = 500$ nm, $b = 15$ μm and $t = 1$ μm) [125] and 100V for a silicon nitride membrane ($d_0 = 120$ nm, $b = 15$ μm and $t = 900$ μm) [123], recent measurements by Metten *et al.* (2016) [126] have observed similar low collapse voltages for graphene-CMUT like structures. Metten shows a single-layer graphene membrane suspended over a trench ($d_0 = 288$ nm and width of 4.9 μm) with a second electrode placed under 212 μm of SiO_2, resulting in a collapse voltage of 20 V, compared to 120 V for dimensions of in this model $d_0 = 500$ nm, $b = 5$ μm. The discrepancy in collapse voltage can be largely attributed to the difference in thickness, varying a factor of ~23. Additionally, the effect of the insulating SiO_2 layer is neglected in this model, attributing to a lower than actually present collapse voltage.

The model in this section shows collapse voltages calculated for a typical multilayer graphene membrane. Main finding is the strong dependence of the collapse voltage on the membrane radius, suggesting geometrical parameters around $d_0 \approx 500$ nm and $b \approx 10$ μm for collapse voltages useful for applications, $V \sim 30$ V. The next section discusses the last parameter of interest, the resonance frequency, determining the potential of graphene-CMUT devices for ultrasound applications.

5.4.3 Frequency modeling

One of the key characteristics of ultrasound devices is its resonance frequency. In order to acquire an insight into possible resonance frequencies of the multilayer graphene membranes used in this thesis, the resonance frequency of circular membranes is calculated according to

$$f_0 = \frac{1}{2\pi}\sqrt{\frac{k}{m}} = \frac{1}{2\pi}\frac{10.22t}{b^2}\sqrt{\frac{E}{12\rho(1-\nu^2)}} \tag{5.12}$$

in which the spring constant k is given by the mechanical stiffness k_m and the mass m by the effective mass m_{eff} of circular clamped membranes [127]

$$k = k_m = \frac{16\pi E t^3}{b^2(1-\nu^2)} \qquad m = m_{eff} = 1.84\pi b^2 \rho t \tag{5.13}$$

with ρ the density of the membrane material. Similar to the previous section, the parameters for multilayer are chosen to be $t = 8$ nm, $E = 700$ GPa and $\nu = 0.24$, with the density of the graphene given by $\rho = 2200$ kg/m^3, similar to the density of graphite [128]. The simulated results are compared with resonance frequencies of a silicon nitride membrane with a thickness of $t = 400$ nm and mechanical parameters $E = 222$ GPa and $\nu = 0.28$ [27], and a density of $\rho = 3400$ kg/m^3 [129].

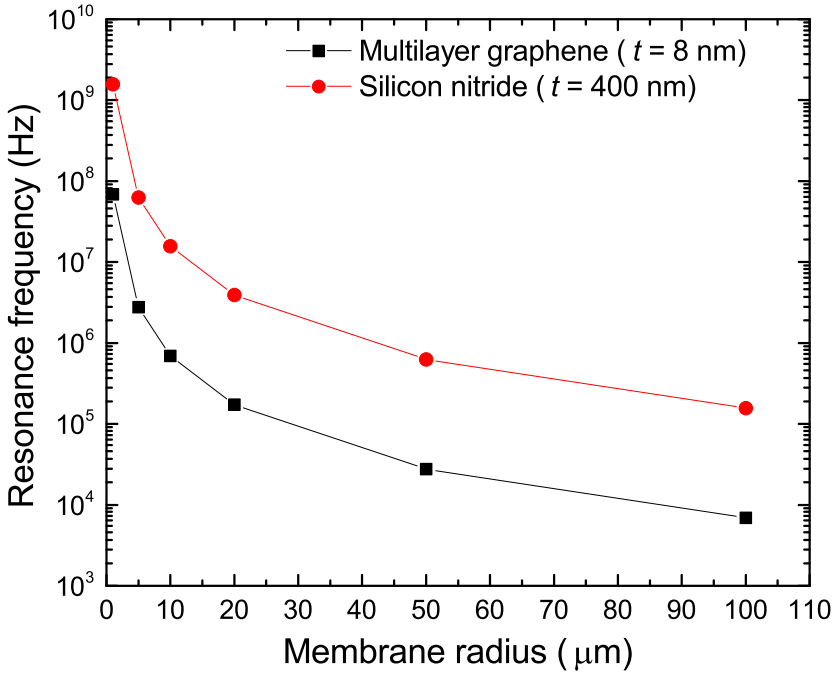

Figure 5.12: *Resonance frequency as function of membrane radius for a silicon nitride membrane ($t = 400$ nm, $E = 222$ GPa, $\nu = 0.28$ and $\rho = 3440$ kg/m^3) and multilayer graphene ($t = 8$ nm, $E = 700$ GPa, $\nu = 0.24$ and $\rho = 2200$ kg/m^3).*

Figure 5.12 shows the simulated resonance frequency of the multilayer graphene membrane and the silicon nitride membrane as function of the membrane radius. While the upward trend with decreasing radius can be expected from Equation 5.12, the graphene membrane exhibits resonance frequencies a factor of ∼10 lower than the silicon nitride membrane. Main reason for this difference is the thickness variation between the two membranes t, largely governing the resulting resonance frequency. Around dimensions of $b = 10 - 20$ μm the resonance frequency of multilayer graphene reaches values around $10^5 - 10^6$ Hz. This approaches the MHz regime,

showing potential for medical imaging. These frequencies are lower than produced by experimentally created graphene resonators, generally in the order of 10-200 MHz (see Zhang *et al.* (2015) [28] for a clear overview on graphene mechanical resonators), even reaching 1 GHz as calculated by Poot *et al.* (2008) [130]. Below possible scenarios for this difference are illustrated.

The model used in this section is a very elementary first order approximation of the resonance frequency of a circular multilayer graphene membrane. Other factors that influence the resonance frequency can cause frequency shifts up to multiple orders of magnitude. The main effect influencing CMUT operation is the DC-actuation of the membrane. It is known that a DC-voltage decreases the effective stiffness k and with that resonance frequency f_0 of the membrane [131]. Although this effect can take place in graphene-CMUT devices, it is more likely the resonance frequency is increased due to an increase in tension in the membrane. This process is similar to the tuning of a guitar string, already observed in different graphene resonator devices [132, 133, 134]. Additionally, the output in terms of amplitude, or dB, of the sounds waves has been outside the scope of this thesis, where it can be crucial for the penetration depth of the sounds waves to achieve a minimum oscillation strength. Before these effects can be incorporated in a model for actuation of circular graphene-CMUT-like membranes, first the experimental preparation of flat graphene membranes has to be realized. As has been shown in the previous chapter, the graphene exhibits multiple wrinkling effects which largely influence its mechanical response. It is crucial to first create non-wrinkled membranes before the characterization of parameters such as the frequency and amplitude strength can be performed.

5.5 Conclusion

In this chapter an outlook has been given on the application of multilayer graphene membranes in capacitive micromachined ultrasound transducers, CMUTs. The graphene has the potential to simultaneously act as both membrane and top electrode, replacing the original concept of an electrode packed in between an insulating membrane.

In this work proof-of-principle electronic actuation of non-transfered multilayer graphene membranes has been shown. Applying DC-voltages up to 1000V for 1x1 mm^2 membranes suspended over a 120 μm high gap, membrane actuation is captured by a camera, directly observing the electrostatic membrane actuation. Simultaneously, AC-voltages are applied simulating CMUT-operation. This confirms the graphene membranes can be actuated using oscillating signals, both unbiased and when imposing a DC-voltage.

Information on possible operating parameters has been acquired by modeling of the multilayer graphene membranes structures. Although individual predicted values for the capacitance are relatively low ($\sim$100 fF), CMUTs are generally structured in arrays for amongst others 3D-imaging. This implies a higher total capacitance and being well within range of standard measuring equipment. Modeling of the collapse voltage and resonance frequency suggest ideal dimensions of graphene-CMUT dimensions are around a gap height of $d_0 = 500$ nm and membrane radius $b = 10$ μm, resulting in a collapse voltage of $\sim$30 V and resonance frequencies of $\sim 10^6$ Hz, suitable for medical applications.

While the simulations and proof-of-principle actuation suggests multilayer graphene membrane can indeed be used in electromechanical resonators, information on critical parameters such as output pressure in dB has been outside of the scope of this work. It would be of great interest to create array-structured graphene-CMUT devices and test actual output parameters

to validate application opportunities. A different point of interest is the wrinkling of the graphene membranes, already observed in the previous chapter, which is generally ignored in modeling of the output parameters. Improvements from a processing point of view are essential in create suitable graphene membranes for applications purposes.

Chapter 6

Conclusions and outlook

This chapter combines the individual research areas, relating back to the research questions formulated at the beginning of this thesis. The conclusions of the three different research areas are discussed, after which an outlook for future research and recommendations for further development is given.

6.1 Thesis conclusions

Graphene is considered one of the strongest and thinnest materials in existence today, showing potential for incorporation in optical windows and electromechanical resonators. For future development and further upscaling towards larger freestanding membrane areas, is it essential to study the characteristics of these multilayer graphene membranes. Factors including the thickness and mechanical response can determine the robustness of the membranes, making these aspects of the graphene membranes focus areas of this thesis.

The thickness of the multilayer graphene membranes is studied with UV-vis spectroscopy ($\sim$250-1100 nm). It is shown that excitonic resonance, the so-called Fano resonance effect, causes an asymmetric transmission profile. This indicates that the optical conductivity of multilayer graphene is strongly energy dependent in the UV-vis regime $\sigma \sim \sigma(E)$, similar to what is observed in single-layer graphene. The number of layers, and with that the graphene thickness, is determined by fitting of the in this thesis proposed UV-vis model, additionally cross-referenced with AFM measurements. The UV-vis model provides additional information on the optical properties of the multilayer graphene, showing very short exciton lifetimes $\sim$30 fs. This can be attributed to the presence of defects in the graphene lattice, indeed observed in the Raman spectra. Based on the fitted transmission curves, the UV-vis model can be used to predict reflection of the graphene membranes, a property generally ignored in optical research on graphene. The measured reflection of the multilayer graphene membranes agrees reasonably well with the modeled reflection, with deviations towards higher energies probably due to diffuse reflection on the rough surface of the graphene membrane. The results clearly show that reflection cannot be neglected for multilayer graphene.

The mechanical response of the graphene membranes is determined using the thickness determined through UV-vis spectroscopy as input. This thesis has shown that the method of bulge testing indeed can be applied to large scale $\sim$mm^2 graphene membranes. For multilayer graphene membranes with a thickness of $t = 11.5$ nm, the **effective** stress-strain responses E_b and E_p show a non-linear behavior. Using two different membrane configurations it is shown the **intrinsic** Young's modulus is relatively constant around $E \approx 80$ GPa. The Poisson ratio on the other hand increases from near zero, thus low directionally dependence, to values

close to the isotropic limit of $\nu = 0.5$. This suggests the Poisson ratio is the largest contributor to the non-linear effective response. SEM-images confirm crumpling of the graphene membranes, possibly contributing to the varying Poisson ratio. Quantitative analysis of the non-linear response confirms the stress follows a non-linear strain response at low stress $\epsilon \sim \sigma^{\alpha}$ and reaching an expected linear response at high stress $\epsilon \sim \sigma$. Unfortunately, this theory only describes bulging in a specific configuration, thus neglecting any effects from the Poisson ratio, as suggested by this thesis to have a significant effect. Thinner graphene membranes with a thickness of $t = 2.76$ nm have also been analyzed, showing a larger stiffness of $E \approx 150$ GPa. Although closer to the value of $E \sim 1$ TPa predicted for single-graphene, the response is still lower, most likely due the multilayer membranes being more resemblant to HOPG or graphite, having values of $E = 15 - 30$ GPa.

Having characterized both the thickness and mechanical response, a possible application for the graphene membranes is studied in the form of capacitive micromachined ultrasound transducers, CMUTs. While proof-of-principle electromechanical membrane actuation has been shown on the freestanding graphene membranes, the large scale wrinkling is an effect which has to be resolved before implementing the graphene membranes into ultrasound transducers. If these problems would be resolved, optimal geometrical configurations would be around a cavity height of $d_0 = 500$ nm and a membrane radius of $b = 10$ μm, resulting in a collapse voltage of $V \approx 30$ V and expected resonance frequencies of $10^5 - 10^6$ Hz, suitable for medical applications.

6.2 Outlook and recommendations for future research

This thesis shows a detailed description of multilayer graphene membranes, both from an optical and mechanical point of view. Additionally some attention points for future development were indicated, as well as interesting future research opportunities for gaining a more complete understanding of the physics behind multilayer graphene membranes.

The most distinct effect observed in this thesis is the crumpling of the graphene membranes. It has been shown that this effect has a large impact on the effective mechanical response during bulging. While current research has focused on the effect of this crumpling on the mechanical response, this work suggest the Poisson ratio actually is the largest contributor. It would be interesting to investigate the effect of crumpling on the Poisson ratio of graphene membranes, possibly by creating crumpling-engineered graphene structures. Simultaneously, theoretical work on the Poisson ratio for crumpled graphene can provide insight into the strength of this effect and how it relates to the value of $\nu = 0.16$ generally used throughout literature.

AFM and SEM-images suggest the crumpling is largely caused by the roughness of the underlaying metal catalyst. It is very likely this is effect occurs during growth of the graphene. Since the growth process of the multilayer graphene has been outside the scope of this work, factors that could have been the cause of crumpling have not been investigated. It would be interesting to examine the effect of different metal catalysts on the graphene's surface roughness. Additionally, this would be a good method to objectively investigate the effect of crumpling on the mechanical response of graphene membranes with similar thicknesses, whereas in this thesis the comparison has to be made between two graphene membrane types with different thicknesses. Furthermore, the SEM-images show the large number of defects in the graphene membranes. These defects are possible causing the membranes to rupture before the intrinsic linear elastic response $\epsilon \sim \sigma$ is achieved. As pointed out in Chapter 4, the difference between the **stiffness** and **strength** of a material has to be taken into account towards possible applica-

tions. While the stiffness of the thinner graphene membranes is a positive effect, the absolute pressure the membranes can withstand is actually lower. Most likely the absolute strength of the membranes increases when the number of defects is decreased. It is still expected the thinner graphene membrane will break at lower pressures compared to thicker membranes. Somewhere an equilibrium might be reached, where the optimum thickness of the multilayer membranes still meets the requirements for amongst others optical windows. Here the UV-vis transmission model can also be used, investigating the exciton coupling and lifetimes observed in the multilayer graphene membranes and how they relate to the defect density in the membranes.

Towards possible applications the potential of graphene in CMUTs has also been investigated. While the current investigation states a positive outlook for the application of graphene membranes in ultrasound transducers, an important parameter, the amplitude of the sound waves in dB, has been outside of the scope of this thesis. Both the amplitude and the crumpling effect have to be investigated before stating a definite answer to this research question, and whether or not the graphene resonators indeed exhibit superior characteristics over current membrane materials. The outcome could be that graphene membranes simply cannot be processed without wrinkles. In that case heterostructured membranes could be potentially investigated. Graphene could still provide the advantage of a membrane with a large strength-to-weight ratio, while a different material could be stress-engineered to create tensile membranes.

Alongside the work described in this thesis, attempts have been made to create more CMUT-like array devices with multilayer graphene membranes. While large steps have been made towards a proof-of-principle device, processing of the graphene membranes in combination with CMUT-like device components still needs improvement. Mainly wet-ech techniques have been used, where it would be interesting to investigate to what extend these can be replaced by dry-etching techniques. The bulk of the graphene membranes break during drying, where it is expected dry-etching techniques would greatly enhance yield of the graphene membranes.

Acknowledgements

The past year has been a leap into a completely new research topic for me: graphene. Philips Innovation Services has provided me the opportunity to contribute to research on graphene membranes, for which I am grateful to have been a part. Combining my work at Philips at the High Tech Campus with work at the PMP group at the university was a nice change of scenery. It has given me a good insight in seeing the different ways of working at Philips and the PMP group at the TUe. I will not forget the winter days in which I had to cycle from the HTC to the university, holding a stack of boxes with extremely fragile graphene membranes with my bare hands.

First and foremost, I would like to thank my supervisors for their great guidance during this graduation project: Ageeth from the PMP group at the university, and Jos and Johan from Philips. All of you have been great discussion partners with whom I could discuss all my ideas. Jos, I would like to thank you in particular. On a regular basis I came to you with "just a small question", which easily turned into half an hour of discussion back and forth. Your knowledge of graphene and enthusiasm were one of the things that have kept me motivated throughout this graduation project.

Since my work has covered a broad range of topics, ranging from optical measurements on graphene to electromechanical actuation, I had to have access to multiple experimental setups. Being both at the university and at Philips, this work also involved getting in touch with a lot of different people. Therefore, I would like to thank Salman Shafqat, Johan Hoefnagels, Olaf van der Sluis and Marc van Maris for their help in using the bulge test setup, and their knowledge on bulge testing, a topic which was completely new to me. Lastly, a big thank you to Peter and Eugene for helping me with all the practical challenges when working in the cleanroom and the chemical labs at Philips. Your much-needed help has greatly contributed to the work described in this thesis.

Besides all the employees and staff of PMP and Philips, I would like to thank the other MSc students at the working space at the university: Roderick, Berit, Karsten, Siebe, Marlous, Patrick, Marc and Boy. You made for a nice and relaxing ambiance and were always in for a little chat, whether it was study-related or simply asking how the weekend was going to look like.

Last but not least, I would like to thank my family, friends and girlfriend Susanne: without you all this work would have never been possible. I am grateful for your continuous support, not only throughout the past year, but also my whole period as a student in Eindhoven. You have never seized to show interest in my studies, even when trying to grasp physical concepts which were hard for me to explain: Bedankt!

Bibliography

[1] E. P. Randviir, D. A. C. Brownson, and C. E. Banks, "A decade of graphene research: Production, applications and outlook," *Materials Today*, vol. 17, no. 9, pp. 426–432, 2014.

[2] H. Shen, L. Zhang, M. Liu, and Z. Zhang, "Biomedical applications of graphene," *Theranostics*, vol. 2, no. 3, pp. 283–294, 2012.

[3] F. Bonaccorso, Z. Sun, T. Hasan, and A. C. Ferrari, "Graphene Photonics and Optoelectronics," *Nature Photonics*, vol. 4, no. 9, pp. 611–622, 2010.

[4] L. Huang, M. Zhang, C. Li, and G. Shi, "Graphene-Based Membranes for Molecular Separation," *The Journal of Physical Chemistry Letters*, vol. 6, pp. 2806–2815, jul 2015.

[5] H. M. Hegab and L. Zou, "Graphene oxide-assisted membranes: Fabrication and potential applications in desalination and water purification," *Journal of Membrane Science*, vol. 484, pp. 95–106, jun 2015.

[6] X. Wang, L. Zhi, and K. Müllen, "Transparent, conductive graphene electrodes for dye-sensitized solar cells," *Nano Letters*, vol. 8, no. 1, pp. 323–327, 2008.

[7] A. K. Geim and K. S. Novoselov, "The rise of graphene," *Nature Materials*, vol. 6, pp. 183–191, mar 2007.

[8] R. Peierls, "Quelques propriétés typiques des corps solides," *Annales de l'I.H.P.*, vol. 5, no. 3, pp. 177–222, 1935.

[9] K. S. Novoselov, "Electric Field Effect in Atomically Thin Carbon Films," *Science*, vol. 306, pp. 666–669, oct 2004.

[10] K. S. Novoselov, V. I. FalâĂško, L. Colombo, P. R. Gellert, M. G. Schwab, and K. Kim, "A roadmap for graphene," *Nature*, vol. 490, pp. 192–200, oct 2012.

[11] K. I. Bolotin, K. J. Sikes, Z. Jiang, M. Klima, G. Fudenberg, J. Hone, P. Kim, and H. L. Stormer, "Ultrahigh electron mobility in suspended graphene," *Solid State Communications*, vol. 146, no. 9-10, pp. 351–355, 2008.

[12] Y. Zhang, Y.-W. Tan, H. L. Stormer, and P. Kim, "Experimental observation of the quantum Hall effect and Berry's phase in graphene.," *Nature*, vol. 438, no. 7065, pp. 201–204, 2005.

[13] K. S. Novoselov, Z. Jiang, Y. Zhang, S. V. Morozov, H. L. Stormer, U. Zeitler, J. C. Maan, G. S. Boebinger, P. Kim, and A. K. Geim, "Room-Temperature Quantum Hall Effect in Graphene," *Science*, vol. 315, no. 5817, p. 1379, 2007.

[14] "Graphene - the perfect atomic lattice." Nobel Committee for Physics (2010). at `https://www.nobelprize.org/nobel_prizes/physics/laureates/2010/illpres.html`.

[15] Y. Han, K. X. Nguyen, Y. Ogawa, J. Park, and D. A. Muller, "Atomically Thin Graphene Windows That Enable High Contrast Electron Microscopy without a Specimen Vacuum Chamber," *Nano Letters*, vol. 16, pp. 7427–7432, dec 2016.

[16] Y. Xu, Z. Guo, H. Chen, Y. Yuan, J. Lou, X. Lin, H. Gao, H. Chen, and B. Yu, "In-plane and tunneling pressure sensors based on graphene/hexagonal boron nitride heterostructures," *Applied Physics Letters*, vol. 99, p. 133109, sep 2011.

[17] A. Kolmakov, D. A. Dikin, L. J. Cote, J. Huang, M. K. Abyaneh, M. Amati, L. Gregoratti, S. Günther, and M. Kiskinova, "Graphene oxide windows for in situ environmental cell photoelectron spectroscopy," *Nature Nanotechnology*, vol. 6, no. 10, pp. 651–657, 2011.

[18] J. Kraus, R. Reichelt, S. Günther, L. Gregoratti, M. Amati, M. Kiskinova, A. Yulaev, I. Vlassiouk, and A. Kolmakov, "Photoelectron spectroscopy of wet and gaseous samples through graphene membranes," *Nanoscale*, vol. 6, no. 23, pp. 14394–14403, 2014.

[19] J. D. Stoll and A. Kolmakov, "Electron transparent graphene windows for environmental scanning electron microscopy in liquids and dense gases," *Nanotechnology*, vol. 23, no. 50, p. 505704, 2012.

[20] M. W. P. van de Put, J. P. Patterson, P. H. H. Bomans, N. R. Wilson, H. Friedrich, R. A. T. M. van Benthem, G. de With, R. K. O'Reilly, and N. A. J. M. Sommerdijk, "Graphene oxide single sheets as substrates for high resolution cryoTEM," *Soft Matter*, vol. 11, no. 7, pp. 1265–1270, 2015.

[21] E. E. Gallagher, J. Vanpaemel, I. Pollentier, H. Zahedmanesh, C. Adelmann, C. Huyghebaert, R. Jonckheere, and J. U. Lee, "Properties and performance of EUVL pellicle membranes," in *Proceedings of SPIE - The International Society for Optical Engineering* (N. Hayashi and B. S. Kasprowicz, eds.), p. 96350X, oct 2015.

[22] S.-G. Kim, D.-W. Shin, T. Kim, S. Kim, J. H. Lee, C. G. Lee, C.-W. Yang, S. Lee, S. J. Cho, H. C. Jeon, M. J. Kim, B.-G. Kim, and J.-B. Yoo, "Large-scale freestanding nanometer-thick graphite pellicles for mass production of nanodevices beyond 10 nm," *Nanoscale*, vol. 7, no. 35, pp. 14608–14611, 2015.

[23] M. Nasalevich, P. J. van Zwol, E. Abegg, P. Voorthuijzen, D. Vles, M. Péter, W. van der Zande, and H. Vermeulen, "Researching new EUV pellicle films for source powers beyond 250 watts," in *Proceedings of SPIE - The International Society for Optical Engineering* (U. F. Behringer and J. Finders, eds.), p. 10032, oct 2016.

[24] S. Zhu, S. Yuan, and G. C. A. M. Janssen, "Optical transmittance of multilayer graphene," *EPL (Europhysics Letters)*, vol. 108, p. 17007, oct 2014.

[25] G. Cao, "Atomistic Studies of Mechanical Properties of Graphene," *Polymers*, vol. 6, pp. 2404–2432, sep 2014.

[26] R. J. Nicholl, H. J. Conley, N. V. Lavrik, I. Vlassiouk, Y. S. Puzyrev, V. P. Sreenivas, S. T. Pantelides, and K. I. Bolotin, "The effect of intrinsic crumpling on the mechanics of free-standing graphene," *Nature Communications*, vol. 6, p. 8789, nov 2015.

[27] J. Vlassak and W. Nix, "A new bulge test technique for the determination of Young's modulus and Poisson's ratio of thin films," *Journal of Materials Research*, vol. 7, pp. 3242–3249, dec 1992.

[28] W.-M. Zhang, K.-M. Hu, Z.-K. Peng, and G. Meng, "Tunable Micro- and Nanomechanical Resonators," *Sensors*, vol. 15, pp. 26478–26566, oct 2015.

[29] G. Caliano, F. Galanello, A. Caronti, R. Carotenuto, M. Pappalardo, V. Foglietti, and N. Lamberti, "Micromachined ultrasonic transducers using silicon nitride membrane fabricated in PECVD technology," in *2000 IEEE Ultrasonics Symposium. Proceedings. An International Symposium (Cat. No.00CH37121)*, vol. 1, pp. 963–968, IEEE, 2000.

[30] Y. Chen, X.-L. Gong, and J.-G. Gai, "Progress and Challenges in Transfer of Large-Area Graphene Films," *Advanced Science*, vol. 3, p. 1500343, aug 2016.

[31] B. AlemaÌĄn, W. Regan, S. Aloni, V. Altoe, N. Alem, C. Girit, B. Geng, L. Maserati, M. Crommie, F. Wang, and A. Zettl, "Transfer-Free Batch Fabrication of Large-Area Suspended Graphene Membranes," *ACS Nano*, vol. 4, pp. 4762–4768, aug 2010.

[32] Y. Grachova, S. Vollebregt, A. L. Lacaita, and P. M. Sarro, "High Quality Wafer-scale CVD Graphene on Molybdenum Thin Film for Sensing Application," *Procedia Engineering*, vol. 87, pp. 1501–1504, 2014.

[33] R. Muñoz and C. Gómez-Aleixandre, "Review of CVD Synthesis of Graphene," *Chemical Vapor Deposition*, vol. 19, pp. 297–322, dec 2013.

[34] K. L. Saenger, J. C. Tsang, A. A. Bol, J. O. Chu, A. Grill, and C. Lavoie, "In situ x-ray diffraction study of graphitic carbon formed during heating and cooling of amorphous-C/Ni bilayers," *Applied Physics Letters*, vol. 96, no. 15, pp. 2010–2013, 2010.

[35] A. C. Ferrari and D. M. Basko, "Raman spectroscopy as a versatile tool for studying the properties of graphene.," *Nature nanotechnology*, vol. 8, pp. 235–46, apr 2013.

[36] A. C. Ferrari, "Raman spectroscopy of graphene and graphite: Disorder, electron-phonon coupling, doping and nonadiabatic effects," *Solid State Communications*, vol. 143, pp. 47–57, jul 2007.

[37] F. Tuinstra and L. Koenig, "Raman Spectrum of Graphite," *The Journal of Chemical Physics*, vol. 53, no. 5, pp. 1126–1130, 1970.

[38] A. Eckmann, A. Felten, A. Mishchenko, L. Britnell, R. Krupke, K. S. Novoselov, and C. Casiraghi, "Probing the nature of defects in graphene by Raman spectroscopy," *Nano Letters*, vol. 12, pp. 3925–3930, aug 2012.

[39] R. Beams, L. Gustavo Cançado, and L. Novotny, "Raman characterization of defects and dopants in graphene," *Journal of Physics: Condensed Matter*, vol. 27, p. 083002, mar 2015.

[40] D. Graf, F. Molitor, K. Ensslin, and C. Stampfer, "Spatially resolved Raman spectroscopy of single-and few-layer graphene," *Nano letters*, vol. 7, pp. 238–42, 2007.

[41] A. C. Ferrari, J. C. Meyer, V. Scardaci, C. Casiraghi, M. Lazzeri, F. Mauri, S. Piscanec, D. Jiang, K. S. Novoselov, S. Roth, and A. K. Geim, "Raman spectrum of graphene and graphene layers," *Physical Review Letters*, vol. 97, no. 18, pp. 1–4, 2006.

[42] D. R. Lenski and M. S. Fuhrer, "Raman and optical characterization of multilayer turbostratic graphene grown via chemical vapor deposition," *Journal of Applied Physics*, vol. 110, no. 1, 2011.

[43] W. Fang, A. L. Hsu, R. Caudillo, Y. Song, A. G. Birdwell, E. Zakar, M. Kalbac, M. Dubey, T. Palacios, M. S. Dresselhaus, P. T. Araujo, and J. Kong, "Rapid identification of stacking orientation in isotopically labeled chemical-vapor grown bilayer graphene by Raman spectroscopy," *Nano Letters*, vol. 13, no. 4, pp. 1541–1548, 2013.

[44] J. A. Garlow, L. K. Barrett, L. Wu, K. Kisslinger, Y. Zhu, and J. F. Pulecio, "Large-Area Growth of Turbostratic Graphene on Ni(111) via Physical Vapor Deposition," *Scientific Reports*, vol. 6, no. 111, p. 19804, 2016.

[45] T. Kaplas, A. Zolotukhin, and Y. Svirko, "Thickness determination of graphene on metal substrate by reflection spectroscopy.," *Optics express*, vol. 19, no. 18, pp. 17226–31, 2011.

[46] Z. H. Ni, H. M. Wang, J. Kasim, H. M. Fan, T. Yu, Y. H. Wu, Y. P. Feng, Z. X. Shen, M. About, and T. Article, "Reflection and Contrast Spectroscopy Graphene Thickness Determination Using Reflection and Contrast Spectroscopy," *Nano letters*, vol. 7, no. 9, pp. 2758–2763, 2007.

[47] H. Jussila, H. Yang, N. Granqvist, and Z. Sun, "Surface plasmon resonance for characterization of large-area atomic-layer graphene film," *Optica*, vol. 3, no. 2, pp. 151–158, 2016.

[48] Wenjuan Zhu, C. Dimitrakopoulos, M. Freitag, and P. Avouris, "Layer Number Determination and Thickness-Dependent Properties of Graphene Grown on SiC," *IEEE Transactions on Nanotechnology*, vol. 10, pp. 1196–1201, sep 2011.

[49] A. Ruammaitree, H. Nakahara, K. Akimoto, K. Soda, and Y. Saito, "Determination of non-uniform graphene thickness on SiC (0001) by X-ray diffraction," *Applied Surface Science*, vol. 282, pp. 297–301, oct 2013.

[50] C. J. Shearer, A. D. Slattery, A. J. Stapleton, J. G. Shapter, and C. T. Gibson, "Accurate thickness measurement of graphene," *Nanotechnology*, vol. 27, p. 125704, mar 2016.

[51] D. Chandler-Horowitz and P. M. Amirtharaj, "High-accuracy, midinfrared (450cmâĹŠ1âľ¡ωâľ¡4000cmâĹŠ1) refractive index values of silicon," *Journal of Applied Physics*, vol. 97, p. 123526, jun 2005.

[52] G. E. Jellison, J. D. Hunn, and H. N. Lee, "Measurement of optical functions of highly oriented pyrolytic graphite in the visible," *Physical Review B*, vol. 76, p. 085125, aug 2007.

[53] H. S. Skulason, P. E. Gaskell, and T. Szkopek, "Optical reflection and transmission properties of exfoliated graphite from a graphene monolayer to several hundred graphene layers," *Nanotechnology*, vol. 21, p. 295709, jul 2010.

[54] R. R. Nair, P. Blake, A. N. Grigorenko, K. S. Novoselov, T. J. Booth, T. Stauber, N. M. R. Peres, and A. K. Geim, "Fine Structure Constant Defines Visual Transparency of Graphene," *Science*, vol. 320, pp. 1308–1308, jun 2008.

[55] K. F. Mak, L. Ju, F. Wang, and T. F. Heinz, "Optical spectroscopy of graphene: From the far infrared to the ultraviolet," *Solid State Communications*, vol. 152, pp. 1341–1349, aug 2012.

[56] K. F. Mak, J. Shan, and T. F. Heinz, "Seeing many-body effects in single- and few-layer graphene: Observation of two-dimensional saddle-point excitons," *Physical Review Letters*, vol. 106, no. 4, pp. 1–4, 2011.

[57] D.-H. Chae, T. Utikal, S. Weisenburger, H. Giessen, K. V. Klitzing, M. Lippitz, and J. Smet, "Excitonic Fano Resonance in Free-Standing Graphene," *Nano Letters*, vol. 11, pp. 1379–1382, mar 2011.

[58] L. Yang, J. Deslippe, C.-H. Park, M. L. Cohen, and S. G. Louie, "Excitonic Effects on the Optical Response of Graphene and Bilayer Graphene," *Physical Review Letters*, vol. 103, p. 186802, oct 2009.

[59] P. K. Gogoi, I. Santoso, S. Saha, S. Wang, A. H. Castro Neto, K. P. Loh, T. Venkatesan, and A. Rusydi, "Optical conductivity study of screening of many-body effects in graphene interfaces," *EPL (Europhysics Letters)*, vol. 99, p. 67009, sep 2012.

[60] I. Santoso, R. S. Singh, P. K. Gogoi, T. C. Asmara, D. Wei, W. Chen, A. T. S. Wee, V. M. Pereira, and A. Rusydi, "Tunable optical absorption and interactions in graphene via oxygen plasma," *Physical Review B*, vol. 89, p. 075134, feb 2014.

[61] L. Yang, "Excitonic Effects on Optical Absorption Spectra of Doped Graphene," *Nano Letters*, vol. 11, pp. 3844–3847, sep 2011.

[62] U. Fano, "Effects of Configuration Interaction on Intensities and Phase Shifts," *Physical Review*, vol. 124, pp. 1866–1878, dec 1961.

[63] L. Matthes, O. Pulci, and F. Bechstedt, "Optical properties of two-dimensional honeycomb crystals graphene, silicene, germanene, and tinene from first principles," *New Journal of Physics*, vol. 16, p. 105007, oct 2014.

[64] T. Stauber, N. M. R. Peres, and A. K. Geim, "Optical conductivity of graphene in the visible region of the spectrum," *Physical Review B*, vol. 78, p. 085432, aug 2008.

[65] H. Min and A. H. MacDonald, "Origin of Universal Optical Conductivity and Optical Stacking Sequence Identification in Multilayer Graphene," *Physical Review Letters*, vol. 103, p. 067402, aug 2009.

[66] K. F. Mak, J. Shan, and T. F. Heinz, "Electronic Structure of Few-Layer Graphene: Experimental Demonstration of Strong Dependence on Stacking Sequence," *Physical Review Letters*, vol. 104, p. 176404, apr 2010.

[67] R. Kundu, "Tight-binding Parameters for Graphene," *Modern Physics Letters B*, vol. 25, pp. 163–173, jan 2011.

[68] T. Deng and H. Su, "Orbital-dependent Electron-Hole Interaction in Graphene and Associated Multi-Layer Structures," *Scientific Reports*, vol. 5, p. 17337, dec 2015.

[69] P. J. Van Zwol, D. F. Vles, W. P. Voorthuijzen, M. Péter, H. Vermeulen, W. J. Van Der Zande, J. M. Sturm, R. W. E. Van De Kruijs, and F. Bijkerk, "Emissivity of freestanding membranes with thin metal coatings," *Journal of Applied Physics*, vol. 118, no. 21, 2015.

[70] J. S. Bunch, A. M. van der Zande, S. S. Verbridge, I. W. Frank, D. M. Tanenbaum, J. M. Parpia, H. G. Craighead, and P. L. McEuen, "Electromechanical Resonators from Graphene Sheets," *Science*, vol. 315, pp. 490–493, jan 2007.

[71] C. Lee, X. Wei, J. W. Kysar, and J. Hone, "Measurement of the Elastic Properties and Intrinsic Strength of Monolayer Graphene," *Science*, vol. 321, pp. 385–388, jul 2008.

[72] Y. Zhang and C. Pan, "Measurements of mechanical properties and number of layers of graphene from nano-indentation," *Diamond and Related Materials*, vol. 24, pp. 1–5, apr 2012.

[73] J.-U. Lee, D. Yoon, and H. Cheong, "Estimation of Young's Modulus of Graphene by Raman Spectroscopy," *Nano Letters*, vol. 12, pp. 4444–4448, sep 2012.

[74] I. Ovid'ko, "Mechanical Properties of Graphene," *Reviews on Advanced Materials Science*, vol. 34, pp. 1–11, 2013.

[75] A. Politano and G. Chiarello, "Probing the Young's modulus and Poisson's ratio in graphene/metal interfaces and graphite: a comparative study," *Nano Research*, vol. 8, pp. 1847–1856, jun 2015.

[76] C. N. Berger, M. Dirschka, and A. Vijayaraghavan, "Ultra-thin grapheneâĂŞpolymer heterostructure membranes," *Nanoscale*, vol. 8, no. 41, pp. 17928–17939, 2016.

[77] R. L. Edwards, G. Coles, and W. N. Sharpe, "Comparison of Tensile and Bulge Tests for Thin-Film Silicon Nitride," *Experimental Mechanics*, vol. 44, pp. 49–54, feb 2004.

[78] R. Ogden, "Non-linear elastic deformations," *Engineering Analysis with Boundary Elements*, vol. 1, p. 119, jun 1984.

[79] K. A. Gschneidner, "Physical Properties and Interrelationships of Metallic and Semimetallic Elements," *Solid State Physics - Advances in Research and Applications*, vol. 16, no. C, pp. 275–426, 1964.

[80] F. A. Vening Meinesz, *Elasticity and Plasticity / Elastizität und Plastizität*, vol. 6. Berlin, Heidelberg: Springer Berlin Heidelberg, 1958.

[81] R. S. Lakes, "Foam Structures with a Negative Poisson ' s Ratio," *Science*, vol. 235, no. 4792, pp. 1038–1040, 1987.

[82] G. N. Greaves, A. L. Greer, R. S. Lakes, and T. Rouxel, "Poisson's ratio and modern materials," *Nature Materials*, vol. 10, no. 11, pp. 823–837, 2011.

[83] J. Neggers, J. Hoefnagels, F. Hild, S. Roux, and M. Geers, "Global Digital Image Correlation for Pressure Deflected Membranes," vol. 6 of *Proceedings of the 2012 Annual Conference on Experimental and Applied Mechanics*, pp. 135–140, New York: Springer, 2013.

[84] S. Shafqat, "Mechanical Characterization of Freestanding Buckled Ultrathin Membranes," *MSc thesis*, 2014.

[85] P. A. Roman, *Polydimethylsiloxane tensile mechanical properties and membrane deflection theory Properties and Membrane Deflection Theory*. PhD thesis, 2004.

[86] Y. Xiang, X. Chen, and J. Vlassak, "Plane-strain Bulge Test for Thin Films," *Journal of Materials Research*, vol. 20, pp. 2360–2370, sep 2005.

[87] O. L. Blakslee, D. G. Proctor, E. J. Seldin, G. B. Spence, and T. Weng, "Elastic Constants of CompressionâĂŘAnnealed Pyrolytic Graphite," *Journal of Applied Physics*, vol. 41, pp. 3373–3382, jul 1970.

[88] Y. Huang, J. Wu, and K. C. Hwang, "Thickness of graphene and single-wall carbon nanotubes," *Physical Review B - Condensed Matter and Materials Physics*, vol. 74, no. 24, pp. 1–9, 2006.

[89] C. D. Reddy, S. Rajendran, and K. M. Liew, "Equilibrium configuration and continuum elastic properties of finite sized graphene," *Nanotechnology*, vol. 17, pp. 864–870, feb 2006.

[90] Q. Lu and R. Huang, "Nonlinear Mechanics of Single-Atomic-Layer Graphene Sheets," *International Journal of Applied Mechanics*, vol. 01, pp. 443–467, sep 2009.

[91] L. Zhou, Y. Wang, and G. Cao, "Elastic properties of monolayer graphene with different chiralities," *Journal of Physics: Condensed Matter*, vol. 25, p. 125302, mar 2013.

[92] B. M. Lempriere, "Poisson's ratio in orthotropic materials," *AIAA Journal*, vol. 6, pp. 2226–2227, nov 1968.

[93] I. S. Burmistrov, I. V. Gornyi, V. Y. Kachorovskii, M. I. Katsnelson, and A. D. Mirlin, "Quantum elasticity of graphene: Thermal expansion coefficient and specific heat," *Physical Review B*, vol. 94, no. 19, pp. 1–18, 2016.

[94] L. Lindsay, D. A. Broido, and N. Mingo, "Flexural phonons and thermal transport in multilayer graphene and graphite," *Physical Review B - Condensed Matter and Materials Physics*, vol. 83, no. 23, pp. 1–5, 2011.

[95] I. V. Gornyi, V. Y. Kachorovskii, and A. D. Mirlin, "Anomalous Hooke's law in disordered graphene," *2D Materials*, vol. 4, p. 011003, nov 2016.

[96] R. J. Nicholl, N. V. Lavrik, I. Vlassiouk, B. R. Srijanto, and K. I. Bolotin, "Hidden Area and Mechanical Nonlinearities in Freestanding Graphene," *Physical Review Letters*, vol. 118, p. 266101, jun 2017.

[97] J.-W. Jiang, T. Chang, X. Guo, and H. S. Park, "Intrinsic Negative Poisson's Ratio for Single-Layer Graphene," *Nano Letters*, vol. 16, pp. 5286–5290, aug 2016.

[98] J.-W. Jiang and H. S. Park, "Negative Poisson's Ratio in Single-Layer Graphene Ribbons," *Nano Letters*, vol. 16, pp. 2657–2662, apr 2016.

[99] J. R. Eskelsen, Y. Qi, S. Schneider-Pollack, S. Schmitt, K. W. Hipps, and U. Mazur, "Correlating elastic properties and molecular organization of an ionic organic nanostructure.," *Nanoscale*, vol. 6, no. 6, pp. 316–327, 2014.

[100] "Carbon - Graphite Materials." AZoM (1996). at `https://www.azom.com/properties.aspx?ArticleID=516`.

[101] M. Huang, X. Zhang, P. Ke, and A. Wang, "Graphite-like carbon films by high power impulse magnetron sputtering," *Applied Surface Science*, vol. 283, pp. 321–326, 2013.

[102] E. J. Gussenhoven, C. E. Essed, C. T. Lancée, F. Mastik, P. Frietman, F. C. van Egmond, J. Reiber, H. Bosch, H. van Urk, J. Roelandt, and N. Bom, "Arterial wall characteristics determined by intravascular ultrasound imaging: An in vitro study," *Journal of the American College of Cardiology*, vol. 14, pp. 947–952, oct 1989.

[103] B. T. Khuri-Yakub and O. Oralkan, "Capacitive micromachined ultrasonic transducers for medical imaging and therapy.," *Journal of micromechanics and microengineering : structures, devices, and systems*, vol. 21, pp. 54004–54014, may 2011.

[104] N. Lamberti, G. Caliano, A. Iula, and A. S. Savoia, "A high frequency cMUT probe for ultrasound imaging of fingerprints," *Sensors and Actuators, A: Physical*, vol. 172, no. 2, pp. 561–569, 2011.

[105] J. Juárez and G. R. Corral, "Piezoelectric transducer for airborne ultrasound," *Acustica*, vol. 29, pp. 234–239, 1973.

[106] Haller and Khuri-Yakub, "A surface micromachined electrostatic ultrasonic air transducer," in *Proceedings of IEEE Ultrasonics Symposium ULTSYM-94*, vol. 43, pp. 1241–1244 vol.2, IEEE, 1994.

[107] A. Caronti, G. Caliano, R. Carotenuto, A. Savoia, M. Pappalardo, E. Cianci, and V. Foglietti, "Capacitive micromachined ultrasonic transducer (CMUT) arrays for medical imaging," *Microelectronics Journal*, vol. 37, pp. 770–777, aug 2006.

[108] "High temperature capacitive micromachined ultrasound transducers." IP.com Prior Art Database (2010). at `http://priorart.ip.com/IPCOM/000199106`.

[109] M. C. Ho, M. Kupnik, K. K. Park, K. Eckhoff, and B. T. Khuri-Yakub, "Wide pressure range operation of air-coupled CMUTs," *IEEE International Ultrasonics Symposium, IUS*, pp. 93–96, 2012.

[110] J. Song, C. Xue, C. He, R. Zhang, L. Mu, J. Cui, J. Miao, Y. Liu, and W. Zhang, "Capacitive Micromachined Ultrasonic Transducers (CMUTs) for Underwater Imaging Applications," *Sensors*, vol. 15, pp. 23205–23217, sep 2015.

[111] G. Bui, Y. Jiang, and D. Pang, "Two Capacitive Micro-Machined Ultrasonic Transducers for Wind Speed Measurement," *Sensors*, vol. 16, p. 814, jun 2016.

[112] D. Barauskas, D. Pelenis, D. Virzonis, J. P. Baltrus, and J. Baltrusaitis, "Greenhouse Gas Molecule CO2 Detection Using a Capacitive Micromachined Ultrasound Transducer," *Analytical Chemistry*, vol. 88, pp. 6662–6665, jul 2016.

[113] A. Ramanaviciene, D. Virzonis, G. Vanagas, and A. Ramanavicius, "Capacitive micromachined ultrasound transducer (cMUT) for immunosensor design.," *The Analyst*, vol. 135, no. 7, pp. 1531–1534, 2010.

[114] A. S. Ergun, G. G. Yaralioglu, and B. T. Khuri-Yakub, "Capacitive Micromachined Ultrasonic Transducers: Theory and Technology," *Journal of Aerospace Engineering*, vol. 16, pp. 76–84, apr 2003.

[115] A. Ergun, O. Oralkan, G. Yarahoglu, B. Khuri-Yakub, A. S. Ergun, and Y. Huang, "Capacitive micromachined ultrasonic transducers: fabrication technology," *IEEE Transactions on Ultrasonics, Ferroelectrics and Frequency Control*, vol. 52, no. 12, pp. 2242–2258, 2005.

[116] O. Oralkan, A. Ergun, J. Johnson, M. Karaman, U. Demirci, K. Kaviani, T. Lee, and B. Khuri-Yakub, "Capacitive micromachined ultrasonic transducers: next-generation arrays for acoustic imaging?," *IEEE Transactions on Ultrasonics, Ferroelectrics and Frequency Control*, vol. 49, pp. 1596–1610, nov 2002.

[117] C. Chen, S. Lee, V. V. Deshpande, G.-H. Lee, M. Lekas, K. Shepard, and J. Hone, "Graphene mechanical oscillators with tunable frequency," *Nature Nanotechnology*, vol. 8, pp. 923–927, nov 2013.

[118] H. Tian, D. Xie, Y. Yang, T.-L. Ren, Y.-F. Wang, C.-J. Zhou, P.-G. Peng, L.-G. Wang, and L.-T. Liu, "Single-layer graphene sound-emitting devices: experiments and modeling," *Nanoscale*, vol. 4, no. 7, p. 2272, 2012.

[119] B. Lebental, A. Ghis, E. Delevoye, J.-M. Caussignac, and F. Bourquin, "Capacitive ultrasonic micro-transducer made of carbon nanotubes," *European Journal of Environmental and Civil Engineering*, vol. 15, pp. 649–662, jan 2011.

[120] S. Thibert, A. Ghis, and M. Delaunay, "Mechanical Characterization of Ultrathin DLC Suspended Membranes for CMUT Applications," *Physics Procedia*, vol. 70, no. 0, pp. 974–977, 2015.

[121] P.-F. Chong, X. Shi, and C.-h. Cheng, "Capacitive micromachined ultrasonic transducer (CMUT) array with single-layer graphene membrane," *Micro and Nano Letters*, vol. 9, pp. 884–886, dec 2014.

[122] E. Bahette, J. F. Michaud, D. Certon, D. Gross, and D. Alquier, "Progresses in cMUT device fabrication using low temperature processes," *Journal of Micromechanics and Microengineering*, vol. 24, no. 4, p. 045020, 2014.

[123] Ö. Oralkan, B. Bayram, G. G. Yaralioglu, A. Sanli Ergun, M. Kupnik, D. T. Yeh, I. O. Wygant, and B. T. Khuri-Yakub, "Experimental characterization of collapse-mode CMUT operation," *IEEE Transactions on Ultrasonics, Ferroelectrics, and Frequency Control*, vol. 53, pp. 1513–1523, aug 2006.

[124] I. O. Wygant, M. Kupnik, and B. T. Khuri-Yakub, "Analytically calculating membrane displacement and the equivalent circuit model of a circular CMUT cell," in *Proceedings - IEEE Ultrasonics Symposium*, no. 6, pp. 2111–2114, IEEE, nov 2008.

[125] K. K. Park, Ö. Oralkan, and B. Khuri-Yakub, "A comparison between conventional and collapse-mode capacitive micromachined ultrasonic transducers in 10-MHz 1-D arrays," *IEEE Transactions on Ultrasonics, Ferroelectrics, and Frequency Control*, vol. 60, pp. 1245–1255, jun 2013.

[126] D. Metten, G. Froehlicher, and S. Berciaud, "Monitoring electrostatically-induced deflection, strain and doping in suspended graphene using Raman spectroscopy," *2D Materials*, vol. 4, p. 014004, dec 2016.

[127] A. W. Leissa, *Vibration of Plates*. 1969.

[128] Y. Liu, B. Xie, Z. Zhang, Q. Zheng, and Z. Xu, "Mechanical properties of graphene papers," *Journal of the Mechanics and Physics of Solids*, vol. 60, pp. 591–605, apr 2012.

[129] "Silicon Nitride Ceramics." International Syalons (Newcastle) Limited (accessed sep 2017). at `http://www.syalons.com/resources/downloads/guide-to-types-of-silicon-nitride-ceramics.pdf`.

[130] M. Poot and H. S. J. Van Der Zant, "Nanomechanical properties of few-layer graphene membranes," *Applied Physics Letters*, vol. 92, no. 6, p. 063111, 2008.

[131] B. Kim, R. H. Olsson, K. Smart, and K. E. Wojciechowski, "MEMS resonators with extremely low vibration and shock sensitivity," in *2011 IEEE SENSORS Proceedings*, pp. 606–609, IEEE, oct 2011.

[132] C. Chen, S. Rosenblatt, K. I. Bolotin, W. Kalb, P. Kim, I. Kymissis, H. L. Stormer, T. F. Heinz, and J. Hone, "Performance of monolayer graphene nanomechanical resonators with electrical readout.," *Nature nanotechnology*, vol. 4, no. 12, pp. 861–867, 2009.

[133] R. A. Barton, B. Ilic, A. M. Van Der Zande, W. S. Whitney, P. L. McEuen, J. M. Parpia, and H. G. Craighead, "High, size-dependent quality factor in an array of graphene mechanical resonators," *Nano Letters*, vol. 11, no. 3, pp. 1232–1236, 2011.

[134] A. M. van der Zande, R. A. Barton, J. S. Alden, C. S. Ruiz-Vargas, W. S. Whitney, P. H. Q. Pham, J. Park, J. M. Parpia, H. G. Craighead, and P. L. McEuen, "Large-Scale Arrays of Single-Layer Graphene Resonators," *Nano Letters*, vol. 10, pp. 4869–4873, dec 2010.

Appendix A

Continuous versus discrete convolution[1]

In this appendix a short note on the incorporation of the convolution in the MATLAB scripts is given, since it is found that literature references scarcely elaborate on the exact numerical incorporation. The convolution is applied to account for spectral broadening of the signal in the model, a technique regularly used in spectroscopy. The **continuous** convolution of two responses $f(t)$ and $g(t)$ is given by

$$f(t) * g(t) = (f * g)(t) = \int_{-\infty}^{+\infty} f(\tau)g(t-\tau)d\tau \tag{A.1}$$

which essentially shifts the function $g(t)$ by τ over the function $f(t)$ integrating for all values of τ from $-\infty$ to $+\infty$.

Unfortunately, it is inherent to all experimental techniques that their responses are reported in **discrete** datapoints, not continuous functions. Equation A.1 then has to be rewritten in discrete form for two responses f and g with an infinite range

$$(f * g)[n] = \sum_{m=-\infty}^{+\infty} f[m]g[n-m] \tag{A.2}$$

which is similar as the expression used in the convolution function `conv` in MATLAB. When the `conv`-function in MATLAB is used to convolute two signals and to calculate a physical response, some assumptions have to be taken into account to ensure the correct physical response is acquired:

- In Equation A.2 there is no mention of any kind on the spacing between the datapoints.
- The discrete convolution has got an infinite range, while discrete signals always have truncated tails.

Considering the first issue: in the continuous integral in Equation A.1 the 'spacing' between the datapoints is taken into account by the $d\tau$ factor. In the discrete case this can be solved by ensuring the two arrays f and g both have equally spaced points with a spacing Δt. Equation

[1] Sources on numerical convolution for MATLAB:
- MATLAB-information page on the `conv`-function, `https://nl.mathworks.com/help/matlab/ref/conv.html`
- MATLAB forum thread on discrete convolution, `http://nl.mathworks.com/matlabcentral/newsreader/view_thread/168559`
- Instruction video on numerical approximation of continuous convolution, `https://www.youtube.com/watch?v=LZ0qjZezGkQ`

A.2 therefor has to be multiplied by Δt to gain a comparable and physical response.

The second issue of finite datapoints is solved by simply truncating the summation at the end of the dataset. Unfortunately, truncating the discrete convolution leads to artificial edge effects in the convoluted function. Numerically this can be solved by extending the original domain of the function both at the lower and upper end. After the convolution these extended regions, where the edge effects are located, are in turn removed from the domain to obtain the convoluted region of interest.

Summarizing: the convolution is applied to the original signal for spectral broadening. This is done via the discrete, truncated convolution function `conv` in MATLAB

$$(f * g)[n] = \Delta t \bullet \sum_{m=-M}^{+M} f[m]g[n-m] = [\Delta t \bullet \texttt{conv(f,g,'same')}]_{n^{\text{th}}\text{element}} \tag{A.3}$$

in which the original (extended) function f (length n, ranging from $-M$ to $+M$) is convoluted with a Lorentzian g (also length n), while taking into account the equal spacing Δt to acquire a physical response. The `'same'` input is given to only return the region of interest with length n, since the standard convolution returns a vector with a length of the two initial vectors f and g combined.

Appendix B

Square membrane fitting

Ideally a circular membrane is used to represent the biaxial strain situation, with the resulting spherical shape appearing when pressurized. Due to processing limitations square membranes are created which are spherically approximated. This Appendix chapter describes the different spherical approximations of the square membranes. The different models shown here are compared for the same bulge test dataset for direct comparison. Eventually the best spherical approximation method is found, which is used in acquiring the resulting membrane radius R during bulging.

B.1 Spherical fit

A first order approximation of the square membrane is simply assuming a pure spherical shape. The height profile can then be fitted using the general form for a sphere with radius R

$$(x-a)^2 + (y-b)^2 + (z-c)^2 = R^2 \tag{B.1}$$

with $(x, y, z) = (a, b, c)$ the sphere's center location. The height profiles are determined from profilometry on a 500 by 650 equidistant grid with 0.83 μm spacing. From each height profile the maximum is determined, after which a k x k area around the maximum is chosen. By varying the k-value the size of the area for fitting of the sphere can be determined. Ideally, the chosen area and k-value is small, minimizing the influence of the square membrane shape. In Figure B.1 multiple area sizes with $k = 100$, 200, 300 and 400 are shown, including the corresponding spherical fits. The height profiles with $k = 100, 200$ in Figure B.1a and b, respectively, show a good agreement with the spherical fits. In the fits of Figure B.1c and d, $k = 300$ and 400 respectively, the corner effects are more prominently visible, suggesting $k < 300$ for a good spherical approximation.

From the spherical fits the radius of curvature R is determined for area sizes ranging from $k = 50$ to $k = 450$, shown in Figure B.2a. For height profiles at multiple pressures this process is repeated, visualizing the area dependence k of the resulting radius of curvature R. It can be seen at $k < 100$ the radius of curvature shows large fluctuations, most likely due to the noise spread on the data. Towards higher values for k some pressures show an increase in curvature, although clear deviations at for example $P = 50$ mbar can be seen. At $k = 250$ the radius of curvature at $P = 50$ and 60 mbar are the same according to the fits, while during the experiment a clear increase in deflection is observed. Similarly, Figure B.1b shows the large fluctuations in the corresponding stress-strain curves for low values of k. Only towards large enough areas $k > 400$ the curves show a continuous upward trend as is expected from the increase in applied pressure. Unfortunately as seen in Figure B.1, for these large values of k the spherical approximation is not suitable anymore. Since both suggested regions for k do not

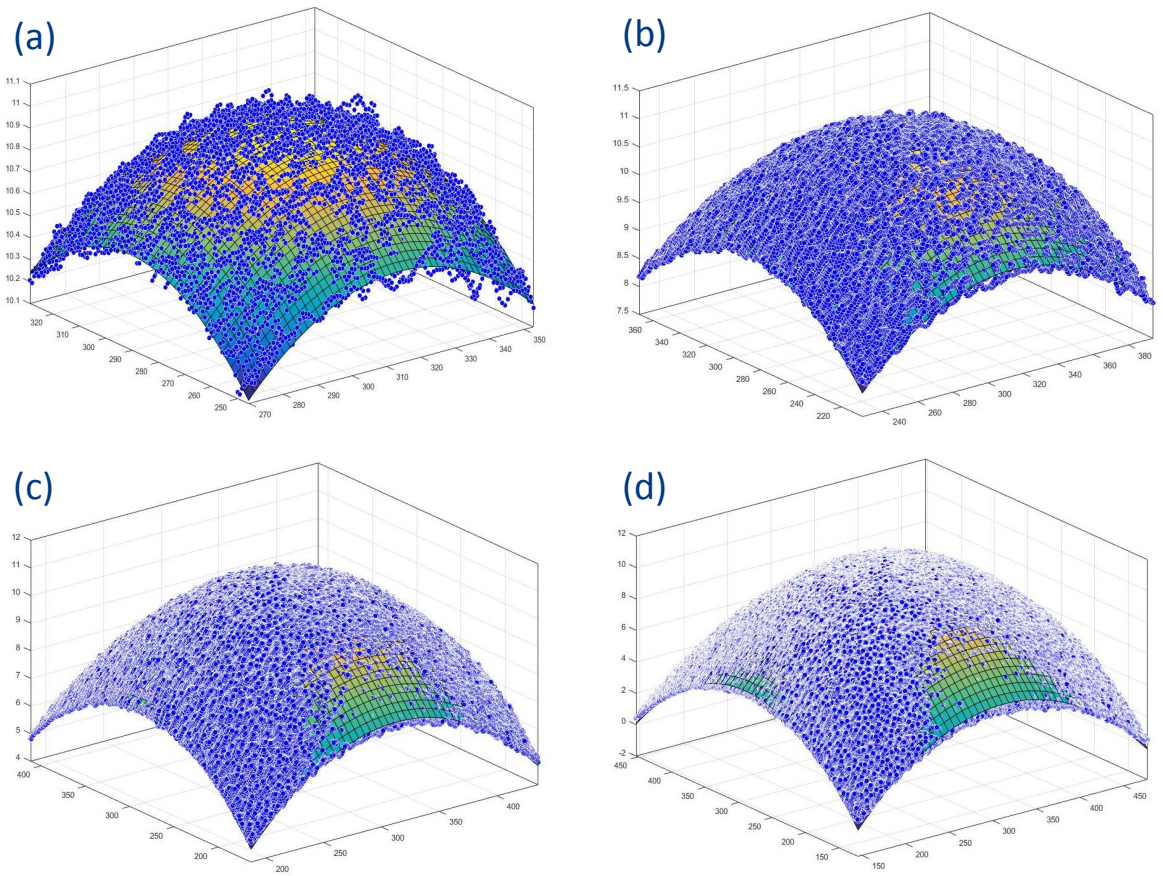

Figure B.1: *Multiple select areas of a membrane height profile for a type 1 multilayer graphene membrane with a thickness of $t = 11.5$ nm bulged at $P = 73$ mbar. The different areas are:* ***(a)*** *100 by 100 points,* ***(b)*** *200 by 200 points,* ***(c)*** *300 by 300 points and* ***(d)*** *400 by 400 points. Each area is fitted using the spherical formula of Equation B.1.*

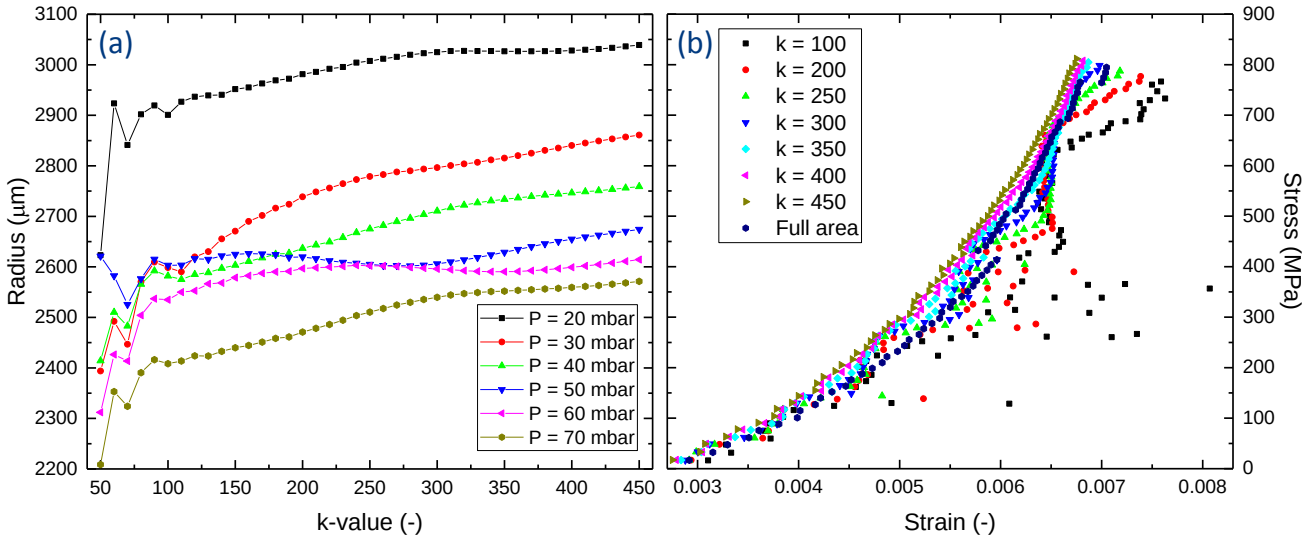

Figure B.2: *Extracted radius of curvature R and corresponding stress-strain curves for multiple values of k.* ***(a)*** *Radius of curvature extracted for several pressures P. Each pressure profile is analyzed for k-values ranging from 50 to 450.* ***(b)*** *Stress-strain curves calculated for multiple k-values on the same bulge test run.*

overlap, a different approach to a spherical approximation of the square membrane has to be found.

B.2 Individual cross-sectional fits

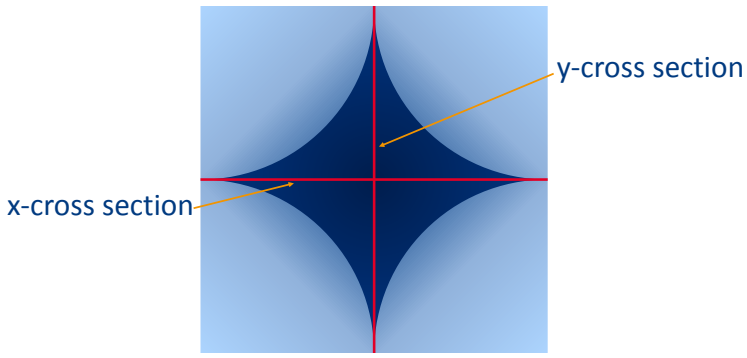

Figure B.3: *Schematic top view of a pressurized square membrane. The typical area where the square membrane can be spherically approximated is shown in dark blue, with the non-spherical parts indicated in light blue. The two cross-sections used for the spherical approximation are shown in red and are within the dark blue spherical region.*

A different approach is adapted which accounts for the square shape of the membrane. Figure B.3 shows a schematic view of a square membrane and the regions that can be spherically approximated. Around the center and towards the edges the membrane can be assumed to be spherical, indicated in dark blue. Towards the corners of the sample the spherical approximation is no longer valid, indicated in light blue. This is similar to observed in Figure B.1. By taking two cross sections of the height profile, as shown in red, the largest part of the curvature

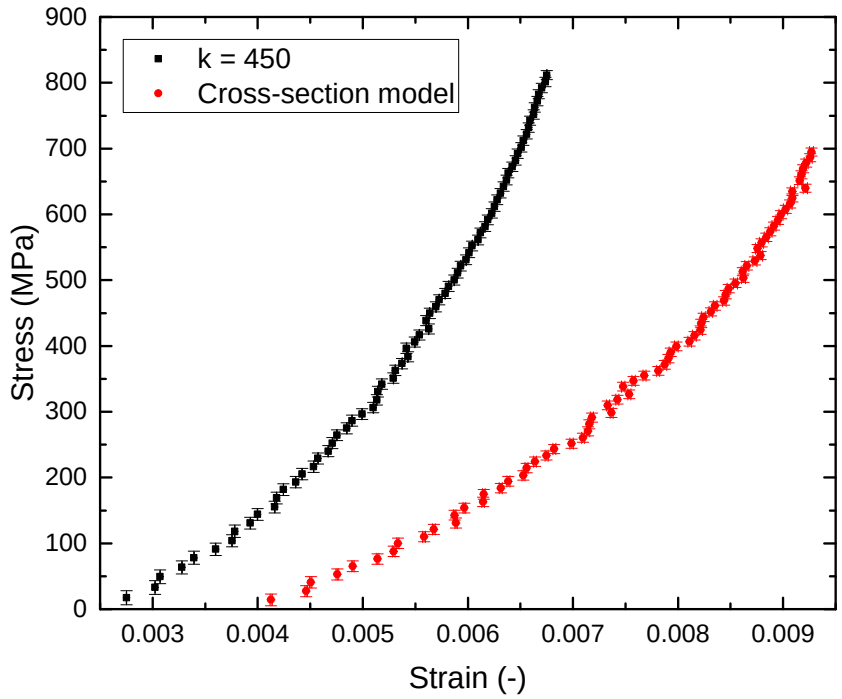

Figure B.4: *Comparison of stress-strain curves calculated with the 3D model ($k = 450$), indicated in black, and calculated using the cross section model, shown in red.*

within the spherical region is taken. These two 2-dimensional height profiles $z_x(y)$ and $z_y(x)$ are simultaneously fitted according to

$$\begin{cases} z_x(y) = c + \sqrt{R^2 - (y-a)^2} \\ z_y(x) = c + \sqrt{R^2 - (x-b)^2} \end{cases} \tag{B.2}$$

which share a common height offset c and individual offsets a and b in the x-direction and y-direction, respectively. The fitted radius R is used to determine the resulting stress-strain curve. Figure B.4 shows the stress-strain curve determined through the cross section model as well as the continuous curve using a 3D area with $k = 450$. It can be seen the cross-section model exhibits much larger strain values, which corresponds to the smaller values for R as determined in the fits. Comparing to the 3D area fit from Figure B.1d, it can indeed be seen the spherical fit overshoots the actual membrane profile towards the edges. Since this results in a larger value for R, the corresponding strain is less than the cross section model. Since the cross section model is more reliable in fitting spherically correct areas, this model is used to determine the deflection radius R of the bulged square membrane.

Appendix C

Stress-strain curve: hysteresis effects

In Chapter 4 is it shown the graphene membranes exhibit a non-linear stress-strain response. To verify this stress-strain response is an intrinsic material characteristic, not a result of membrane failure, hysteresis test are performed. In the hysteresis test the pressure difference P over the membrane is increased and decreased, meanwhile monitoring the resulting membrane deflection profile. Applying the described analysis method in Chapter 4, the corresponding stress and strain are calculated along loading and unloading of the membrane. After a loading and unloading cycle, the following loading and unloading cycle is performed up to a higher pressure. This process is repeated until membrane rupture, with the maximum pressure increasing by 10 mbar per cycle.

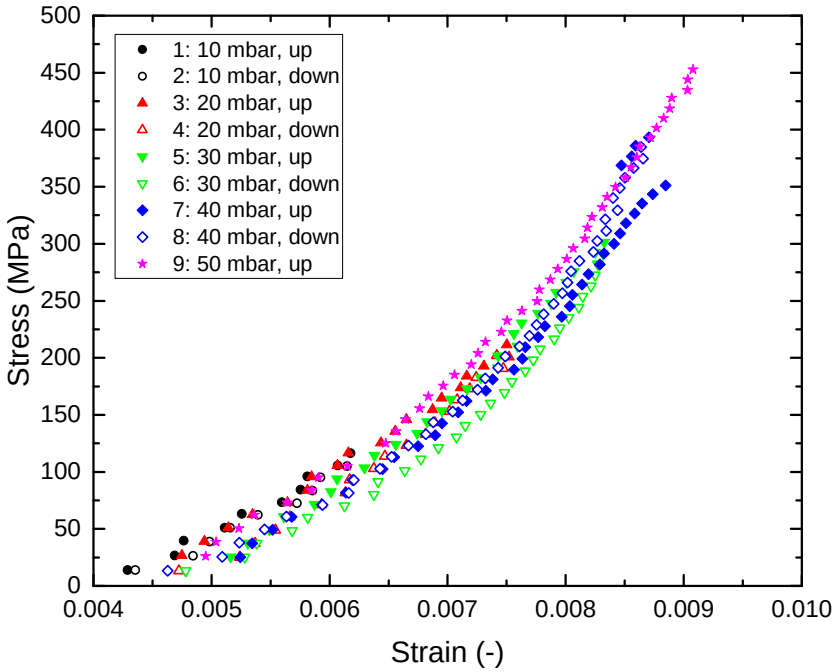

Figure C.1: *Stress-strain curve of a square multilayer graphene membrane (t = 11.5 nm) over multiple loading (solid marks) and unloading (open marks) cycles. After each unloading cycle the maximum applied pressure is increased with 10 mbar to 10, 20, 30, 40 and 50 mbar until membrane rupture.*

Figure C.1 shows a hysteresis test run performed on a square type 1 (t = 11.5 nm) multilayer graphene membrane. Each color indicates the stress and strain up until a certain pressure, with the solid and open marks representing the loading and unloading part of the cycle, respectively. As expected the bulging experiments show the non-linear effect, mainly in the cycles with

$P > 20$ mbar. Comparing the loading and unloading part within each cycle individually, it can be seen they follow similar patterns. In the case of the loading up to 40 mbar the curve shows a small discrepancy at the high end, possibly due to small membrane rearrangement. Despite this discrepancy, the unloading curve follows the loading part quite accurately. Comparing the loading and unloading curves of all the different cycles, no significant discrepancy is observed. This indicates the non-linear stress-strain effect indeed is a material property and can be attributed to intrinsic graphene characteristics.

Appendix D

Parameter error analysis

The errors in the parameters of interest are in general determined from the corresponding fit through the dataset. In the case of the full-range UV-vis transmission model in Chapter 3, the error in the thickness S_t is determined by linear scaling of the error in the number of layers S_N the with the interlayer distance d:

$$S_t = d \cdot S_N \tag{D.1}$$

All the other error propagations, mainly in the procedure of determining the mechanical characteristics in Chapter 4, are determined through the standard 68%-error propagation formula

$$S_y = \sqrt{\sum_{i=1}^{N} \left(\frac{\partial y}{\partial x_i}\right)^2 \cdot S_{x_i}^2} \tag{D.2}$$

with S_y the error for a parameter $y(x_1, x_2, ..., x_N)$ with individual errors S_{x_i}.

D.1 Individual strain moduli and Young's modulus

The average values for the biaxial and planar strain modulus are determined by calculating the average of the different individual strain moduli E_x, i, determined from linear approximation of the stress-strain curves

$$\overline{E_x} = \frac{1}{N} \sum_{i=1}^{N} E_{x,i} \tag{D.3}$$

with N the number of individual moduli and $x = p$ pr $x = b$ either for the planar or biaxial modulus, respectively. The error in $\overline{E_x}$ is determined by the standard deviation in the spread in $E_{x,i}$

$$S_{\overline{E_x}} = \sqrt{\frac{1}{N-1} \sum_{i=1}^{N} \left(E_{x,i} - \overline{E_x}\right)^2} \tag{D.4}$$

The formulas described above to determine the average values and errors for E_b and E_p are a general procedure to determine an average value and its corresponding error. In this thesis this procedure is also used to determine the values for the non-linear fitting parameters α, k and σ_* from Equation 4.15.

Since the Young's modulus is determined from the biaxial E_b and planar E_p modulus through

$$E = 2E_b - \frac{E_b^2}{E_p} \tag{D.5}$$

the corresponding error can be determined using Equation D.2 with the errors S_{E_b} and S_{E_p} the errors in the biaxial and planar modulus, respectively

$$S_E = \sqrt{\left(2 - 2\frac{E_b}{E_p}\right)^2 S_{E_b}^2 + \left(\frac{E_b^2}{E_p^2}\right)^2 S_{E_p}^2} \tag{D.6}$$

D.2 Poisson ratio

Similar to the Young's modulus, the Poisson ratio is a function of the biaxial E_b and planar E_p modulus

$$\nu = \frac{E_b}{E_p} - 1 \tag{D.7}$$

The corresponding error in the Poisson ratio can be calculated using Equation D.2

$$S_\nu = \sqrt{\left(\frac{1}{E_p}\right)^2 S_{E_b}^2 + \left(\frac{E_b}{E_p^2}\right)^2 S_{E_p}^2} \tag{D.8}$$

Appendix E

Individual bulge test fit parameters

In this appendix the individual values are given for parameters determined through the different fitting procedures performed on the stress-strain curves in Chapter 4. The average values and errors of the average values are calculated according to the procedure described in Appendix D.

E.1 Biaxial E_b and planar E_p modulus

As discussed in section 4.4, the individual biaxial E_b and planar E_p moduli of the different graphene membranes are determined by linearly approximation of the stress-strain curves in certain stress-regimes. The following sections present an overview of all the individual elastic moduli determined from the bulge test experiments performed on the individual graphene membranes.

E.1.1 Type 1 graphene: thickness $t = 11.5$ nm

Tables E.1 and E.2 show the individual biaxial E_b and planar moduli E_p, respectively, for the type 1 square graphene membranes with a thickness of $t = 11.5$ nm. The individual elastic moduli are determined by linear approximation of a low stress regime ($<$ 250-300 MPa) and a high stress regime ($>$ 300-350 MPa) of the stress-strain curves in Figure 4.7.

Table E.1: *Individual biaxial moduli E_b from the stress-strain curves of the square membranes in Figure 4.7 with a thickness $t = 11.5$ nm. The biaxial moduli are determined by linear approximation in the corresponding stress regime.*

Curve color	E_b **low stress regime ($<$ 250-300 MPa, in GPa)**	E_b **high stress regime ($>$ 300-350 MPa, in GPa)**
Black	87.8 ± 2.6	192.4 ± 4.7
Red	114.1 ± 3.3	166.0 ± 6.3
Orange	73.4 ± 2.6	-
Pink	68.6 ± 1.9	-
Light blue	79.9 ± 2.0	129.7 ± 3.4
Dark blue	70.9 ± 2.2	-
Purple	77.4 ± 2.1	152.1 ± 2.4
Green	79.9 ± 1.9	143.3 ± 1.8
Dark yellow	66.5 ± 1.7	-
Dark brown	96.7 ± 3.0	158.3 ± 3.8

Table E.2: *Individual planar moduli E_p from the stress-strain curves of the rectangular membranes in Figure 4.7 with a thickness $t = 11.5$ nm. The planar moduli are determined by linear approximation in the corresponding stress regime.*

Curve color	E_p **low stress regime (< 250-300 MPa, in GPa)**	E_p **high stress regime (> 300-350 MPa, in GPa)**
Black	93.6 ± 8.1	-
Red	81.1 ± 1.6	-
Orange	69.8 ± 4.4	-
Pink	70.7 ± 1.4	90.7 ± 10.5
Light blue	85.8 ± 2.5	113.3 ± 4.3
Dark blue	69.0 ± 1.5	133.9 ± 2.6
Purple	92.4 ± 5.4	-
Green	66.7 ± 1.3	87.7 ± 2.1

E.1.2 Type 2 graphene: thickness $t = 2.76$ nm

Similar to the type 1 graphene membranes with a thickness $t = 11.5$, stress-strain curves are determined for the type 2 graphene membranes with a thickness of $t = 2.76$ nm. Tables E.3 and E.4 show the individual biaxial E_b and planar moduli E_p, respectively, again determined for two stress regimes in Figure 4.12, below and above ∼600 MPa.

Table E.3: *Individual biaxial moduli E_b from the stress-strain curves of the square membranes in Figure 4.12 with a thickness $t = 2.76$ nm. The biaxial moduli are determined by linear approximation in the corresponding stress regime.*

Curve color	E_b **low stress regime (< 600 MPa, in GPa)**	E_b **high stress regime (> 600 MPa, in GPa)**
Black	96.7 ± 24.5	197.4 ± 57.6
Red	130.1 ± 16.5	375.4 ± 16.2
Orange	131.8 ± 15.9	-
Light blue	110.3 ± 16.9	233.6 ± 26.2
Dark blue	126.8 ± 14.3	167.0 ± 62.2
Purple	137.7 ± 18.2	194.5 ± 100.0
Green	132.3 ± 16.5	294.6 ± 11.9
Dark yellow	165.0 ± 19.2	-
Dark red	142.5 ± 10.8	235.1 ± 65.0

Table E.4: *Individual planar moduli E_p from the stress-strain curves of the square membranes in Figure 4.12 with a thickness $t = 2.76$ nm. The planar moduli are determined by linear approximation in the corresponding stress regime.*

Curve color	E_p **low stress regime (< 600 MPa, in GPa)**	E_p **high stress regime (> 600 MPa, in GPa)**
Black	92.4 ± 5.4	-
Red	81.1 ± 1.6	-
Green	69.8 ± 4.4	-
Pink	70.7 ± 1.4	-
Blue	69.0 ± 1.5	-
Dark green	85.8 ± 2.5	-
Dark yellow	66.7 ± 1.3	-

E.2 Non-linear strain-stress analysis parameters

As described in section 4.4.2 the non-linearity of the strain-stress curves of the type 1 graphene is quantitatively analyzed using the equation derived by Gornyi *et al.* (2016) [95]

$$\epsilon(\sigma) = \frac{\sigma_*}{k}\Big(\frac{\sigma}{\sigma_*} + \frac{1}{\alpha}\Big(\frac{\sigma}{\sigma_*}\Big)^{\alpha}\Big) \tag{E.1}$$

Table E.5 shows the individual values for α, $k = E_b$ and σ_* determined by fitting the strain-stress curves of the type 1 graphene membranes, as seen in Figure 4.11.

Table E.5: *Individual non-linear strain-stress parameters from Equation 4.15 determined by fitting the strain-stress curves of the type 1 graphene membranes in Figure 4.11.*

Curve color	**Non-linear exponent α (-)**	**Elastic modulus E_b (GPa)**	**Cross-over stress σ_* (MPa)**
Black	0.185 ± 0.010	355 ± 35	457 ± 94
Red	0.198 ± 0.020	371 ± 82	568 ± 253
Blue	0.117 ± 0.011	158 ± 11	89 ± 17
Green	0.140 ± 0.008	223 ± 16	208 ± 33
Purple	0.137 ± 0.009	203 ± 15	168 ± 30
Dark red	0.257 ± 0.044	227 ± 40	201 ± 106

Appendix F

Bulge test sample deviations

In general the stress-strain curves of the type 1 graphene follow the same upward trend, showing a reproducible mechanical response. The difference in the onset of the stress-strain curves has already been discussed, being an artifact of the presence of membrane attachments to the sidewalls.

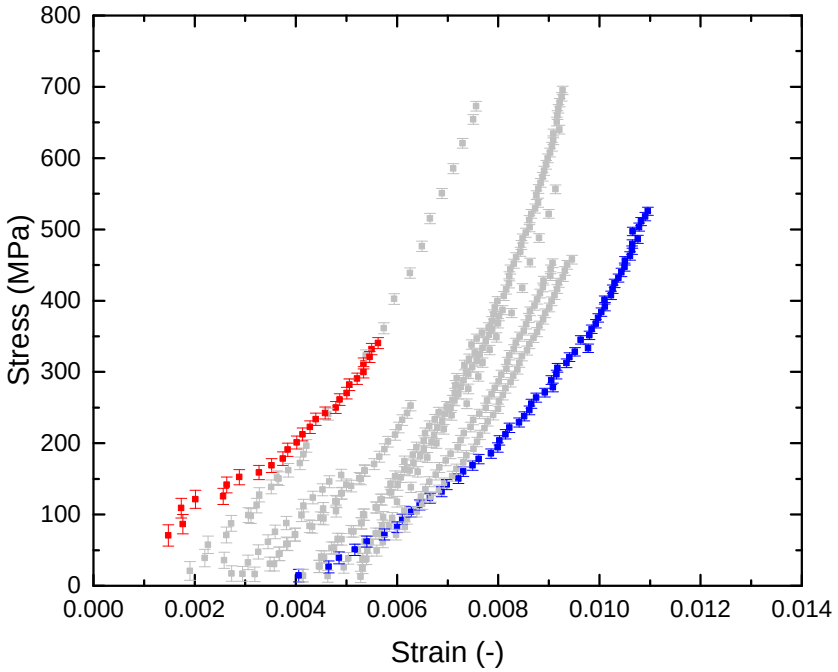

Figure F.1: *Stress-strain curves of type 1 square graphene membranes. The stress-strain curves as reported in Chapter 4 are indicated in grey, with the two deviating samples indicated in red and blue.*

Two samples measured during bulging have shown different stress-strain responses, indicated by the red and blue curves in Figure F.1. The sample indicated in red follows a relatively irregular stress-strain pattern. During bulging the sample deflection is followed by a camera along the same optical path as the interferometer signal. No folds are observed on the sample, but during bulging multiple irregular jumps in deflection are noticed. These jumps in deflection influence the measured curvature R and therefore lead an irregular stress-strain pattern. It is chosen not to take this sample into account in the statistical analysis due to the observed irregularity.

The stress-strain response indicated in blue does show a smooth continuous upward trend. Unfortunately, this trend does not correspond with the other stress-strain curves. Analyzing an optical image of the membrane, see Figure F.2, no large folds or other defects are identified. The sample does however show a much larger large-scale wrinkling compared to previous graphene membranes. This wrinkling results in the largest observed strain value of all the membranes $\epsilon \approx 0.011$. Although no definitive cause for this effect is identified, manual processing could have effected the graphene wrinkling. Since the stress-strain response is significantly different from the other coinciding curves, it is chosen to exclude this curve from statistical analysis.

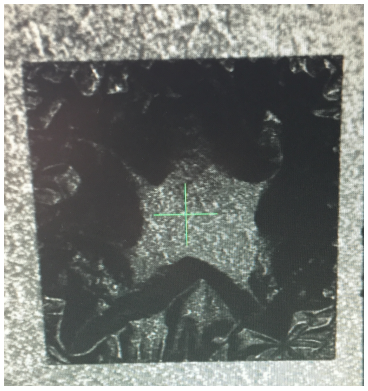

Figure F.2: *Optical image of the graphene multilayer sample showing the deviating stress-strain response. The corresponding stress-strain response is shown in blue in Figure F.1.*

Appendix G

MATLAB scripts

In this Appendix the MATLAB scripts developed in this thesis are reported. The script for fitting of the full-range UV-vis model is reported, as well as the coupled files required to calculate the conductivity of the multilayer graphene stack. Similarly the files used for fitting the height profiles are reported. The files are provided with comment lines for more detailed explanation, as well as previous code which can be potentially used for further improvement of the analysis method.

G.1 UV-vis transmission model

The MATLAB-file presented here is used to fit the multilayer graphene transmission spectra.

```
% In this script the thickness of a multilayer graphene stack is determined
% by fitting transmission data over the full wavelength range with a model
% for the conductivity, based on exciton resonance (Fano peak resonance).
% Main source is Mak et al. (2011), supported by Gogoi et al. (2012) and
% Santoso et al. (2014). Transmission and reflectivity are converted to and
% from conductivity according to Matthes et al. (2014)
% Most parameters can be initialized here, but in the file
% 'Graphene_conductivity_function.m' parameters can be chosen:
% 1) Use empirical conductivity or Stauber et al. (2008) model
% 2) Convolution type (Gaussian or Lorentzian) and corresponding width
% 3) Parameters can be set fixed in function file
% Model valid in range of [0,5.5] eV (not strict boundaries), and only at
% T=300 K.
% More information in MSc thesis of Jochem Huijs (2017)

clear all

%% Set constants
e = 1.60217662e-19; % elementary charge (in C)
h_bar = 1.054571628e-34; % reduced Planck constant (in J*s)
c = 2.99792458e8; % speed of light (in m/s)
epsilon_0 = 8.82e-12; % vaccuum permittivity (F/m)

% calculate universal optical conductivity
sigma_0 = e^2/(4*h_bar); % universal optical conductivity (no unit)

%% Parameters to initialize!
% set the start and end wavelenght of the fitting region
interlayer_distance = 0.335; % in nm
w_start = 250; % in nm
w_end = 1100;  % in nm
filename = '170913_UV-vis_to_thickness_UVVIS_05012017_&_08032017.xlsx';
```

```
33 sheet = 'Spectra_08032017';
34 X = 13; % column number of transmission in Excel-file (X=>2 since column 1 ...
       is x_data)
35 Z = 1; % set to 1 for reflectance data incoorporation
36 Y = 14; % column number of reflectance in Excel-file (Y=>2 since column 1 is ...
       x_data)
37
38 % Initial parameters and boundary conditions for fit
39 N_start = 10;       % number of layers (no unit)
40     N_lower = 1;
41     N_upper = 100;
42 t_start = 2.60;     % hopping parameter (in eV)
43     t_lower = 2;
44     t_upper = 4;
45 q_start = -1;       % Fano coupling parameter (no unit)
46     q_lower = -4;
47     q_upper = -0.1;
48 E_res_start = 5.02; % exciton resonance frequency (in eV)
49     E_res_lower = 4;
50     E_res_upper = 7;
51 Gamma_start = 1.0;  % width of exciton resonance (in eV)
52     Gamma_lower = 0.1;
53     Gamma_upper = 3;
54
55 %% Fitting procedure starts from here
56 T_data = xlsread(filename,sheet);
57 m = size(T_data);
58
59 % set rows outside of selected wavelength range to zero and remove rows
60 for i = 1:m(1)
61    if T_data(i,1) < w_start
62        T_data(i,:) = 0;
63    elseif T_data(i,1) > w_end
64        T_data(i,:) = 0;
65    end
66 end
67 T_data(all(T_data==0,2),:)=[];
68
69 % Convert wavelength to energy basis and extract selected column to fit
70 x_data = T_data(:,1);
71 E_data = 2 .* pi .* c ./ (x_data .* 1e-9) .* h_bar ./ e;
72 y_data = T_data(:,X);
73
74 % Convert transmission to conductivity (in units of sigma_0)
75 sigma = (sqrt(1./y_data)-1).*2.*c.*epsilon_0./sigma_0;
76
77 % Create new evenly spaced array in the energy domain(in wavelength to
78 % energy conversion spacing is NOT conserved), necessary for convolution
79 E_start = min(E_data);
80 E_end = max(E_data);
81 n = size(E_data);
82 E_even_spaced = transpose(linspace(E_start,E_end,max(n)));
83
84 % Fit spline through data and extract new (evenly spaced!) datapoints
85 f = fit(E_data,sigma,'smoothingspline','SmoothingParam',0.999);
86 sigma_data_even = feval(f,E_even_spaced);
87 %plot(f,E_data,sigma)
88
89 %% Define formula for fit and include initial startparameters
90 formula = @(x,E)Graphene_conductivity_function(E,x(1),x(2),x(3),x(4),x(5));
91 x0 = [t_start,N_start,q_start,E_res_start,Gamma_start];
92
```

```
% Include additional opties for fit, increase in nummber of evaluations and
% iterations, fit data with evenly spaced data sigma_data_even
options = optimoptions(@lsqcurvefit,'Algorithm','trust-region-reflective',...
    'MaxFunctionEvaluations',50000,'MaxIterations',10000);
[x,¬,resid,¬,¬,¬,J] = lsqcurvefit(formula,x0,E_even_spaced,sigma_data_even,...
    [t_lower N_lower q_lower E_res_lower Gamma_lower],...
    [t_upper N_upper q_upper E_res_upper Gamma_upper],options);

%% Calculate corresponding errors in parameters
Error = nlparci(x,resid,'jacobian',J);
x=transpose(x);
x(1,2) = (Error(1,2)-Error(1,1))/4;
x(2,2) = (Error(2,2)-Error(2,1))/4;
x(3,2) = (Error(3,2)-Error(3,1))/4;
x(4,2) = (Error(4,2)-Error(4,1))/4;
x(5,2) = (Error(5,2)-Error(5,1))/4;

%   Manual method to determine error
% dif = sigma_data_even - formula(x,E_even_spaced);
% Cov = inv(J'*J);
% x = transpose(x);
% x(1,2) = sqrt(Cov(1,1));
% x(2,2) = sqrt(Cov(2,2));
% x(3,2) = sqrt(Cov(3,3));
% x(4,2) = sqrt(Cov(4,4));
% x(5,2) = sqrt(Cov(5,5));

%% Calculate thickness of graphene multilayer membrane & plot data and fit
x
thickness = x(2,1)*interlayer_distance;
thickness(1,2) = x(2,2)*interlayer_distance

figure
fig1 = subplot(1,2,1);
plot(fig1,E_data,sigma)
hold on
plot(fig1,E_even_spaced,sigma_data_even)
plot(fig1,E_even_spaced,formula(x,E_even_spaced))
hold off

%% Calculate reflectance from the fitted conductance

R = ((formula(x,E_even_spaced)*sigma_0/(2*c*epsilon_0))./...
    (1+formula(x,E_even_spaced)*sigma_0/(2*c*epsilon_0))).^2;

fig2 = subplot(1,2,2);
plot(fig2,E_even_spaced,R)

if Z == 1
    hold on
    plot(fig2,E_data,T_data(:,Y))
    hold off
end
```

In order to keep the MATLAB-scripts concise, the conductivity modeling is separated into an individual function-file `Graphene_conductivity_function.m`.

```
function conductivity = Graphene_conductivity_function(E,t,N,q,E_res,gamma)
% parameter as basis
    % E: energy of the light (in eV)
% parameters to fit
```

```
5       % t: hopping parameter (in eV)
6       % N: number of graphene layers (no unit)
7       % q: Fano coupling parameter (no unit)
8       % E_res: exciton resonance frequency (in eV)
9       % gamma: width of exciton resonance (in eV)
10
11  %% Variable parameters
12  % choose sigma ¬log (W = 1) or sigma ¬Stauber (W = 2)
13  W = 1;
14  % choose to convolute with Lorentzian (Y = 1) or Gaussian (Y = 2) and width
15  Y = 1;
16  width = 0.25; % in eV
17
18  % Possibility to set parameters fixed
19  %t = 5.20/2;
20  %q = -1;
21  %E_res = 5.02;
22  %gamma = 1.0;
23  %N = 35;
24
25  %% Continuation of script
26  % create basis for calculations and arrays for calculation
27  X = 1500; % extra numbers on side of convolution
28  n = size(E); % determine number of datapoints
29  m = max(n)+2*X; % number of datapoints for larger range for convolution
30  sigma_real = zeros(m,1);
31  sigma_imag = zeros(m,1);
32  epsilon = zeros(m,1);
33  Fano = zeros(m,1);
34  sigma_real_Fano = zeros(m,1);
35  sigma = zeros(m,1);
36  conductivity = zeros(m,1);
37
38  % create larger base for convolution extending original base with X, since
39  % discrete convolution leads to edge effects
40  E_start = E(1);
41  E_end = E(max(n));
42  E_diff = median(diff(E));
43  E_back = transpose(linspace(1,X,X))*E_diff+E_end;
44  E_front = transpose(linspace(-1*X,-1,X))*E_diff+E_start;
45
46  % merge sides with original base
47  E_full = [E_front;E;E_back];
48
49  %% Test of functions (NOT CORRECT due to mismatch in base)
50  %     Lorentz_base1 = linspace(2*t-2.5,2*t+2.5,101);
51  %     Lorentz_base2 = linspace(2*t-2.5,2*t+2.5,501);
52  %     Lorentz_base3 = linspace(2*t-2.5,2*t+2.5,1001);
53  %     Lorentz_base4 = linspace(2*t-2.5,2*t+2.5,max(n));
54  %     Lorentz_base5 = linspace(E(1),E(max(n)),10000);
55  %     Lorentz1 = ...
        Conductivity_functions.Lorentzian_func(Lorentz_base1,0.250,2*t);
56  %     Lorentz2 = ...
        Conductivity_functions.Lorentzian_func(Lorentz_base2,0.250,2*t);
57  %     Lorentz3 = ...
        Conductivity_functions.Lorentzian_func(Lorentz_base3,0.250,2*t);
58  %     Lorentz4 = ...
        Conductivity_functions.Lorentzian_func(Lorentz_base4,0.250,2*t);
59  %     Lorentz5 = ...
        Conductivity_functions.Lorentzian_func(Lorentz_base5,0.250,2*t);
60  %     sigma_real_conv1 = ...
        median(diff(Lorentz_base1)).*conv(sigma_real,Lorentz1,'same');
```

```
61 %     sigma_real_conv2 = ...
       median(diff(Lorentz_base2)).*conv(sigma_real,Lorentz2,'same');
62 %     sigma_real_conv3 = ...
       median(diff(Lorentz_base3)).*conv(sigma_real,Lorentz3,'same');
63 %     sigma_real_conv4 = ...
       median(diff(Lorentz_base4)).*conv(sigma_real,Lorentz4,'same');
64
65 %    for i = 1:max(n)
66 %        sigma_real_convfunc(i) = ...
       Conductivity_functions.Lorentz_conv(E(i),t,mu);
67 %    end
68
69 % Tested FFT in stead of convolution, but gave similar results
70 %    sigma_test1 = abs(median(diff(E)))*ifft(fft(sigma_real).*fft(Lorentz6));
71 %    sigma_test2 = ...
       median(diff(Lorentz_base4))*ifft(fft(sigma_real).*transpose(fft(Lorentz4)));
72
73 %% Continuation of script
74 % calculate conductivity for full range (for functions, see file:
75 % 'Conductivity_funtions.m')
76
77      if W == 1
78          for i = 1:m
79              sigma_real(i) = 1-1.0*log(abs(1-E_full(i)/(2*t)));
80 %             sigma_real_gogoi(i) = -1.7*log(abs(1-E_full(i)/(2*t)))+0.8;
81          end
82      elseif W == 2
83          % ignore warning in integral calculation for Stauber method
84          warning('off', 'MATLAB:integral:MinStepSize')
85
86          mu = 0.2;  % set chemical potential fixed for Stauber method
87          for i = 1:m
88             sigma_real(i) = ...
                   Conductivity_functions.sigma_real_func(E_full(i),t,mu);
89             sigma_imag(i) = ...
                   Conductivity_functions.sigma_imag_func(E_full(i),t,mu);
90          end
91      end
92
93      % create shifted base for Lorenztian/Gaussian
94      E_base = E_full+2*t-(E_full(m)+E_full(1))/2;
95      if W == 1
96         conv_func = Conductivity_functions.Lorentzian_func(E_base,width,2*t);
97      elseif W == 2
98         conv_func = Conductivity_functions.Gaussian_func(E_base,width,2*t);
99      end
100
101     % convolute sigma with the Lorentzian/Gaussian, median necessary to
102     % gain correct physical response
103     sigma_real_conv = median(diff(E_full)).*conv(sigma_real,conv_func,'same');
104
105 % multiply convoluted conductivity with Fano resonance peak
106     for i = 1:m
107         epsilon(i) = (E_full(i)-E_res)./(gamma./2);
108         Fano(i) = (q+epsilon(i)).^2./(1+epsilon(i).^2);
109         sigma_real_Fano(i) = sigma_real_conv(i).*Fano(i);
110     end
111
112 % scale Fano corrected conductivity down to value from convoluted
113 % conductivity
114     if  W == 1
115         A = max(sigma_real_Fano)/max(sigma_real_conv);
```

```
116     elseif W == 2
117         A = 1.0;
118     end
119     sigma_real_Fano_scaled = sigma_real_Fano./A;
120
121     for i = 1:m
122         if (i > X) && (i ≤ m-X)
123             sigma(i) = sigma_real_Fano_scaled(i) + 0*sigma_imag(i);
124
125             % calculate total conductivity for total stack of N layers
126             conductivity(i) = abs(N*sigma(i));
127         end
128     end
129     % Only return the same shape array as the input by removing not-used rows
130     conductivity(all(conductivity==0,2),:)=[];
131 end
```

The experimental broadening of the conductivity can be done using a Lorentzian or Gaussian distribution. These functions are separated into a different file `Conductivity_functions.m`. Additionally, this file incorporates the conductivity described by Stauber *et al.* (2008) [64], but it is found the empirical description using $\sigma \sim -\log(E)$ is more representative for the background optical conductivity of single-layer graphene.

```
1  classdef Conductivity_functions
2
3      methods(Static)
4
5          function [x] = rho_func(E,t)
6
7              n = size(E);
8              x = zeros(n);
9
10             for i = 1:max(n)
11                 F_func = @(x,t) (1+x/(2*t))^2 - 0.25*((x/(2*t))^2-1).^2;
12                 K_func = @(x,m) ((1-x.^2).*(1-m.*x.^2)).^(-1/2);
13
14                 if E(i)/2 < t
15                     x(i) = 1./sqrt(F_func(E(i),t)) .* ...
                           integral(@(x)K_func(x,2.*E(i)./(F_func(E(i),t).*t)),0,1);
16                 elseif t < E(i)/2 %< 3*t
17                     x(i) = 1./sqrt(2.*E(i)./t) .* ...
                           integral(@(x)K_func(x,F_func(E(i),t).*t./(2.*E(i))),0,1);
18                 else
19                     x(i) = 0;
20                 end
21             end
22         end
23
24         % real part of conductivity (function)
25         function [x] = sigma_real_func(E,t,mu)
26
27             k_b = 8.617343e-5; % Boltzman constant (in eV/K)
28             T = 300; % temperature (in K), only valid for these experiments
29
30             x =  1/(12*sqrt(3)*pi) .* Conductivity_functions.rho_func(E,t) ...
                   .* ...
31                     (18 - (E./t).^2) .* (tanh((E + 2.* mu)./(4*k_b*T))+...
32                     tanh((E - 2.* mu)./(4*k_b*T)));
33         end
34
35         % imaginary part of conductivity (function)
```

```
36          function [x] = sigma_imag_func(E,t,mu)
37
38              x = 4./(E* pi) .* (mu - 2/9 * mu^3 / t^2) - ...
39                          1/pi * log (abs(E+2*mu)/abs(E-2*mu)) - 1/(36*pi) .* ...
40                          (E./t).^2 .* log (abs(E+2*mu)/abs(E-2*mu));
41          end
42
43          % Lorentzian function (normalized)
44          function [x] = Lorentzian_func(E,w,E_center)
45
46              x = 1./(pi*w.*(1+((E-E_center)./w).^2));
47          end
48
49          % Convolution with Lorentzian centered around 2*t and width 0.250
50          % (integral goes from -10*width to +10*width around center 2*t)
51          function [x] = Lorentz_conv(E,t,mu) %NOT FUNCTIONAL
52
53              integral_func = @(x) ...
                    Conductivity_functions.sigma_real_func(x,t,mu).*...
54                  Conductivity_functions.Lorentzian_func(E-x,0.250,2*t);
55              x = integral(@(s)integral_func(s),2*t-2.5,2*t+2.5);
56
57          end
58
59          % Gaussian function (normalized)
60          function [x] = Gaussian_func(E,w,E_center)
61
62              x = 1./(w.*sqrt(2*pi))*exp(-0.5*((E-E_center)./w).^2);
63          end
64      end
65  end
```

G.2 Bulge test: membrane profile fits

The membrane profiles in the cylindrical and square configurations are analyzed according to the procedures described in section 4.3.1. The fitting files shown here return the extracted radius of curvature R, which consequently can be used to determine the stress σ and strain ϵ applied to the membrane at the different pressures P. The height profile files are given as an '`.plu`'-file output by the Sensofar. The file `pluread.m` (not reported here) is used to convert the `.plu`-files to regular matrices, used for further analysis in the MATLAB-files.

G.2.1 Cylindrical membrane

```
1  clear all
2
3  % filename needs to be in the format '5x1mm_"N",0mb_20x.plu' with "N" the
4  % corresponding pressure in mbar, steps need to be constant and in
5  % integers!
6
7  % Insert the experiment parameters here, needs to be in integers
8  P_start = 1; %insert the starting pressure here in mbar (in integers!)
9  P_end = 5; %insert the end pressure here in mbar (in integers!)
10 stepsize = 1; %insert the stepsize between the pressures in mbar
11
12 M = (P_end-P_start)/stepsize+1; %calculates the number of measurements
13
14 R = zeros(P_end-P_start,3); %create matrix to insert all radius values
```

```
% note: if stepsize>1 then rows with zeros will stay in the matrix, this is
% corrected at the end of the script

% Create empty matrix to collect Y-data for wrinkles
%Y_data = zeros(1000,M+1);

for P = P_start : stepsize : P_end

    R(P-P_start+1,1)=P; % Sets the first number of the row to the ...
        corresponding pressure

    file = strcat('5x1mm_',int2str(P),',0mb_20x.plu');
    Profile = pluread(file);

    [n,m] = size(Profile.Z);
    xyzPoints = zeros(n*m,3);

    for i = 1 : m
        for j = 1 : n
            t = n*(i-1)+j;
            xyzPoints(t,1) = Profile.x(i);
            xyzPoints(t,2) = Profile.y(j);
            xyzPoints(t,3) = Profile.Z(j,i);
        end
    end

    xyzPoints=xyzPoints(¬isnan(xyzPoints(:,3)),:);

    %print pressure to screen
    P

    %fit the model through the pointcloud and store radius and error
    ft = fittype('b+e*y+sqrt(R^2-(x-a-d*y)^2)','dependent',{'z'},...
        'independent',{'x','y'},'coefficients',{'a','b','R','d','e'});
    f = fit([xyzPoints(:,1),xyzPoints(:,2)],xyzPoints(:,3),ft,...
        'StartPoint',[400,-3500,1000,0.001,0.001],'Lower',[200,-30000,50,-1,-1],...
        'Upper',[600,-50,30000,1,1])
    Err = confint(f);

    R(P-P_start+1,2)=f.R;
    R(P-P_start+1,3)=(Err(2,3)-Err(1,3))/4;

    % Save the data on the central line for plotting:
    %for k = 1 : n
    %Y_data(k,1)=Profile.y(k);
    %Y_data(k,P-P_start+2)=Profile.Z(k,m/2)+1.0*(P-P_start);
    %end
end

R(all(R==0,2),:)=[] % Remove rows containing zeros and print the end result

% Clear the whole matrix from zeros
%Y_data(all(Y_data==0,2),:)=[]
```

G.2.2 Square membrane

```
clear all

% filename needs to be in the format '5x1mm_"N",0mb_20x.plu' with "N" the
% corresponding pressure in mbar, steps need to be constant and in
```

```
% integers!

% Insert the experiment parameters here, needs to be in integers
P_start = 1; %insert the starting pressure here in mbar (in integers!)
P_end = 11; %insert the end pressure here in mbar (in integers!)
stepsize = 1; %insert the stepsize between the pressures in mbar

k = 50; % determines how many points around the 3D-fit maximum are
        % taken into account to fix the actual maximum

M = (P_end-P_start)/stepsize+1; %calculates the number of measurements

R = zeros(P_end-P_start,5); %create matrix to insert all fitting parameters ...
    and radius values
% note: if stepsize>1 then rows with zeros will stay in the matrix, this is
% corrected at the end of the script

%% Start loop here:

for P = P_start : stepsize : P_end

    R(P-P_start+1,1)=P;% Sets the first number of the row to the ...
        corresponding pressure

    file = strcat('1x1mm_',int2str(P),',0mb_20x.plu');
    Profile = pluread(file);

    %print pressure to the screen
    P

    [m,n]=size(Profile.Z);
    xyzPoints = zeros(n*m,3);

    for i = 1:n
        for j = 1:m
            t = m*(i-1)+j;
            xyzPoints(t,1) = Profile.x(i);
            xyzPoints(t,2) = Profile.y(j);
            xyzPoints(t,3) = Profile.Z(j,i);
        end
    end

    % Fit a sphere through the pointcloud to image the surface
    xyzPoints=xyzPoints(¬isnan(xyzPoints(:,3)),:);

    ft1 = fittype('c+sqrt(R^2-(x-a)^2-(y-b)^2)','dependent',{'z'},...
        'independent',{'x','y'},'coefficients',{'a','b','c','R'});
    f1 = fit([xyzPoints(:,1),xyzPoints(:,2)],xyzPoints(:,3),ft1,'StartPoint',...
        [400,400,-4000,4050],'Lower',[200,200,-20000,50],'Upper',[600,600,0,20000])

    % Find index numbers of the maximum point from the 3D fit
    % x-direction
    tmp1 = abs(Profile.x-f1.a); % calculate array with difference between ...
        target value f.a and position Profile.x
    [idx idx] = min(tmp1); %index of closest value

    % y-direction
    tmp2 = abs(Profile.y-f1.b); % calculate array with difference between ...
        target value f.a and position Profile.x
    [idy idy] = min(tmp2); %index of closest value


```

```
63      % Create a new matrix with zeros which only center around around the
64      % values from the 3D-fit maximum
65      MaxMatrix = zeros(m,n);
66      for i = idx-k/2:idx+k/2
67          for j = idy-k/2:idy+k/2
68              MaxMatrix(j,i) = Profile.Z(j,i);
69          end
70      end
71
72      MaxValue = max(MaxMatrix(:));
73      [rowMax colMax] = find(Profile.Z == MaxValue);
74
75      % Calculate the x and y position of the maximum value
76      y = Profile.y(rowMax(1,1));
77      x = Profile.x(colMax(1,1));
78
79      % x-cross section
80      x_cross = zeros(m,2);
81      x_cross(:,1) = Profile.y;
82      x_cross(:,2) = Profile.Z(:,colMax(1,1));
83      %removes all the NaN values from the matrix
84      x_cross=x_cross(¬isnan(x_cross(:,2)),:);
85
86      % y cross section
87      y_cross = zeros(n,2);
88      y_cross(:,1) = Profile.x(:);
89      y_cross(:,2) = Profile.Z(rowMax(1,1),:);
90      %removes all the NaN values from the matrix
91      y_cross=y_cross(¬isnan(y_cross(:,2)),:);
92
93      % This method uses combined-dual fits for the two directions
94      f2 = ...
            @(par)nonlinmodel(par,x_cross(:,1),y_cross(:,1),x_cross(:,2),y_cross(:,2));
95      [optimal_par,no_use1,no_use2,no_use3,no_use4,no_use5,J] = ...
96          lsqnonlin(f2,[f1.c;f1.R;f1.b;f1.a],[-20000;50;200;200],[0;20050;600;600]);
97
98      dif1 = ...
            x_cross(:,2)-(optimal_par(1)+sqrt(optimal_par(2).^2-(x_cross(:,1)-optimal_par(3)).^2));
99      dif2 = ...
            y_cross(:,2)-(optimal_par(1)+sqrt(optimal_par(2).^2-(y_cross(:,1)-optimal_par(4)).^2));
100     dif = [dif1;dif2];
101     Cov = inv(J'*J)*var(dif);
102
103     R(P-P_start+1,2)=optimal_par(4);
104     R(P-P_start+1,3)=optimal_par(3);
105     R(P-P_start+1,4)=optimal_par(2);
106     R(P-P_start+1,5)=sqrt(Cov(2,2));
107 end
108
109 R(all(R==0,2),:)=[] % Remove rows containing zeros and print the end result
```

The combined cross-section fits are given in a separate file for practical purposes **nonlinmodel.m**.

```
1  function z = nonlinmodel(par,loc1,loc2,x_height,y_height)
2      z = [x_height-(par(1)+sqrt(par(2).^2-(loc1-par(3)).^2));...
3          y_height-(par(1)+sqrt(par(2).^2-(loc2-par(4)).^2))];
```